EMERGING USE OF SINGLE-CHANNEL SHORT WAVE INFRARED IMAGING FOR SEA ICE DETECTION

by

NICHOLAS SEAN LEWIS

B.S., United States Military Academy, 2008

M.S., American Public University, 2016

A thesis submitted to the

Faculty of the Graduate School of the

University of Colorado in partial fulfillment

of the requirement for the degree of

Master of Arts

Department of Geography

2018

This thesis entitled:

Emerging Use of Single-Channel Short Wave Infrared Imaging for Sea Ice Detection

written by Nicholas S. Lewis

has been approved for the Department of Geography

_____

Mark Serreze

_____

Waleed Abdalati

_____

David Gallaher

Date_____

The final copy of this thesis has been examined by the signatories, and we find that both the content and the form meet acceptable presentation standards of scholarly work in the above mentioned discipline.

Abstract

Lewis, Nicholas Sean (M.A., Geography)

EMERGING USE OF SINGLE-CHANNEL SHORT WAVE INFRARED IMAGING FOR SEA ICE DETECTION

Thesis directed by Research Professor Mark Serreze

This work assesses the feasibility of using a single channel shortwave infrared (SWIR) approach to detect and chart sea ice in Hudson Bay using GOES-16 data as a proxy for overhead persistent infrared. While not traditionally exploited for sea ice remote sensing, the availability of near continuous shortwave infrared data streams over the Arctic from overhead persistent infrared (OPIR) satellites could provide an invaluable source of information regarding the changing Arctic climate. Traditionally used for the purpose of missile warning and strategic defense, characteristics of OPIR make it an attractive source for Arctic remote sensing as the temporal resolution can provide insight into ice edge melt and motion processes. Fundamentally, the classification algorithm discerns water/ice/clouds using a time-based algorithm as well as raw data processing enhancements. Demonstration of the temporal utility and sensitivity of GOES-16 SWIR to detect and discern water/ice/clouds provides a justification for exploring the utility of military OPIR sensors for civil and commercial applications. Products will be limited by seasonal solar presence due to their reliance on reflected energy and will have a spatial resolution constrained by the underlying data set. Potential users include the scientific community as well as emergency responders, the fishing, oil and gas, and transportation industries that are seeking to exploit changing conditions in the Arctic but require more accurate and timely ice charting products.

I dedicate this thesis to my wife, Amy, and our sons, Samuel and Benjamin. Their love and support have enabled this project and allowed me to be successful at “work-school”. You guys make life fun.

Acknowledgements:

I would like to thank those who have assisted in the production of this thesis over the past two years and supported me throughout this process. Firstly my wife, who has read and helped to edit each of my papers during this degree, has been an invaluable resource, ensuring that I maintain focus on the audience and am clear in communicating the science. I would like to acknowledge Dr. Mark Serreze and David Gallaher of the National Snow and Ice Data Center for offering me the opportunity to study at the University of Colorado and supporting my efforts through advising, mentorship, and facilities/technology support. The staff of NSIDC has also been a tremendous support over the past two years with both technology support as well as being an incredible scientific resource. Dr. Waleed Abdalati of the Cooperative Institute for Research in Environmental Sciences has provided invaluable mentorship and directed my progress in remote sensing. I express my sincere thanks to Dr. Lora Koenig of NSIDC for her patience and guidance in the continued efforts in both this work, as well as the overall ICARTA project. I am also grateful to the other scientists on the ICARTA team who have assisted in the development of algorithms for classification, data preprocessing, and geolocation of the datasets to include Dr. G. Garrett Campbell, Dr. Glenn Grant, Dr. Kevin Schaefer, Dr. Jeffery Thompson and Florence Fetterer of NSIDC. Fellow students advised by Dr. Serreze, including Dr. Alexander Crawford, Erika Schreiber, Sara Morris, Meghan Helmberger, and Jonathon Cavitt, have all contributed to the production of this work through advice, technical assistance, and friendship. I am particularly appreciative of their friendship over the past two years. Lastly, I am grateful for the love and support that my family and I have received from our friends at Brave Church in Broomfield, Colorado. This community has sustained our family for the past two years through friendship, prayer, and love.

Contents

List of Figures:

Introduction & Context:

Short wave infrared (SWIR) remote sensing is ideal for capturing high-heat phenomena in imagery because of the transparency of the atmosphere at SWIR wavelengths. Temperatures associated with these features reach peak emission in the SWIR portion of the electro-magnetic spectrum allowing for clear discernment in remotely sensed imagery. If an aspect of a sensor's SWIR resolution is dramatically increased, its utility can expand to other naturally occurring earth phenomena beside heat events. Such is the case for sea ice remote sensing using single channel SWIR from Overhead Persistent Infrared (OPIR) satellites. While providing continuous coverage of the North Polar region for missile warning, the U.S. Air Force designed the Space Based Infrared System (SBIRS) to identify high intensity heat events that correspond to missile/rocket launches anywhere in the world. The nature of missile warning requires persistent coverage, but events occur at a relatively low frequency. The result is a constellation of satellites collecting valuable continuous data over the Arctic with a very small customer base. Given appropriate filtering and computational algorithms, this "noise" data for the Air Force is ripe for scientific discovery.

The purpose of this research is to explore the utility of high temporal resolution short wave infrared data to determine the feasibility of using SBIRS data to create a sea ice product during spring and summer seasons in the Arctic. This project will use Geostationary Operational Environmental Satellite – 16 (GOES-16) data as a proxy for the Air Force data, due to the classified nature of "missile warning" data. While most of the specific characteristics about the SBIRS highly elliptical orbit (HEO) satellites is classified, GOES-16 can still serve as a proxy data set based on the similar physics and orbital mechanics of this satellite when compared to SBIRS-HEO. While the center frequency of the SWIR band on SBIRS is unknown, there are two channels on GOES-16 that use portions of the SWIR spectrum (1.3-3 microns). Similarly, the GOES-16 satellite is located in a geostationary orbit (GEO), and while SBIRS-HEO is an entirely different orbital regime, orbital altitude of the GEO is a fair approximation of an expected HEO apogee altitude. Constraints with regard to optics sizes for remote sensing platforms in these orbital regimes means that

spatial resolution may also be approximate when comparing GOES-16 and an OPIR platform. The most important point of the GOES-16 proxy data is that it has a near-continuous time sampling by imaging the same portion of the earth at least every fifteen minutes.

Due to this orbit, sensor design, and primary missions of existing satellites, scientists have little access and therefore have not explored the utility of SWIR data for remote sensing of sea ice. Given a free, continuous, and available data source, there is great utility in deriving a product from currently discarded data. Leveraging SBIRS for sea ice charting and characterization farther north than GOES views may yield products to aid in Arctic navigation, particularly for emergency response actions where timely products are invaluable. Using the GOES-16 data as a proxy for SBIRS will allow increased collaboration for an effective algorithm, as it does not have the same dissemination restrictions as missile warning data.

The requirement for increased Arctic navigability and domain awareness will become present in the coming years as sea ice continues its steady decline, particularly during summer months (Melia et al., 2016). As the Arctic becomes more open to navigation during polar day, maritime use will significantly increase with focuses on shipping, fisheries, and oil production. Without much-needed infrastructure in the high Arctic, emergency response and management for these type of operations will be very limited. The ability to project emergency services into the Arctic will become more critical as the Arctic increases seasonal variability in sea ice cover, but these operations will be limited by the availability of data products informing current conditions. A persistent remote sensing platform could provide this intelligence, enabling both the civil/military/commercial ventures as well as the emergency preparedness for first responders.

Remote sensing of sea ice is currently available at a time scale of approximately 1-day to cover the entire Arctic. Products are pieced together from multiple overpasses of polar-orbiting satellites, creating mosaics of daily conditions at a resolution of 250m – 2km. Other products are produced daily at a scale of 12.5km or 25km and are used to give overview of Arctic-wide conditions and trends for current and

historical analysis. These products are limited in their utility for current Arctic operations because of the lag in production time, as well as the requirement to aggregate data over a time period (at least one day). This means that after the data is processed and disseminated, it is at least 24 hours old. In an environment where surface and atmospheric conditions change rapidly, existing Arctic sea ice products lack the time scale (in both collection and processing) to be an asset in navigation and current operations. This project explores an alternative to these existing products. While the data may not be of the same spatial quality as mosaicked datasets, the temporal scale is a vast improvement.

Aside from ice charting products, this project explores the remote sensing fundamentals that are often overlooked in an age where "more data" from "more channels" is the solution to challenges posed from remote sensing datasets. The constraint of single-channel remote sensing imposed by using GOES-16 as a representative proxy of missile warning data focuses efforts on extracting as much exploitable information as possible from the limited amount of data. These efforts have applicability across all disciplines of remote sensing as an example of manipulating data using proven techniques to tease out the features of imagery that are the subject of scientific research.

Research Questions:

The proposed research will address the following questions:

a. Is there enough sensitivity within the SWIR bands of the EM spectrum to develop an accurate sea ice product from a given data set?

b. Can a temporal based approach overcome the data limited nature of a single-channel algorithm, as well as a poor spectral resolution for sea ice studies?

Literature Review:

Passive microwave satellite sensors provide the most reliable and consistent method of measuring sea ice concentration and gauging the many subsequent values that are dependent upon accurate

concentration estimates. These products include sea ice area, sea ice extent, and ice volume. Many of these products are incorporated into numerical weather prediction, global climate models, and other atmospheric models that use hindcasting and forecasting to predict conditions on the surface of the earth in both the near and long term.

These sensors have become the preferred method of data collection because they operate regardless of sun-conditions and passive microwave data is easily converted into a useful term for earth surface assessments - brightness temperature. Unlike near-infrared and visible satellites, which typically only capture data where the sun is shining, passive microwave collects long-wave radiation from the earth at different frequency intervals that correspond to naturally occurring molecular level phenomena on the earth's surface. Additionally, the atmosphere is much more transparent to microwave frequency ranges, allowing a broader spectrum of collection than does the visible or infrared frequencies. Microwave frequencies can see through clouds as well, while clouds are opaque to infrared frequencies.

Sea ice concentration is the measure of ice in a sampled area as a percentage between 0-1 (or 0-100). This value helps to determine how much ice is present in the polar regions and how that ice cover changes over time. Ice concentration can then be used to gauge the spatial extent of the ice. This is a more useful term for trend analysis and as such, this number is tracked throughout the satellite record (dating back to the late 1970s) to provide a snapshot as to how the earth's polar ice cover is changing over the years. Critical to identifying any of the changes in the earth's sea ice cover is the accurate sampling of ice conditions using passive microwave.

Physical characteristics of the ice changes how it emits longwave radiation and reflects shortwave radiation at sampled frequencies. In order to understand the meaning of remote sensing data, it is essential to understand the complex nature of sea ice formation/melt. Many of the models that are used to convert satellite data into meaningful values require separate models of the earth's surface conditions,

to include atmospheric information and surface characteristics. When all of this information is synthesized, there is significant utility in passive microwave for sea ice measurements.

Sea Ice Formation:

Sea ice forms when the fresh water layer of the Arctic Ocean (about 20m deep) reaches its temperature of maximum density, which for salt water is equivalent to the freezing point (Serreze & Barry, 2014). As the water column cools to around -1.8°C (salinity adjusted freezing point), the air temperature (2 meters above the surface) and surface (skin) temperature are much colder. This dramatic gradient between a relatively warm body of water and the frigid air causes the ocean to continue to lose heat at the surface levels. Heat loss reduces the water's top layer temperature to the point where it is able to freeze. Once the top layer has frozen, ice will continue to form beneath it, transmitting ocean heat through the ice into the atmosphere causing further freezing. This process will continue to occur throughout the winter but, as the ice becomes thicker, the transfer of heat away from the water becomes less efficient. This will cause the ice formation rate to decline and move toward stagnation over the course of the 6-month winter season.

The water in the top layer of the Arctic is fairly fresh compared to other ocean waters as a result of ice melt, precipitation, and river runoff from four major rivers in the Arctic. The salinity, temperature, and density of the water all serve as a function to stratify the Arctic, keeping a cold, relatively fresh layer near the surface and available for freeze-up. The Arctic warms below this layer as the salinity increases with depth and the density allows for a higher heat capacity. The heat contained within the ocean at all layers is much higher than what is contained in the atmosphere. The ocean continues to lose heat to the atmosphere, first where there is open water, and then by transmitting through the ice that forms at the surface.

When snow falls onto the ice, the temperature gradient between the water, ice and snow creates the conditions for kinetic metamorphism of the snow. Even if the snow grains are fine when they initially

fall onto the ice, it almost immediately begins to change shape as a function of the vapor pressure gradient established by the temperature difference between the air and water. This gradient causes water vapor to migrate through the snowpack and freeze onto other snow grains. This increases the size of the snow grains within the snowpack and ultimately effects how visible and infrared light are reflected by the surface. Even if there is not a significant temperature gradient, fine grains of snow on sea ice will undergo equilibrium metamorphism as the wind blows and breaks grains, and creates conditions for sintering.

The Arctic is a seasonably cloudy location and cloud coverage creates problems for satellite retrievals at high latitudes (Serreze & Barry, 2014). Cloud cover peaks between April and October when significant temperature gradients between sea and air enable the development of low-level clouds. Discrimination of clouds from snow/ice is challenging due to similar reflectance values of those mediums, especially when only one spectral band is available for image feature discrimination. Pertinent to this project is the spectral reflectance of clouds as well as the movement of cloud cover. Despite their predominance in the Artic, clouds are distinguishable by their movement relative to the surface. Sea ice moves with currents and wind, but not on the same timescale as clouds, enabling the possibility for cloud filtering through time-series images.

Remote Sensing of Sea Ice

Infrared Wavelengths

Shortwave radiation is reflected by snow and ice on the surface in very specific ways. The albedo of the surface is dependent upon the grain size and density of the snow/ice, as well as the angle of the sun. In visible wavelengths, fresh snow has an albedo close to one (0.95). Bare sea ice has a much lower surface albedo (0.8). Albedo changes with snow grain size of the surface because the surface area of a given areal medium is greater when the grains are smaller. The solar zenith angle, or the angle from directly overhead to the sun elevation, is significant because it scales the amount of light that can be reflected toward the

sensor. When the zenith angle is large, the sun is low in the sky so there is a diffuse effect of sunlight from the snow/ice surface.

In the shortwave infrared portion of the spectrum (1.6-3microns), the albedo of sea ice and snow is very low. It peaks at 2.25 microns, but even there it only reaches about 30% - a function of the snow grain size. Finer grains of snow will reflect about 30% of the incoming shortwave infrared radiation, but larger grains have a much lower albedo. Since snow grains begin to metamorphose shortly after deposition on the ice, there is a very short window when this fine grain snow exists on the surface. When there is just ice, the albedo is very low in these wavelengths, but this value is distinguishable from the underlying water. Radiance values based on solar reflectance are very susceptible to the surface roughness (presence of sastrugi, etc. on the surface) and the orientation of the sun during the collection.

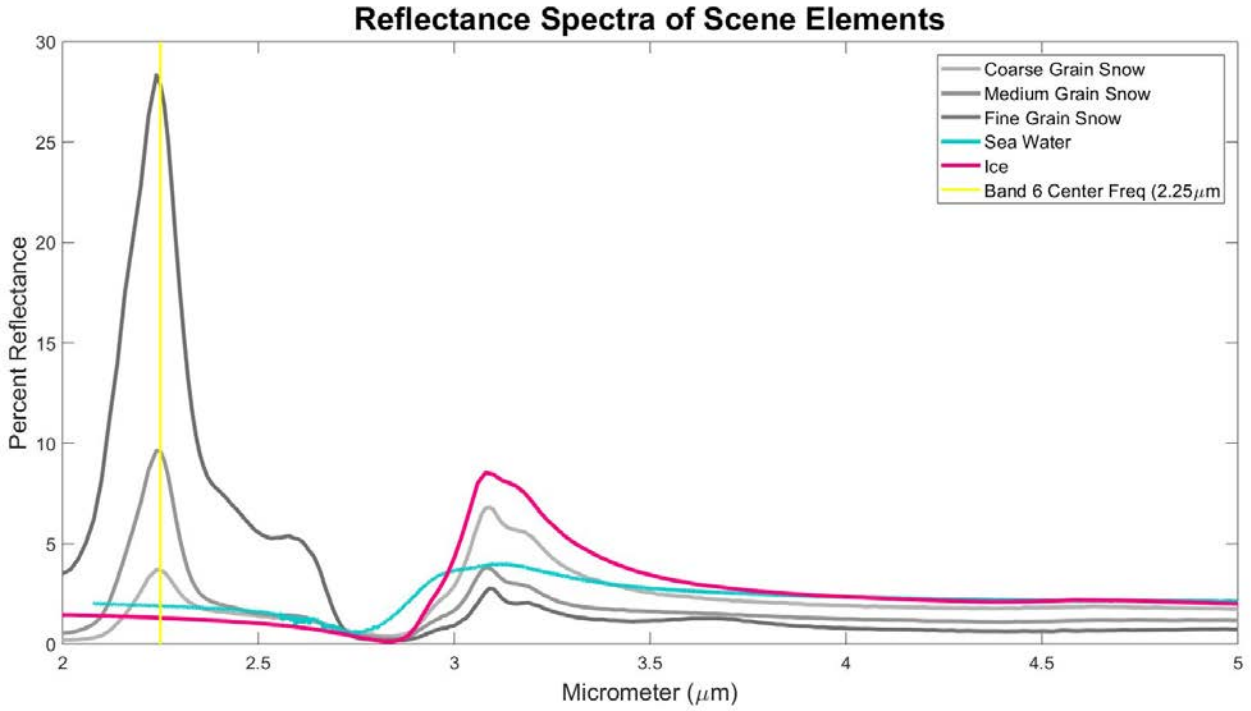

Figure 1: Spectral reflectance of different surface mediums in the SWIR portion of the EM Spectrum. GOES-16 Band 6 is centered at 2.25μm. (Hook, 2017)

In the midwave infrared region of the electromagnetic spectrum (3-6 microns), the reflectance of shortwave radiation is one component of the radiance. The other is a thermal component that is defined by emissivity and temperature of the surface. The reflectance component is subject to the same conditions

as the shortwave infrared signal, influenced by surface roughness, orientation of the sun, and the size of snow grains / density of the surface. The difficulty in separating the reflected component from the emitted component of radiance complicates the use of an MWIR channel in the ice-detecting algorithm. This is especially the case when there is no additional dataset available to assist in the emitted vs reflected assessment.

Infrared Algorithms

The prevalence of snow covered land in winter months combined with the availability of visible and infrared space-based sensors established the requirement for development of an algorithm that uses these wavelengths to map and chart the earth's snow cover (Hall et al., 1995). Snow cover is a critical component to the net surface radiation budget of the earth, so accurate and complete mapping of this feature is valuable for other assessments and measurements. Aside from sampling along snow courses and then at Snow Telemetry (SNOTEL) sites, accurate samples of snow depth, variability, and cover have remained a challenge for those interested in snow as a water resource as well as those who work with radiation budgets. Using visible and near infrared sampling techniques from space based platforms represented an improvement in the ability to monitor snow cover over large areas often too remote for *in situ* sampling. Despite the availability of satellite platforms to study and assess snow cover, spatial variability, vegetation cover, topography, slope, and wind make this a challenging endeavor.

Remote sensing platforms measure surface radiance. This is different from reflectance in that radiance is a measurement of reflected energy at a specific point in space (the sensor), whereas reflectance is the total amount of energy that is reflected from the surface. Therefore, a surface's radiance should always be less than an objects' reflectance but there are other influencing factors. Path radiance has an influence on the overall radiance value, which can increase the reported value. Path radiance is energy reflected toward the sensor or into the study area from adjacent objects or the atmosphere.

One of the major issues with remote sensing of snow covered surfaces is the visible reflectance properties of snow and clouds. In visible wavelengths, the white surface of clouds is nearly indistinguishable from that of a snowy landscape. The similar reflectance values translate into similar radiance values. To combat this effect, near infrared channels are often incorporated into the assessment of snow cover from space. While the visible wavelengths reflect similarly for clouds and snow, that is not the case for near infrared channels. Clouds reflect near infrared wavelengths while snow surfaces absorb them much more efficiently. This difference allows a snow surface to become distinguishable from overhead clouds. One particularly effective wavelength for such discrimination is at 1.6µm.

Initial snow mapping algorithms built upon techniques developed for the normalized difference vegetative index (NDVI). Using a normalized differencing technique contrasts coincident collections in different band wavelengths for the sun's influence, as the solar zenith angle is identical for all collected frames. While NDVI was effective at distinguishing vegetation cover from bare soil and water, a similar approach was taken for snow mapping. Combining green and near infrared wavelengths in a normalizing algorithm allows for distinguishing snow cover from clouds. This method first developed using Landsat Thematic Mapper channels, was designed for the improved spatial resolution found on the Moderate Resolution Imaging Spectroradiometer (MODIS) and named the Normalized Difference Snow Index (NDSI).

(1) $NDSI = \frac{(TM\ band2 - TM\ band5)}{(TM\ band2 + TM\ band5)}$ (Hall et al., 1995)

An NDSI assessment is less precise with regard to established thresholds than its vegetation counterpart. By charting different thresholds and their respective snow covered areal estimates, a distribution of the algorithm's surface types is inferred. Values in the range of .25 and .45 were reliable and consistent in discerning snow cover, and water was determined using a combination of the NDSI calculated value as well as the reflectance in the near infrared band, in which water has a very low reflectance value (Hall et al., 1995). Thresholds set above .5 for snow yielded results that showed large changes in snow covered regions and were ultimately determined to be too inaccurate to use.

Additional methods have been developed that use similar techniques but slightly different frequencies for establishing the snow cover/ice cover threshold. Dorofy, et. al 2016, used visible and midwave infrared channels (3.9µm) on the GOES 13 imager because the sensor did not have a 1.6µm channel. Their algorithm sought to use only the reflected solar energy that is a component of the 3.9µm channel, so they incorporated additional bands to remove the thermal component of that band. Using brightness temperatures derived from a strictly thermal infrared band (10.7µm) they were able to determine skin temperature of the surface and initialize their snow model from this condition (Dorofy et al., 2016). It then used specific reflectance values of each of the channels of interest as well as a ratio of the visible and midwave infrared bands to determine the presence of lake/sea ice.

Passive Microwave Frequencies

For passive microwave, the critical component for measuring sea ice concentration is brightness temperature. Brightness temperature is the temperature of a blackbody that emits the same amount of radiation as an observed surface (Shokr and Sinha, 2015). The Stefan-Boltzmann law (equation 2) governs this quality, which relates a radiative flux (R_B) to a physical temperature (*T)* using a constant value (σ: the Stefan-Boltzmann constant).

$$(2)\quad R_B = \sigma T^4$$

The radiative flux of a blackbody is based upon Planck's equation. This theoretical construct identifies the radiative flux for a blackbody of a specific frequency and temperature. Because the passive microwave region deals with very high frequency and low wavelengths, one of the terms in Planck's equation approaches its limit of one. This allows for an approximation of the equation which simplifies the terms. The resulting equation is the Rayleigh-Jean's approximation *(equation 3)*.

$$(3)\quad R_B(\gamma) = \frac{2hkT_\gamma{}^2}{c^2}$$

This equation relates the radiance at a given frequency [$R_B(\gamma)$] to Plank's constant (*h*), the Boltzmann constant (*k*), the speed of light (c), and the physical temperature of an object (T_γ). An inversion of *equation 2* yields the equation for brightness temperature in the microwave region as a function of the radiative flux, or intensity at a given frequency (*equation 4*).

$$(4)\ \ T_b = \frac{c^2 * R_b}{2k_\gamma{}^2}$$

In the microwave region of the electromagnetic spectrum (1-300GHz), the brightness temperature of an object (surface) is equivalent to the emissivity of that object multiplied by the physical temperature (*equation 5)*.

$$(5)\ \ T_B = \varepsilon_\gamma * T$$

This relationship makes the brightness temperature very sensitive to changes in the emissivity value (a number between 0-1), which allows passive microwave sensors to be exploited fairly easily for sea ice assessments. For most passive microwave sensors, the brightness temperature is a level 3 product that is disseminated as data from the system or data archive center. This creates a common starting value that lends itself easily to computation and algorithm exploitation for many different functions.

While the emissivity of water is fairly consistent throughout other portions of the electro-magnetic spectrum used for satellite remote sensing, it varies substantially in the microwave regions (Shokr & Sinha, 2015). Throughout the IR bands, water's emissivity is very close to that of snow and ice, but the values diverge significantly in the microwave regions. This feature of physics creates the opportunity for scientists and researchers to use *equation 5* to determine significant information with regard to the earth's sea ice cover.

Using the brightness temperature derived from the satellite sensor, the sea ice concentration is calculated using a weighted average method. The observed/measured brightness temperature is an average of the concentrations of both ice and water in the pixel multiplied by their respective, representative, brightness temperature values. The equation to calculate sea ice concentration makes use

of the Rayleigh-Jean's approximation and the derived relationship between emissivity and physical temperature to brightness temperature. It also assumes that the surface is only a combination of ice and water.

$$(6)\quad T_{b,obs} = c_{ice}(\varepsilon_{ice} * T_{ice}) + c_{water}(\varepsilon_{water} * T_{water})$$

$$(7)\quad T_{b,obs} = c_{ice}\left(T_{b,ice}\right) + c_{water}\left(T_{b,water}\right)$$

This is the most fundamental form of the sea ice concentration equation, and would be appropriate for computing concentration values given a single band (channel) of a satellite sensor. The inherent problems with such a calculation, however, is that passive microwave frequencies are subject to atmospheric attenuation, and brightness temperatures are susceptible to variations in surface temperature that can be either real or perceived.

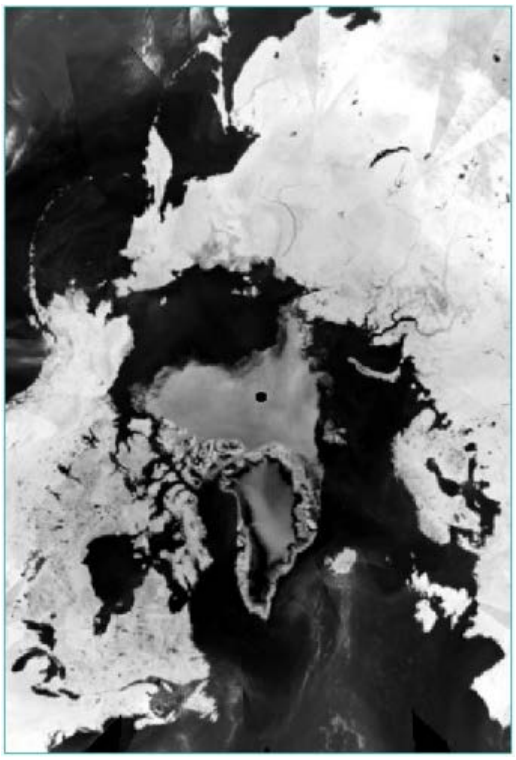

(Cavalieri et al., 2014)

Figure 2: Brightness Temperature Data from the Advanced Microwave Scanning Radiometer - Earth Observing Satellite.

The atmosphere is transparent to the microwave region of the electro-magnetic spectrum. Unlike the infrared portions of the spectrum, large atmospheric windows in the microwave region enable passive

microwave remote sensing. However, even these bands are attenuated by the atmosphere. Across the most prominent bands for passive microwave sensors (18GHz, 37GHz, 89GHz) some of the microwave signal is attenuated by water vapor, ozone, and CO_2 in the Earth's atmosphere. Because the attenuation is fairly low compared to IR regions, these minor fluctuations by frequency allow algorithm optimization to detect or remove atmospheric phenomena.

Significant variations in surface temperature values across a remotely sensed scene can skew data when the surface is fairly uniform in type, but has substantial variation in surface roughness. Emissivity will remain constant in this scenario, but the changes in physical temperature can have a dramatic effect on the brightness temperature. To correct for these conditions, brightness temperature data is often converted into more useful terms that limit the impact of physical temperature variation and surface roughness on measured brightness temperature. These terms are ratios derived from plotting passive microwave band collections in different polarities, or at different frequencies, and identifying noteworthy traits like correlation values. The resultant ratios are independent of physical temperature influences, increasing utility of the measured data.

The polarization ratio is a term developed by plotting the different polarization collections from the same frequency against one another. This allows normalization of the brightness temperatures by correcting for variations in perceived surface temperatures. The scatterplots developed from comparing multiple polarization ratios help to identify correlations of ice concentrations and provide sample regions for which representative brightness temperatures of either water or ice can be selected.

$$(8)\quad PR = \frac{T_{b,\gamma,V} - T_{b,\gamma,H}}{T_{b,\gamma,V} + T_{b,\gamma,H}}$$

Similarly, the spectral gradient ratio compares the same polarity of different spectral bands to identify patterns in the data. These spectral gradient ratios can then be compared to the opposite polarity, or against polarization ratios to identify patterns in the brightness temperature data while minimizing the influence of surface temperatures and surface roughness. Some common comparisons are the GR(85V19V)

and GR(85H19H) which identify perturbations in low concentration areas due to surface roughness, and GR(37V19V) and PR(19) which can identify portions of the data that are most representative of 100% concentration values for open water and ice (Markus et al., 2008). These data segments can then be assessed to determine representative brightness temperature values for inclusion in the inversion of *equation 7* to solve for ice concentration.

$$(9)\quad GR = \frac{T_{b,\gamma 1p} - T_{b,\gamma 2,p}}{T_{b,\gamma 1,p} + T_{b,\gamma 2,p}}$$

Passive Microwave Algorithms:

There are two primary passive microwave algorithms used to calculate sea ice concentration, the Bootstrap Algorithm and the Advanced NASA Team Algorithm (NT2)[1]. Both of these algorithms use passive microwave channels in the ≈19GHz and ≈37GHz regions that produce brightness temperature data. In both algorithms the multiple channels are plotted against one another to form scatterplots from which patterns are discernable. The method of comparing the channels varies, however, and there are substantial differences in how these two algorithms model the environment, exploit the electromagnetic spectrum, and derive reference brightness temperature values or tie points.

Bootstrap Algorithm:

The bootstrap algorithm makes use of the ≈36GHz channel of passive microwave sensors in both polarizations. This channel is used because the emissivity of sea water in both polarities is near equivalent and accounts for spatial variation in surface temperature (Markus et al., 2008). When plotted against one another (vertical polarity on the x-axis, and horizontal polarity on the y-axis) in a scatterplot, there are

[1] The Bootstrap Algorithm is applied to data from the Defense Meteorological Satellite Program (DMSP) passive microwave sensor (SSMI/S) while the Advanced NASA Team 2 algorithm is applied to AMSR-E and AMSR2 data collected from a different satellite at a different spatial resolution. The original NASA Team algorithm was also applied to DMSP passive microwave data.

distinctive linear trend lines that form within the data. These linear trends correspond to high ice concentration (around the line AD) and high water concentration (around the line OW).

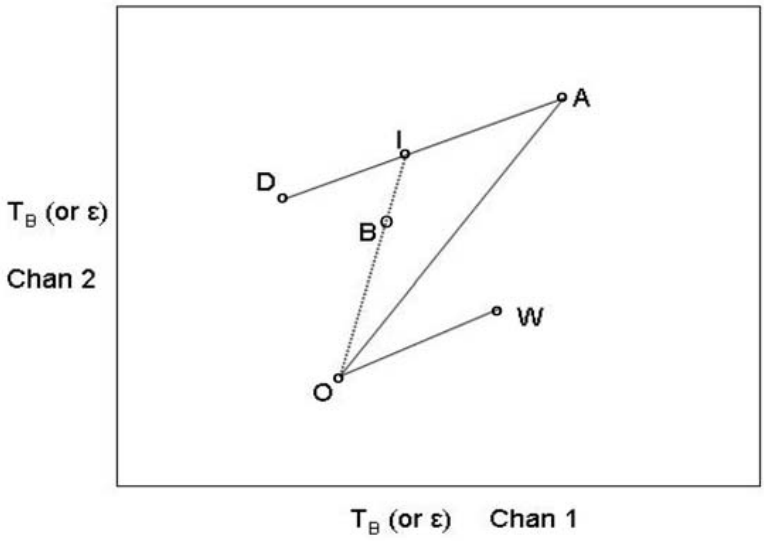

(Markus et al., 2008)

Figure 3: The pattern formed from plotting different polarities of the same passive microwave channel are identified in the figure. Line AD represents 100% ice concentration values, while Line OW denotes 100% water concentration values.

The bootstrap algorithm also makes use of the ≈19GHz vertical polarity band. This band is plotted against the ≈36GHzV channel to make a plot (V1936). The utility in this additional frequency band is the ability to correct for atmospheric effects as the two channels are impacted differently by atmospheric attenuation. The V1936 plot assists by more clearly distinguishing open water which will cluster around the line OA in *figure 3*. By understanding the slope of this line, and visualizing the data in this manner, water brightness temperature values are identified for references. The V1936 plot also better discriminates the ice water interface, as there is a high contrast evident between the emissivity of ice and water in this frequency combination.

When the slope of the line AD is approximately equal to one, the data is thought to correlate well to the variation in brightness temperature for 100% ice concentration. This is due to more substantial differences in the brightness temperature with regard to 100% ice than there is difference in the brightness temperature for 100% water concentration in the VH36 and V1936 scatterplots. In order to better assess

these values, the entire plot is rotated so that the AD line is vertical. With these rotated values, a histogram can be generated to create a probability density function of the ice concentration values (Markus et al., 2008).

This process works best for surveyed areas where there is not a need to apply a land mask or correct for land/water interaction. If these areas exist in a given region, there are different bands/combinations of bands that can be viewed as scatterplots to better model the ice concentration conditions. These methods are applied before a landmask is used to remove land surface from the products.

Advanced NASA Team Algorithm:

The Advanced NASA Team Algorithm (NT2) also uses the ≈19GHz and ≈37GHz bands of passive microwave to identify sea ice concentrations. This algorithm shifts away from using the calculated brightness temperatures, however, and instead uses forms of the polarization ratio and spectral gradient ratios. While both the Bootstrap algorithm and NT2 seek to model sea ice concentration, there are a few significant differences. These differences make the NT2 algorithm more complex than the Bootstrap algorithm, and incorporate more data from outside the passive microwave collections.

While the Bootstrap algorithm still operates using the most basic form of the weighted average algorithm for sea ice concentration (*equation 7*), the NT2 algorithm uses a form that accounts for the variation in ice type. The NT2 models both first-year (or thin) ice as well as multi-year (or thick) ice in the production of concentration values. The baseline algorithm for this model still follows a weighted average form, but has an additional term included.

$$(10) T_{b,obs} = c_{wat}T_{b,wat} + c_{my-ice}T_{b,my-ice} + c_{fy-ice}T_{b,fy-ice}$$

The variation from the standard weighted average equation is because of the difference in emissivity values for multi-year ice and first-year ice. The emissivity difference impacts the calculated brightness

temperature values, so the NT2 algorithm distinguishes between the two in computation, but can also equate it altogether as sea ice for reporting concentrations.

The calculation of sea ice concentration comes from the interpolation of points on a scatterplot of the gradient ratio of ≈19GHz V and ≈37GHz V (GR V1937) and the polarization ratio for ≈19GHz (PR 19). This plot forms a distinctive shape that is then used to interpolate concentration values. The interpolation follows what is known as the NASA tie point triangles (shown below) – a curvilinear triangle that spans between 0% concentration of sea ice and 100% concentration of sea ice.

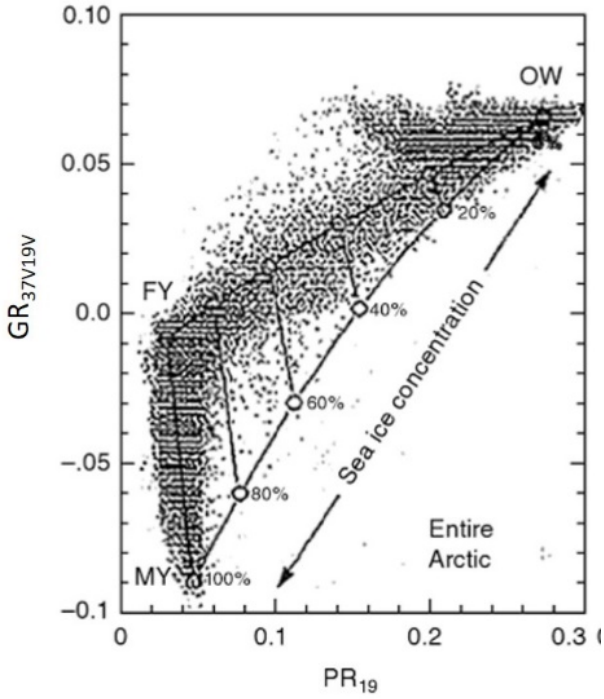

(Shokr & Sinha, 2015)

Figure 4: Advanced NASA Algorithm (NT2) Tie Point Triangle depicts the regions of the scatterplot that correlate to each level of sea ice concentration over the entire Arctic Ocean

The NT2 also makes use of another ratio, known as the rotated polarization ratio. This is a calculated value that attempts to normalize the data for better comparison and correction of surface roughness effects. The rotated polarization ratios adjust the slope of the polarization ratio and gradient ratio plots by an angle (φ) to show deviations from the norm. The equations that govern the rotated polarization ratios are listed below.

$$(11) PR_R(19) = -GR_{V3719} \sin \varphi_{19} + PR_{19} \cos \varphi_{19}$$

$$(12) PR_R(85) = -GR_{V3719} \sin \varphi_{85} + PR_{85} \cos \varphi_{85}$$

The last significant value that is used is the gradient difference (ΔGR). The ΔGR identifies the effects of weather and allows the algorithm to reduce the impact with regard to the tie points.

$$(13) \Delta \mathrm{GR} = GR_{H8519} - GR_{V8519}$$

When these values are used and plotted together, they create a picture of the sea and ice conditions. They identify the thin ice, thick ice, open water, and areas of varying concentrations of ice. The use of these equations, however, takes the algorithm far away from the initial convention of the weighted average.

The algorithm ultimately follows this process: First it identifies brightness temperatures for pure surfaces that represent 100% concentrations of sea water, first-year ice, or multi-year ice. Next it determines the appropriate emissivity value given the surface type by accounting for atmospheric conditions that govern a series of twelve atmospheric variables. According to the variables, the correct emissivity value is applied to calculate a typical reference brightness temperature for the surface. These reference brightness temperatures for the three possible surfaces are used to calculate reference sets at combinations in 10% increments for all combinations of surfaces within the pixels (10% FY_{ice}, 10% MY_{ice}, 80% water; 20%FY_{ice}, 10% MY_{ice}, 70% water; …etc.). These are the possible values for a pixel and are referred to as model values. The rotated polarization ratios and difference gradient values are then calculated for the observed brightness temperatures, and an actual value is determined. This calculated value is compared to the modeled values, and the concentration levels of the closest modeled value is applied for that pixel (using the minimum error technique – square root of the difference between the model and computed values squared) (Shokr & Sinha, 2015).

In this manner the NT2 algorithm does an excellent job at limiting the influence of surface roughness, atmospheric absorption (attenuation) of the passive microwave signal, and atmospheric effects in calculating the concentration of sea ice in a sampled area. It does require a bank of reference knowledge

however, to determine the potential combination values (model values) to serve as a look up table for the computed terms. In comparing the differences in practical terms between the Bootstrap algorithm and NT2, the NT2 is better suited to correct for atmospheric effects (weather) and the tie points are viewed as more representative.

Combining Efforts:

Due to the low spatial resolution of passive microwave products, visible and near infrared satellite sensors are also employed to assess sea ice conditions. These measurements often serve as seasonal enhancements for passive microwave data as they can provide dramatic spatial improvements by functioning at 1-4km resolution as opposed to a 25km microwave resolution. They only serve as "seasonal" enhancements because these frequencies rely upon solar radiation, only present during polar day. Two products developed through cooperation between NOAA and the National Ice Center (NIC) include Interactive Multisensor Snow and Ice Mapping System (IMS) and MASAM2.

IMS uses a combination of satellite sources to provide a more accurate ice product for regional uses by incorporating higher resolution imagery than passive microwave. The system is effective at charting ice-edge at a 4km scale by using a combination of visible/IR imagery, as well as microwave and synthetic aperture radar data. The purpose of this product is to provide daily hemispheric data as to the extent of ice/snow cover for incorporation into numerical weather prediction models, and as a standalone product for ice edge detection/analysis (National Ice Center, 2017).

MASAM2 is a blend of the IMS product from NIC (repackaged by NSIDC as "MASIE – Mulitsensor Analyzed Sea Ice Extent) and AMSR2 sea ice concentration data. This method of product development ensures a more accurate map of where ice truly is in the Northern hemisphere by combining visible/IR observations with passive microwave to assess the concentration as well as the extent (F. Fetterer et al., 2015). The resulting MASAM2 (MASIE + AMSR2) product is a 4km resolution product that incorporates all

available data to establish the initial conditions for ice predictability models. It improves IMS by being reliant upon passive microwave as opposed to visible interpretation of multiple sources and availability of imagery analysts. This product is not limited by ambiguous visible cues, as the passive microwave provides a definitive assessment of the pixel composition.

Error & Uncertainty:

There are many significant sources of error and uncertainty with regard to passive microwave collections and the processing of brightness temperature data into sea ice concentration values. These sources of error include poor calibrations of the sensor for initial collection, as well as charged particle interaction with the spacecraft than can cause a "bit-flip" where data is influenced by a photon and is falsely reported (a bit changes from a 0 to a 1 or the opposite). More substantial errors arise from computational influences.

Tie points are the most substantial source of error in sea ice concentration estimates. This is reflected by the painstaking process the NT2 algorithm uses to identify appropriate values to serve as references for 100% concentration of ice and water. For the Bootstrap algorithm, these tie points are entirely dependent on how well the line AD models 100% concentration of ice (see Figure 3). When the scatterplot generated by comparing different polarities and/or frequencies is rotated so that line AD is parallel to the Y-axis, the correlation of the data to 100% ice concentration is easily visualized (Markus et al., 2008). If points have a normal distribution around this line, the data is likely good, while if the distribution is not focused on this line, the data likely does not correlate well to a 100% ice concentration tie point.

Other errors arise in the data when land masking is applied. Without a land mask, returned values over land do not correlate correctly to their cover type with regard to ice or water. To reduce this inherent confusion, pixels in an image that correspond to land are cancelled. This is effective in improving the meaningfulness of the data, but if the land mask is produced from higher (or lower) resolution imagery, or

if the land/water boundary has changed since the mask was produced, this could be a source of significant errors. Changes in the land/water boundary could occur from glacial calving, erosion, or permafrost melt (Markus et al., 2008).

A significant source of error in concentration use for ice charting is the low spatial resolution of the data. SSMI/S sea ice concentration maps are produced at 25km resolution (each pixel represents 25km x 25km on the surface of the earth). When computed, an area that is 625km^2 is recorded at a uniform concentration. This is known to not be the case, but because this is the level at which the sampling is completed, it is the best approximation of sea ice concentration. Some products are released at 12.5km which reduce this error. Further, the threshold for calculating sea ice area is held at 15% ice concentration. This value was chosen because it is a point at which the satellite data correlates well with *in situ* observations in the arctic. Due to this low threshold and low spatial resolution, a pixel may be included in the summation of ice area, even though only 93.75km^2 are actually present in the 625km^2 pixel.

Data Source & Specifics:

The Geostationary Operational Environmental Satellite – 16, or GOES-16, was launched from Cape Canaveral Air Force Station on 19 November 2016 with the purpose of providing continuous imagery and atmospheric measurements of the Earth's western hemisphere. It also collects and monitors lightning data, space weather, and provides critical data for atmospheric, hydrologic, oceanic, climatic, solar, and space sciences (Leslie, 2016) . The 16th in a series of environmental monitoring satellites operated by the National Oceanic and Atmospheric Administration (NOAA), GOES-16 represents an improvement in spectral resolution, spatial resolution, and temporal resolution.

The satellite has significant utility for all aspects of environmental monitoring. Its broad spectral range across the several onboard instruments allows for effective mapping of atmospheric and surface

phenomena with the potential for raw exploitable data as well as product development for more immediate application. The many products and data available from this satellite's sensors are more effective because of the other aspects of resolution that are improvements over previous iterations of geostationary weather monitoring satellites.

The instrument of interest for this project is the Advanced Baseline Imager, which is the primary payload of the GOES-16 satellite. It is an imaging sensor with sixteen spectral bands covering visible light through thermal infrared portions of the electromagnetic spectrum (John Leslie, 2016). These spectral bands are each centered on particular wavelengths to ensure data collection that can be used to exploit and identify many environmental processes. The satellite operates in a geostationary orbit, giving it the ability to image the western hemisphere every fifteen minutes, the continental United States every five minutes, and at a mesoscale (1000km x 1000km) every 30-60 seconds (Harris Corporation, 2017a). This high temporal resolution allows for near continuous monitoring of environmental phenomena as they occur. The revisit rate supports customers requiring continued updates regarding atmospheric and weather conditions like the transportation industry.

The ABI instrument on GOES-16 is an improvement over the previous version on the GOES-15 platform. Not only has the number of bands increased from five to sixteen, or the revisit rate decreased, but the spatial resolution is also a dramatic improvement over the previous version. With most spectral bands available at 1km (at nadir), and full disk scan at 2km (nadir resolution), the ABI can resolve objects half the size of its predecessor in all bands (Harris Corporation, 2017). Data covering the observed hemisphere is available at fifteen-minute time chips, enabling 96 frames of data per day, and providing the opportunity for effective time sequencing products. While Level 2 products built from ABI data are available from NOAA, the data is also available as Level 1B radiances.

Data

This project uses full disk scans. Before they are subset the center point of the images are 0° North Latitude, and 89.5° W longitude.[2] The data is provided by NOAA in a gridded format that corresponds to a geostationary weather satellite projection. The (x,y) values of each collection file are the east-west (x) and north-south(y) scan angle (in radians) of the sensor to the center of the pixel on the earth. This data is then able to be projected into a latitude and longitude format using the characteristics of the projection ellipsoid (which for this product is GRS80), and the orbital characteristics of the satellite (mainly the height above the ellipsoid). The data, even without conversion into a latitude/longitude format, is provided on a fixed grid so that pixels in subsequent collections are not subject to variations in location due to perturbations of the satellite orbit.[3]

The principle channel of interest for this study is the 2.25µm channel, which corresponds to channel 6 on the Advanced Baseline Imager. The bandwidth of channel 6 is .5µm. This channel and channel 7 (3.9µm) are on different focal planes of the imager which could potentially cause issues with regard to calibration in a dual-channel approach, but that was not evident in the data assessed for this study.

Channel 6 is known as the "Cloud Particle Size" near infrared band and is idealized for daytime applications in snow and cloud regions, and during nighttime for fire applications (GEOS-R Program Office, 2015, p.1). The focus of this project being ice and water, there is no thermal component to the data, so there is little utility for nighttime observations. While 2.25µm is not a sensitive to differences in reflectance between clouds and ice as the 1.6µm band, it is more utilitarian in that the reflectance behavior of ice

[2] Data was collected prior to GOES-16's move in orbit to current positioning over 72.5°W longitude, which began on 30 November 2017.

[3] At the time of this project, the data is restricted and not for public dissemination as there are final tests required prior to public release. To this end, none of the major data processing toolsets has a completely effective means for projecting the data accurately on a fine scale. The "fixed grid" that the data is provided in allows for data processing without projecting, but preprocessing steps require an approximate geolocation that is accurate at the nadir point of the satellite and degrades from there. Future releases of ESRI software will include the ability to project data into and from a geostationary satellite projection that is common with GOES series satellites.

around 2.25µm is comparable to any adjacent frequency ranges, making it a good proxy for an unknown "shortwave infrared" band.

Channel 7 is knowns as the "Shortwave window" infrared band, but for the purposes of this study it is a proxy for "midwave infrared". This band has a thermal component as well as a reflective component, allowing it to provide data during night but exaggerating daytime reflectance values with the addition of this thermal component. This band is used primarily for fire detection, but is also valuable in determining cloud presence during darkness because of the thermal component (GEOS-R Program Office, 2015b).

The study area for this project is Hudson Bay. While Hudson Bay does not lie within the Arctic Circle, the orbital geometry of the GOES-16 ABI limits the utility of "Arctic data" because of the distance from the nadir point and the associated perspective. Hudson Bay is at a low enough latitude that the data is not terribly skewed. Additionally, Hudson Bay is seasonally ice covered sea water, which is sufficient for an assessment of a sea ice detection/characterization algorithm. The data is subset to include only Hudson Bay prior to processing, and then masked using a land mask developed from a GOES-16 ABI Level 2B product: Sea Surface Temperature.

Methods:

While this project was initially conceived as the development of a dual-channel algorithm, the complexity of isolating a reflected signal and emitted signal from channel 7 data, as well as the limited distinguishing characteristics of ice/water data in that band pushed the efforts to focus on single-channel applications. This decision constrained the amount of data available at any given moment for the purpose of surface phenomenology classification requiring more substantive and meaningful preprocessing steps for the channel 6 (2.25µm) data.

The original design of this project used channels 6 and 7 from GOES-16 in a normalized difference algorithm to distinguish ice from sea. This ultimately proved to be an unreliable venture because of the

minute distinction in albedo between ice and water in these SWIR wavelengths as well as the complexity of the channel 7 (3.9μm) data. Because channel 7 is comprised of both thermal and reflected radiance values (which proved extraordinarily difficult to isolate without additional data channels) the data, when compared in an algorithm, did not divert in exploitable ways. On its own, the channel 6 data demonstrated much more utility for sea ice detection, and ultimately the project moved in the direction of a single-channel approach. This decision also simplified future applications with other datasets as single-channel data sources are thought of as reliable, while multichannel sources may be less common.

Data Preprocessing:

Single-channel remote sensing techniques were established in the early days of remote sensing as a means to extract as much meaningful data as possible from a limited data source. With the prevalence of multi-channel sensors, the need to tool data to be more substantive diminished as more complicated problems could rely upon additional data from other portions of the electro-magnetic spectrum. This has ultimately resulted in a decrease in the focus of pulling as much information out of each available data set as possible.

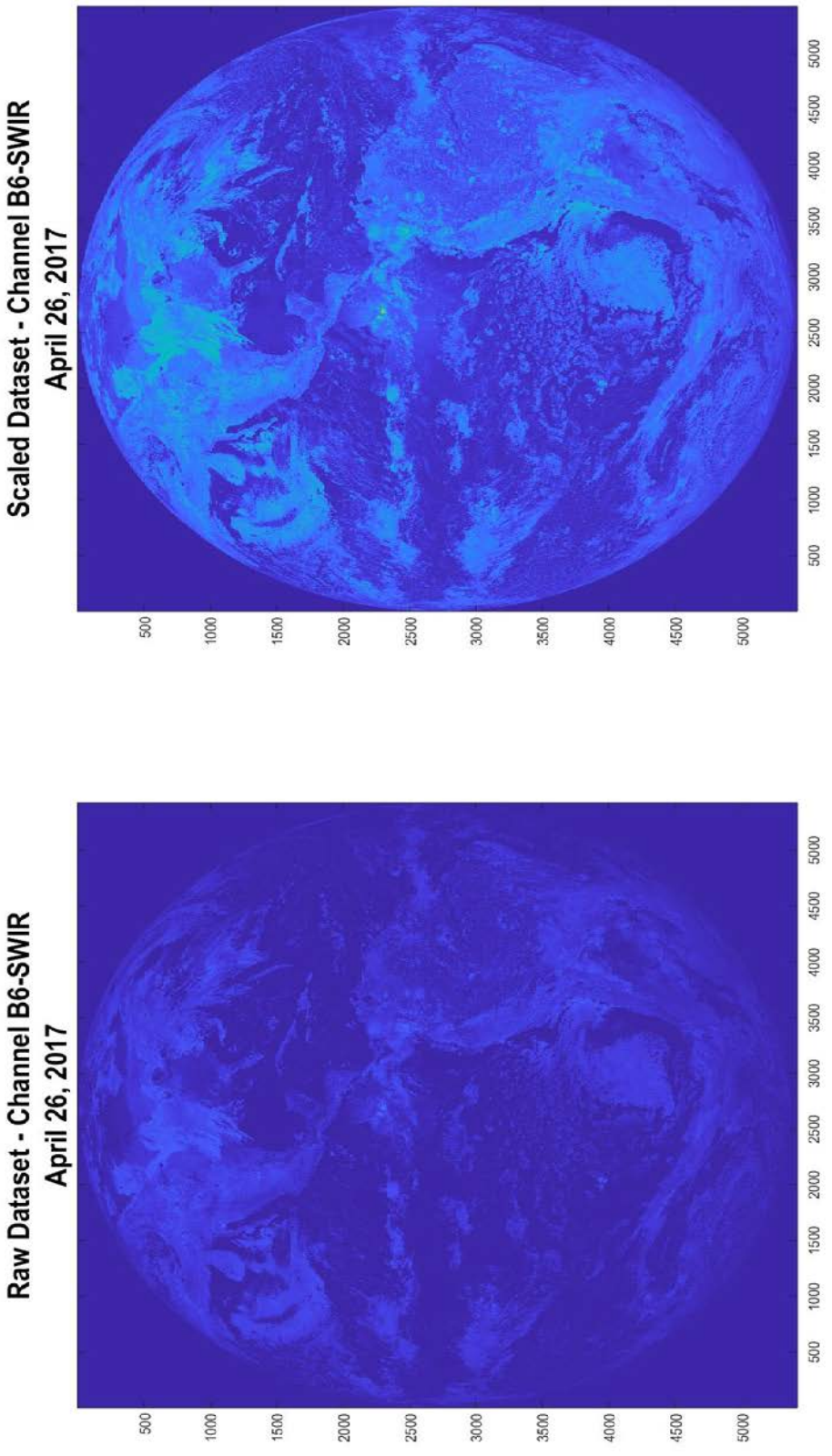

Figure 5: Raw datasets from GOES-16 Band 6 (2.25micron). Scaled image allows for enhanced visual interpretation. (The poor contrast in the images is intentional and intended to show the inherit difficulty in exploiting a single-channel SWIR sensor).

For this project the data is extremely limited because it is focused on a single-channel. Preprocessing is therefore a means to create more meaningful data by influencing the collected radiance values provided in the Level 1B data source and tailoring it to better suit needs. Prior to this data enhancement, traditional methods for data preparation were conducted.

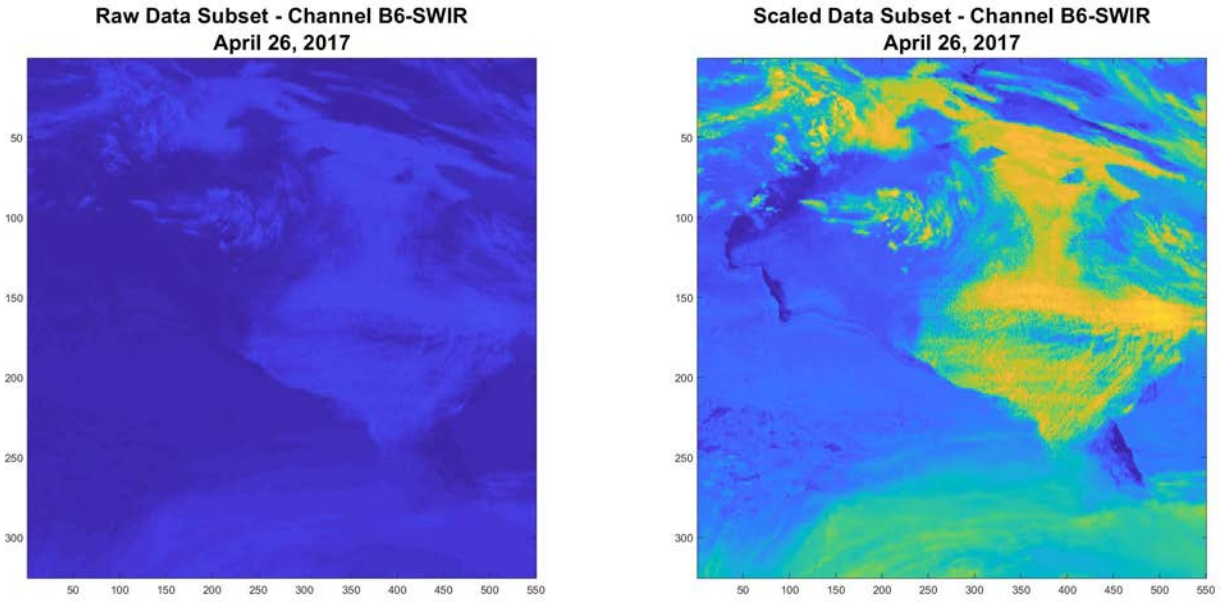

Figure 6: Subset of the study area is shown. Left image shows natural contrast present in raw data - notice that Hudson Bay is indistinguishable. The right image is scaled to enhance contrast. (Poor contrast is again intentional [left] as it depicts the original data set well).

Hudson Bay Subset

The first step in preprocessing was to subset the image from a 5424x5424 pixel image into a 325x550 pixel box around Hudson Bay. The subset scene represents only 0.6% of the original full disk image. This fraction is visually displayed in figures 10 and 11. This step also assists in improving the contrast that allows the ice and water to be distinguishable from one another as well as reducing the overall number of pixels for subsequent calculations. As other regions are removed from the target area, the variability in radiance is greatly reduced, allowing for improved contrast enhancements between the radiance values which remain.

The data from multiple time slices is combined into a data cube for further processing. The cube's four dimensions include the X component, Y component, Z (radiance) component, and lastly the time component. By layering and packaging the data this way, locations remain consistent and time steps are more easily processed simultaneously.

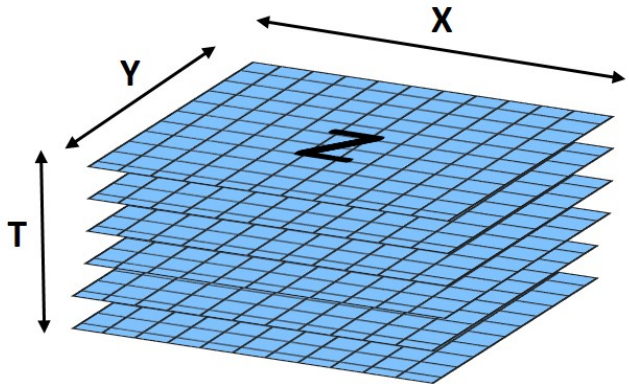

Figure 7: Data cube structure. The Z values represent the satellite reported radiance from the Level 1B product, T is the time component, while X and Y combine to determine the location of the pixel in physical space.

Once the data is subset, a land mask is applied to the data to ensure that the remaining pixels are only those that are located over the water features of Hudson Bay. A land mask was not readily available, so one was developed from the Level 2 Sea Surface Temperature product for GOES-16. A full disk image of the SST product was reduced to the same subset as the study area, and then used to mask out any land features in the Hudson Bay Subset. All reported pixel values (water) in the SST product are changed to a 1 while all masked pixels (land) are reduced to zero. When this "land-mask" image is multiplied by a valid data set, only the region of interest (water on Hudson Bay) remains. Zeros are then converted to "NaN" values (not-a-number) so that they are not included in future mathematical processes.

In the subset images, the size of the pixels is not consistent with regard to their spatial representation. This is a result of the unique geometry of the GOES-16 constellation, and the high latitude location of Hudson Bay. A quick assessment of the size of Hudson Bay and its representation in the subset images shows that pixels represent approximately 2.1km x 4.6km. The stretch in the y-direction is a result

of the nadir position of the satellite (at 0° N latitude) when compared to Hudson Bay which is centered at approximately 60° N latitude.

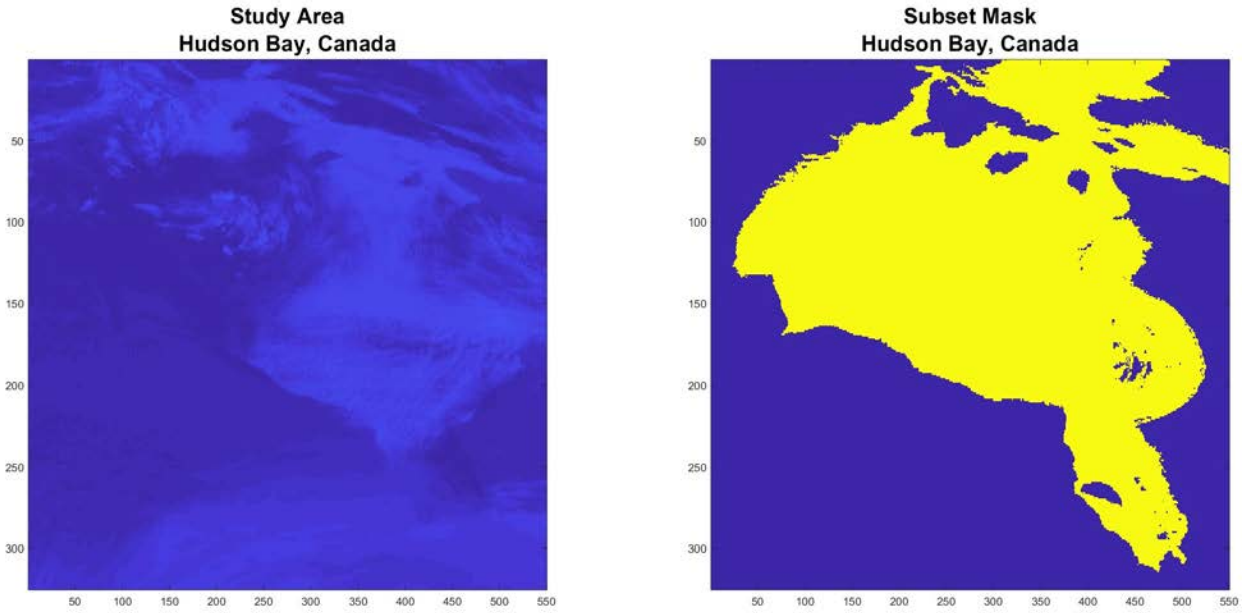

Figure 8: The land mask (right) is applied to the study area scene in order to increase ability to decipher surface phenomena in a single scene. It also removes ambiguity with regard to surface type (as "surface" can only be land/water - or atmospheric effect).

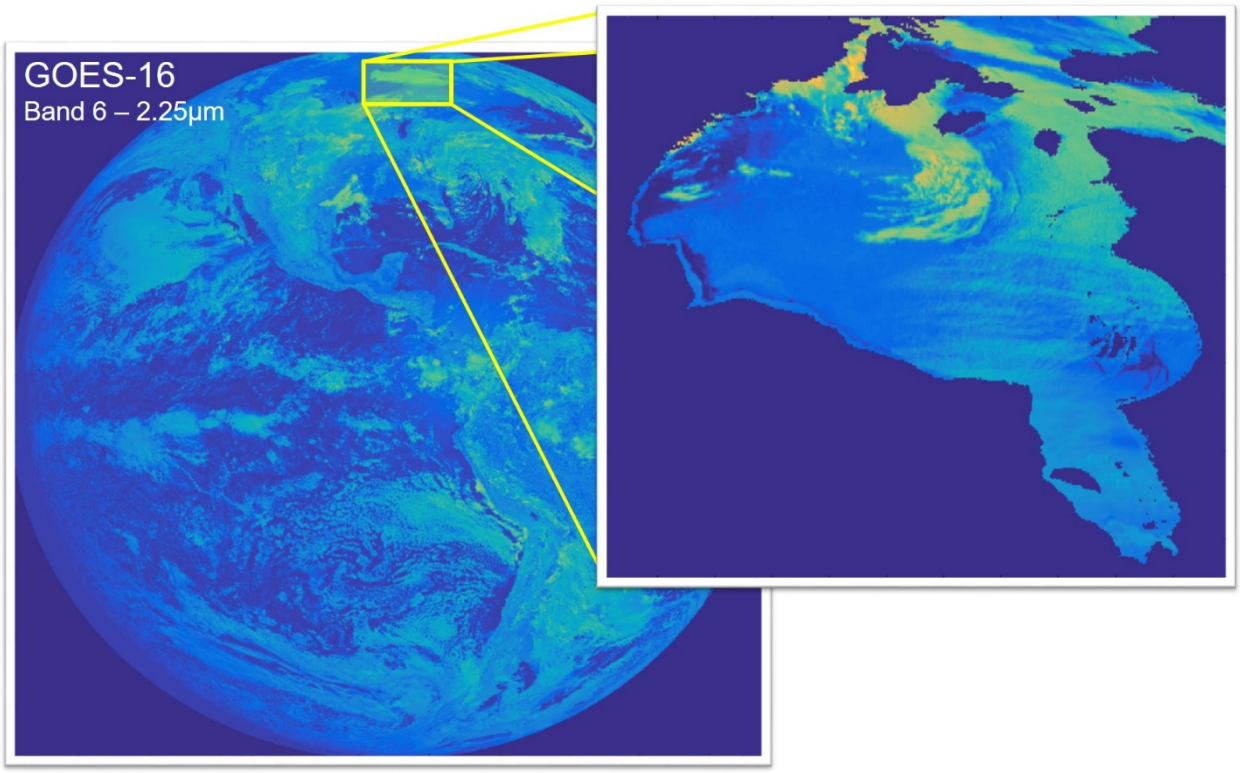

Figure 9: Full disk image of band 6. Subset of Hudson Bay after land-masking and contrast stretching enhancements are applied.

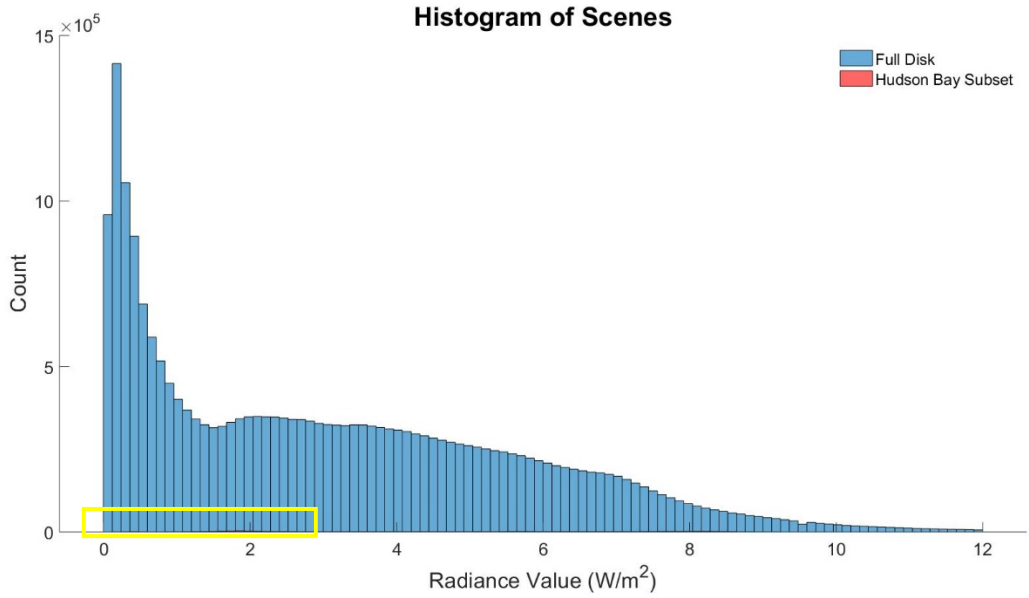

Figure 10: Histogram of the full disk scan from 26 April 2017 at 12:00pm local yellow box denotes area of the graph below. (Red values depicting the Hudson Bay Subset are indistinguishable at this scale because they comprise such a small portion of the full-disk data set).

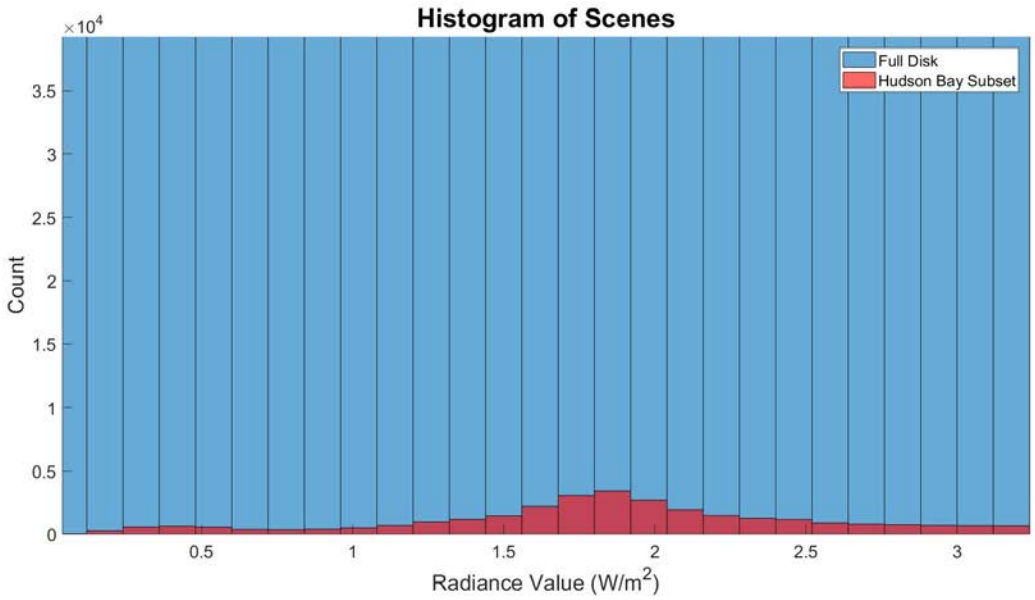

Figure 11: Same histogram as shown above, zoomed in to show the pixels that make up the Hudson Bay Subset scene.

Sun Angle Corrections:

The high latitude of the subset region coupled with the variation in the time of image collection creates a substantive sun influence variation throughout a single time series as well as between monthly collections. To minimize the influence of the sun's differing perspective throughout the test images, a sun angle correction is performed for each pixel in the subset scene. Using a matrix of latitude and longitude that correlate to each of the pixel points, as well as the start date and time of the image capture, an additional matrix is created that is comprised of the solar zenith angle for each pixel. This is used to normalize the data for solar influence by multiplying each pixel by the cosine of the zenith angle (θ).

$$(14)\ \theta = \arccos(\sin\emptyset \sin\delta + \cos\emptyset \cos\delta \cos\omega t)$$

$$\emptyset = \text{latitude}$$
$$\delta = \text{solar declination}$$
$$\omega t = \text{hour angle}$$[4]

[4] Hour angle is determined by converting the time of day to a number that represents hours from noon as a decimal and then multiplying this value by 15°. (10:30 am local time is therefore -1.5 hours from noon. $-1.5\ x\ 15^{\circ} = -22.5°$)

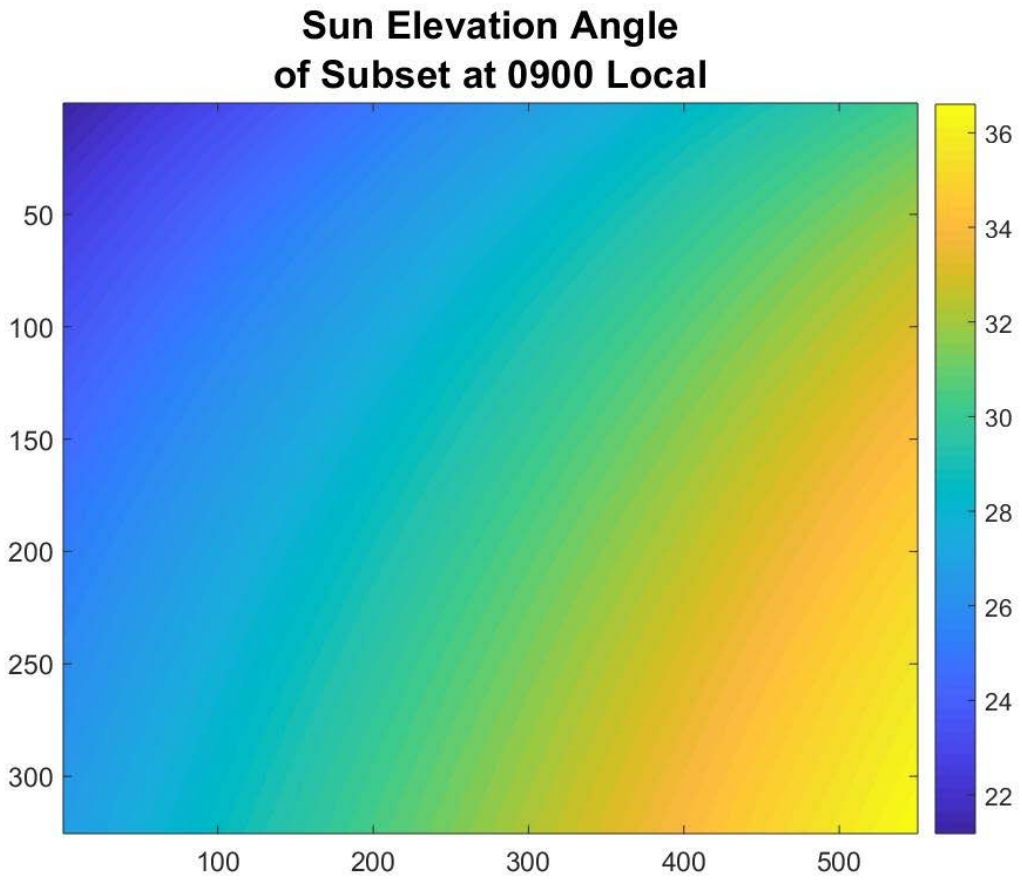

Figure 12: Sun Elevation Angle of Hudson Bay Subset scene. Image depicts the sun angle for each pixel at 0900 Local time (1400GMT). Difference in sun angle for scene exceeds 14°. This difference equates to a 12% difference in W/m^2 given an identical TOA radiance.

While efforts are made to reduce sun angle influence, this technique only improves radiance reporting by attempting to normalize the data through time. It does not correct sun angle influence completely and the remaining influence of sun angle will likely continue to pose a problem throughout a sensitive classification scheme. Additionally, surface roughness is not accounted for in this model, but may have a substantive impact on reported radiance. The large pixel size assumes a flat surface, but micro-terrain within a pixel can skew radiance values as scattering and reflecting regimes change over short distances. This unaccounted for surface roughness combined with the legacy (or remaining after correction) influence of sun angle likely contribute to the remaining variance in pixel radiance among pixels with similar surface conditions.

Atmospheric Correction:

In order to reduce the changes in atmospheric contributions to include path irradiance, a dark object subtraction correction was applied to all data sets. To accomplish this effort, the data is converted into a vector, and the minimum value pixel is reduced to zero by subtracting the minimum pixel value from every pixel within the scene. This step is performed after land masking to ensure that no significant pixel (one over water) is converted to a NaN value as part of the land-masking process (which takes all zero values derived from the mask and converts them to NaNs). This process assumes that the darkest pixel in the scene likely has a reflectivity of zero, but because of atmospheric contributions, that value is recorded as greater than zero. While this is an assumption, because of its equal application across the single image, as well as the individual application for all images in a time-series, the data is more closely normalized through time.

These pre-processing steps assist in improving the histogram distribution and create a more stable histogram that is less influenced by solar zenith angle or atmospheric contributions to the captured scenes. This ultimately improves the ability to characterize surface phenomena throughout a daily time series as well as a seasonal time series. The more stable an image's histogram is throughout a time series, the more likely a classification algorithm will be successful and accurate in categorizing data. The point at which histograms change significantly with regard to scene distribution (clustering) and radiance drifting (recorded radiance for similar surface conditions) will determining the effective time scale of a specified classification scheme.

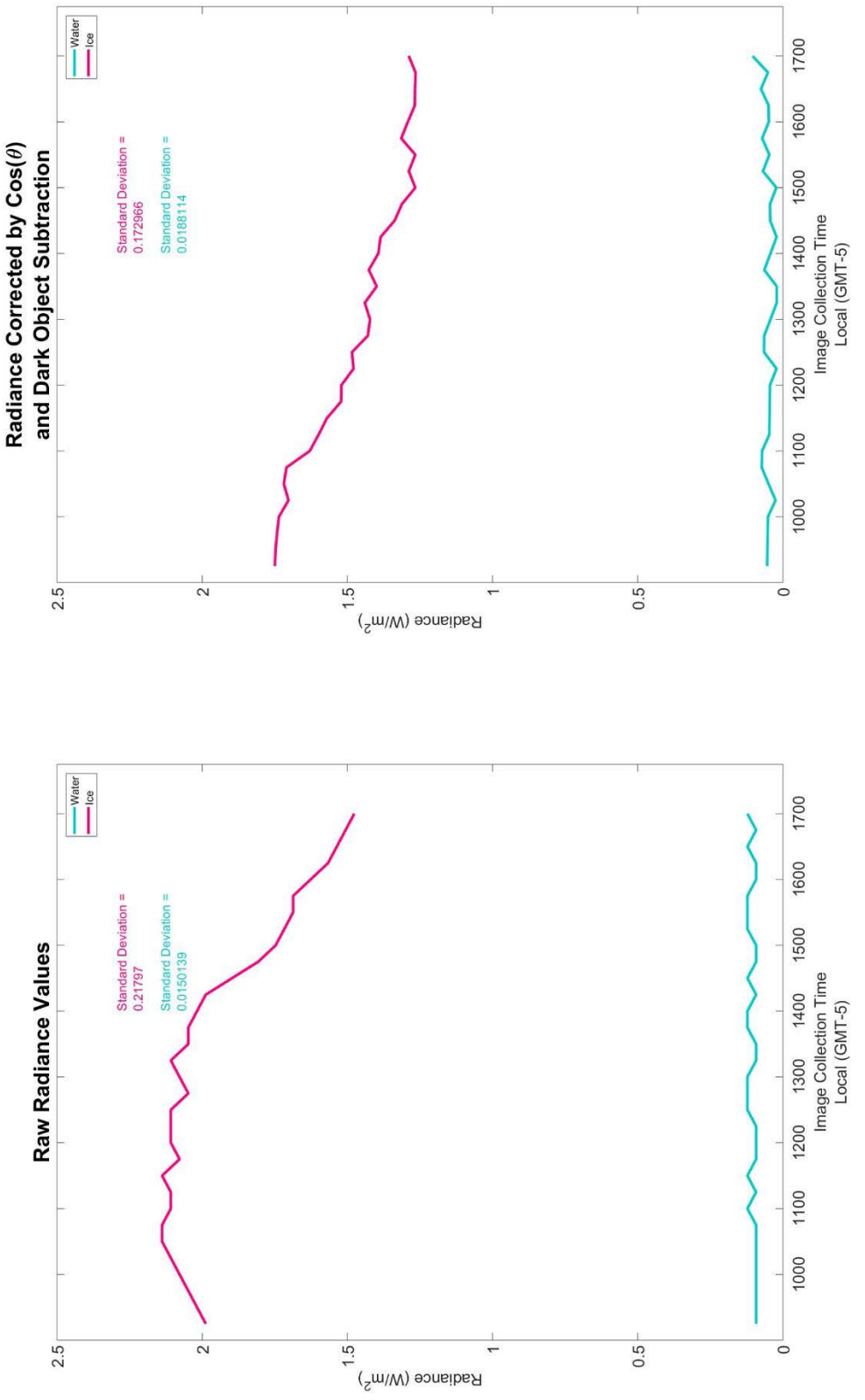

Figure 13: Graphs show single pixel (one for ice, one for water) before and after sun angle correction & dark object correction. Data from April 26, 2017.

Dark Object Values

Atmoshperic Correction Applied to Each Frame

		February			March				April						May			June		
Dark Object (Minimum values from Image)	Frame	Day 044	Day 045	Day 046	Day 047	Day 072	Day 073	Day 074	Day 075	Day 115	Day 116	Day 117	Day 118	Day 119	Day 133	Day 134	Day 136	Day 165	Day 166	Day 167
	1	0.029791	0.030041	0.029932	0.030067	0.028501	0.0282	0.028127	0.028282	0.053447	0.024756	0.026886	0.024501	0.026077	0.019124	0.023705	0.023149	0.021944	0.024457	0.023041
	2	0.03008	0.029979	0.029823	0.029773	0.028281	0.02787	0.027804	0.027912	0.026361	0.026671	0.026421	0.026624	0.025695	0.019158	0.023088	0.022401	0.021527	0.024152	0.022505
	3	0.030075	0.0299	0.029558	0.029653	0.027955	0.027661	0.02742	0.027572	0.025975	0.026187	0.025918	0.025964	0.025317	0.019321	0.022417	0.021521	0.020767	0.023547	0.021962
	4	0.030012	0.029804	0.029655	0.029528	0.027423	0.027343	0.027219	0.027203	0.025281	0.025594	0.025434	0.025634	0.024925	0.019546	0.021834	0.020804	0.020127	0.023102	0.021613
	5	0.030001	0.029685	0.029532	0.029392	0.027288	0.026693	0.026756	0.026804	0.025803	0.02514	0.024964	0.025469	0.024579	0.019815	0.021225	0.019958	0.019483	0.022784	0.020824
	6	0.028456	0.02955	0.029104	0.029461	0.02696	0.026324	0.026579	0.026442	0.076216	0.024759	0.024453	0.021416	0.024493	0.020067	0.020594	0.019257	0.018816	0.022277	0.020565
	7	0.028181	0.029448	0.029284	0.029129	0.026661	0.026254	0.026224	0.026095	0.024188	0.024287	0.02391	0.024683	0.024156	0.020401	0.020017	0.018666	0.018169	0.021896	0.020271
	8	0.056088	0.23853	0.028795	0.029001	0.02636	0.025637	0.026099	0.025768	0.023871	0.023719	0.023522	0.024268	0.023844	0.020519	0.019551	0.018026	0.017586	0.021533	0.020007
	9	0.056099	0.029339	0.029048	0.028889	0.025865	0.025689	0.025738	0.02522	0.047209	0.023054	0.023013	0.019966	0.023085	0.021148	0.018781	0.017453	0.017051	0.021005	0.019503
	10	0.05596	0.028936	0.028949	0.028766	0.025597	0.025071	0.025527	0.025011	0.023345	0.022753	0.022494	0.023551	0.022683	0.021619	0.018585	0.01708	0.016647	0.020727	0.019337
	11	0.027915	0.058908	0.028409	0.028673	0.025642	0.025145	0.026965	0.024817	0.023149	0.022405	0.02222	0.019108	0.022318	0.022103	0.018505	0.016645	0.016572	0.020357	0.019075
	12	0.027879	0.056547	0.057547	0.028599	0.025465	0.024979	0.026722	0.024717	0.023	0.021838	0.021779	0.02297	0.022024	0.02248	0.018673	0.016398	0.016268	0.020194	0.018864
	13	0.055777	0.02936	0.057458	0.028544	0.025351	0.024848	0.024951	0.024643	0.022866	0.019463	0.021432	0.018752	0.021756	0.023032	0.018375	0.016294	0.016133	0.019759	0.018749
	14	0.027912	0.029329	0.028689	0.028511	0.025268	0.025152	0.024879	0.024622	0.022818	0.02155	0.021413	0.022521	0.021541	0.02367	0.018396	0.016195	0.016057	0.01954	0.018706
	15	0.027878	0.028296	0.028652	0.027619	0.025245	0.024747	0.024822	0.024749	0.022822	0.019623	0.021094	0.022375	0.021399	0.02416	0.055668	0.020533	0.016135	0.019959	0.018652
	16	0.028059	0.028365	0.028677	0.027542	0.025239	0.024767	0.024819	0.024871	0.02271	0.020928	0.020908	0.022284	0.018917	0.024693	0.018874	0.016501	0.016223	0.019253	0.018629
	17	0.056344	0.028383	0.057394	0.027581	0.025315	0.024863	0.024881	0.025063	0.023107	0.019916	0.021268	0.022323	0.021281	0.025752	0.019462	0.020355	0.016555	0.019508	0.018623
	18	0.056639	0.029274	0.08508	0.028601	0.025428	0.024991	0.024994	0.025299	0.023059	0.020855	0.020923	0.022343	0.019585	0.026232	0.019387	0.020467	0.016919	0.019357	0.01515
	19	0.028863	0.029354	0.028343	0.027854	0.025576	0.025184	0.025178	0.025897	0.02343	0.020949	0.021302	0.022437	0.019959		0.020482	0.020505	0.017839	0.03875	0.018309
	20	0.029588	0.058963	0.028865	0.027905	0.025796	0.025413	0.025341	0.026208	0.023504	0.021081	0.021169	0.022544	0.021609		0.020717	0.020851	0.017864	0.020292	0.018973
	21	0.029085	0.089059	0.028573	0.028135	0.026017	0.025681	0.025595	0.026562	0.023807	0.021293	0.021451	0.022381	0.021824		0.021208	0.018665	0.018415	0.020586	0.019283
	22	0.029752	0.030002	0.028804	0.028983	0.02629	0.025982	0.025874	0.026912	0.023616	0.021576	0.021553	0.022933	0.022657		0.021251	0.021059	0.019019	0.019983	0.019542
	23	0.029648	0.029924	0.02895	0.028435	0.026584	0.026309	0.026183	0.027273	0.023857	0.021902	0.021849	0.023236	0.022746		0.021604	0.020244	0.019896	0.021009	0.019937
	24	0.029543	0.029892	0.029103	0.029242	0.026897	0.026786	0.026526	0.027642	0.024131	0.022276	0.022296	0.023564	0.023355		0.022029	0.020962	0.020258	0.021073	0.019126
	25	0.030082	0.030026	0.029305	0.029361	0.027224	0.027015	0.026878	0.027996	0.024453	0.022691	0.023149	0.023532			0.022496	0.021691	0.020935	0.02178	0.020793
	26	0.030083	0.030088		0.029513	0.027564	0.027377	0.027235	0.028344	0.023595	0.023147	0.023578	0.02506			0.022962	0.022428	0.022082	0.022369	0.021217
	27	0.030013	0.030061		0.029612	0.027889	0.027741	0.027601	0.028667	0.024185	0.023651	0.024084	0.024318				0.023958	0.022307	0.022882	0.02174
	28	0.030033	0.030054		0.02973	0.028195	0.028099	0.027957	0.028854	0.02548	0.024202	0.025023	0.025196				0.024445	0.023045	0.023356	0.022281
	29	0.029995	0.030016		0.029932	0.028374	0.028439	0.02807	0.029249	0.025729	0.024642	0.025631	0.025623				0.024905	0.023708	0.023845	0.022845
	30	0.029931	0.029978		0.029941	0.028808	0.028762	0.028329		0.026216	0.02514	0.02594	0.026005				0.02543	0.024122	0.024326	0.023414
	31				0.030008	0.028891	0.029053	0.028584			0.025548							0.024695		0.023742
	32				0.030012	0.029121	0.029316	0.028835			0.026122							0.025144		0.024305
	Mean	0.034659	0.04137	0.034701	0.029	0.026783	0.026481	0.026522	0.026507	0.027574	0.023054	0.023169	0.023386	0.022743	0.021824	0.021919	0.020228	0.019447	0.022122	0.020362
	St Dev	0.010774	0.038939	0.013809	0.000761	0.001246	0.001398	0.001217	0.001434	0.011231	0.002011	0.00186	0.001938	0.001859	0.00225	0.006937	0.002622	0.002774	0.003475	0.001953

Figure 14: Dark Object values for every frame of test data. Daily mean and standard deviation values are provided.

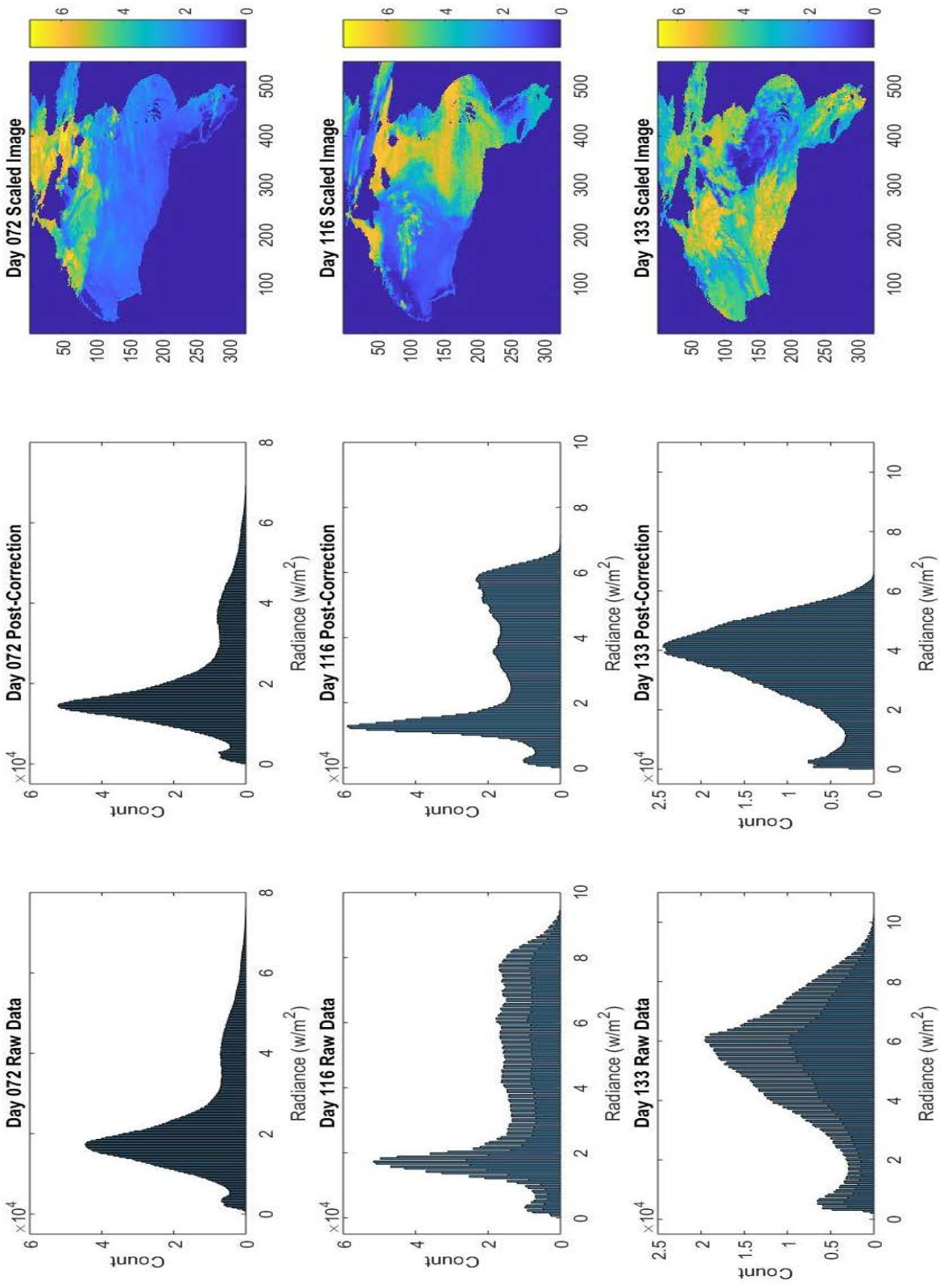

Figure 15: Histograms (and corresponding images) for raw data and pre-processed data (using sun angle correction and dark object subtraction).

Snow on Sea Ice – constraining the problem:

Both snow and ice have a high albedo for visible wavelengths, but this is significantly attenuated in short-wave infrared frequencies. Despite this significant drop in reflectivity, grain size of snow particles still has an influence on albedo. This difference can account for a 10% increase or decrease depending on the surface cover. While this difference exists particularly between fine-grained snow and bare sea-ice, this project assumes that any snow on the surface is quickly metamorphosed into medium to coarse grain snow because of the significant temperature gradient between the underlying water and the atmosphere (Sturm, 2002). So while there may be spikes in reported radiance values following a snowfall event, these values should quickly return to a normal snow-on-sea-ice range because of the kinetic metamorphism that occurs regarding the snow grains.

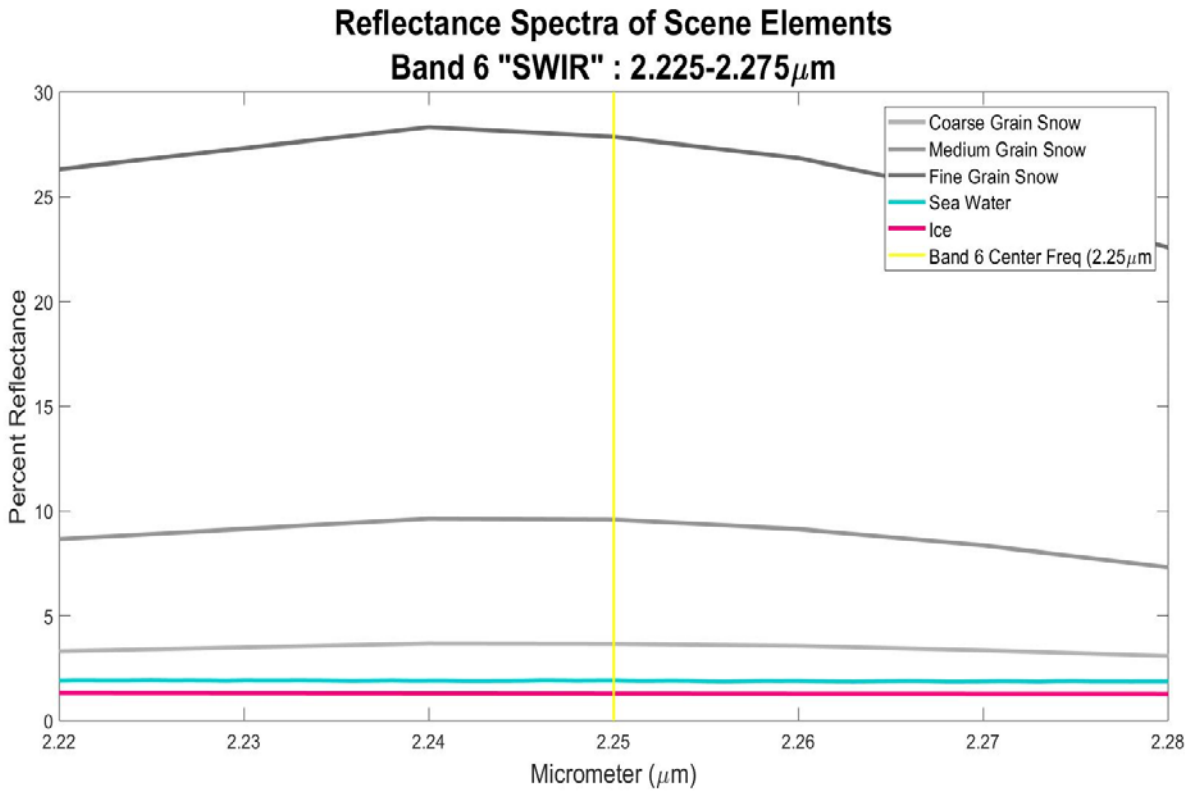

Figure 16: Spectral reflectance of different surface mediums over bandwidth of GOES 16 Band 6 (2.25microns). (Hook, 2017)

Classification:

The initial classification algorithm uses k-means clustering for "k" number of classes. In order to execute the classification schema, a number of classes is specified. The function (which is built into MatLab) then uses this number of classes to partition the data into the most likely class by minimizing the distance between the class centroid and the underlying data. This occurs many times until each distance between data point and cluster centroid is minimized, and the classes are approximately of equal size. Because this clustering technique requires classes to contain values that are equidistant to determined centroids, the number of distinct classes must be greater than the number of distinct scene elements. This is the case for a distinction between ice/water and ice/cloud as these "classes" are very similar. By implementing extra classes that the algorithm can use in order to discern more distinct (or discrete) classes, the result is several "classes" that represent similar surface/atmospheric medium. While the underlying images contain pixels with values representing ice, water, or cloud, in order to get a quality discernment between surface/atmospheric classes there needs to be between 5-8 distinct classes for clustering. This means that K equals 5+, and several classes of data are representative of the same surface medium.

The data for classification is very limited given the pixel size and study area. Two methods are assessed in this project, one which moves forward in the data limited environment and one which seeks to compensate for it. The first develops a classification scheme by using a "snapshot in time" – using a single image in the classification algorithm, and applying the results to the target data. The second method attempts to increase the quality and reliability of the classification scheme by combining three subsequent images into a single data array. This data set (with three values for each pixel location) is then used for k-means clustering. This yields a product that uses 45 minutes worth of data (three images taken 15 minutes apart), rather than a single value representing a singular 15-minute period. This is tested to determine if it improves discernment in cloud versus ice classification as well as ice versus water classification. Combining

this time series increases the classification training data set from 178,750 pixels to 536,250 pixels (or 178,750 x 3).

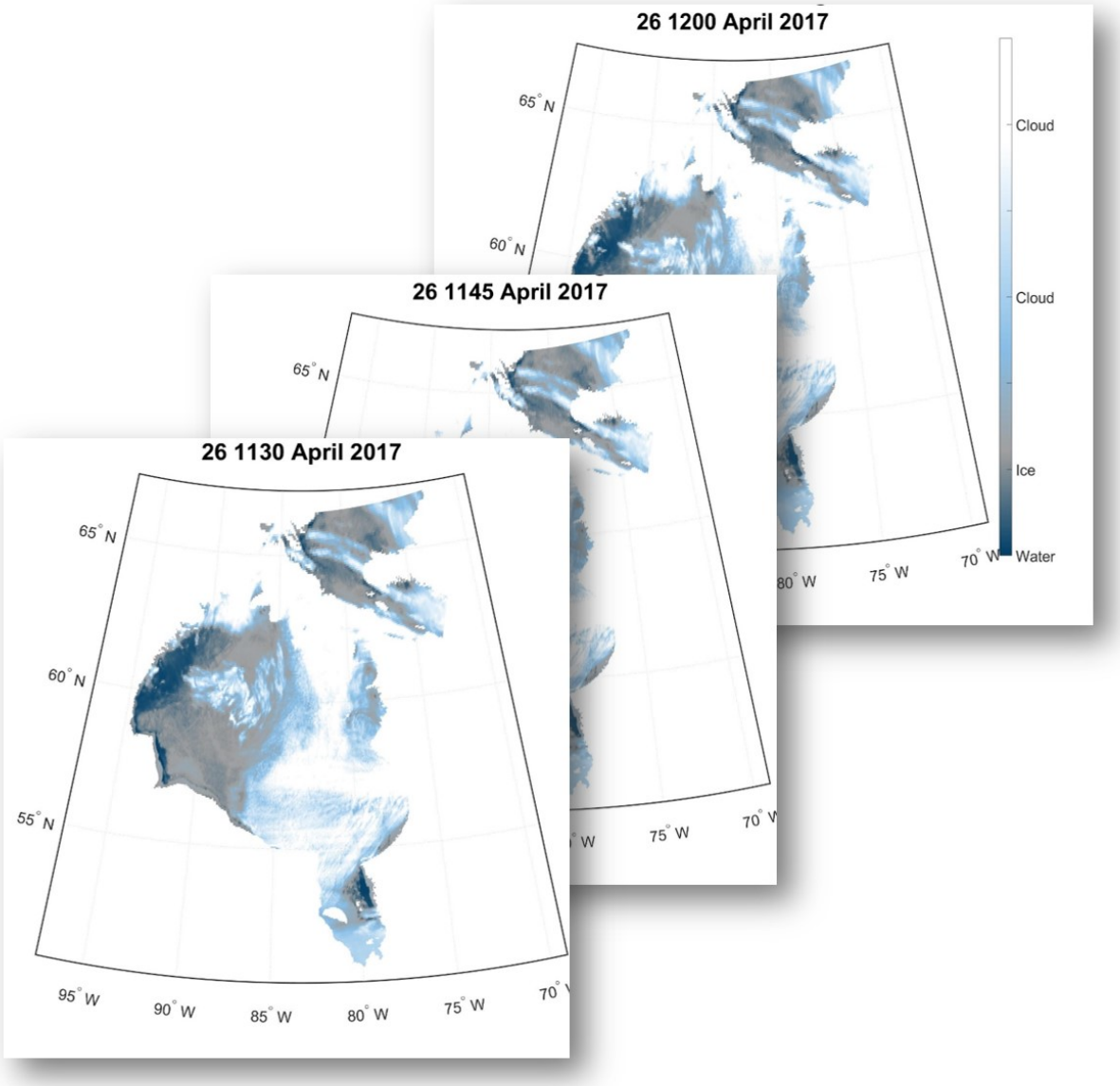

Figure 17: 3-images in a time series used to increase data available for the development of the classification schema through k-means clustering.

The initial classification of training dataset (either the "snapshot in time" or the 3-image time series) yields a single classification schema. This schema is a binary decision tree that ultimately identifies a pixel value from subsequent images, and filters through the decision tree until the class number of the pixel

is determined. While a single image classification scheme may have 5-7 decision points on the decision tree, a combined 3-image set can have 50 or more decision points increasing the specification of class determination. This binary decision tree is then applied to each of the images in a time-series data cube that was corrected for both atmospheric contribution as well as sun angle.

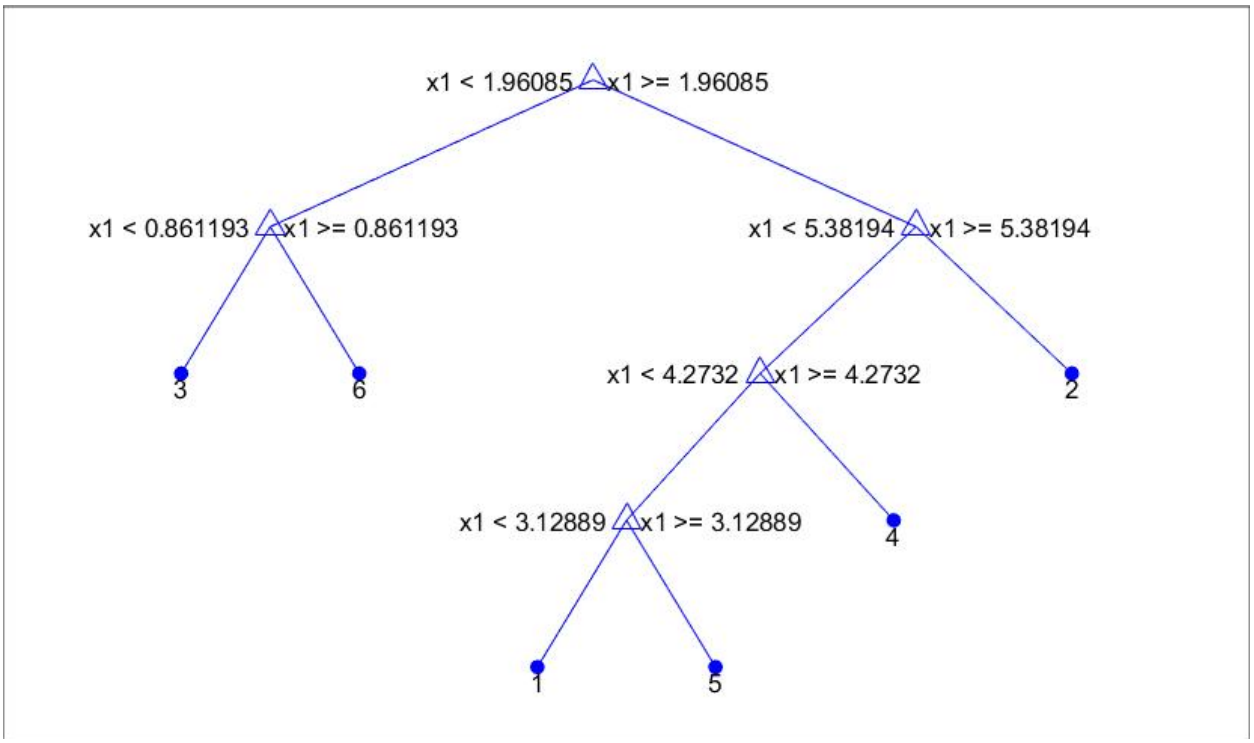

Figure 18: Binary Decision Tree for classification schema using a single image as the basis of classification. This decision tree has five decision points. A decision tree from a 3-image series has 50+ decision points (denoted by a triangle). At each decision point, moving down the 'tree' Right is "True", Left is "False".

Post classification, the user must identify the specific classes and correlate them to surface features (ice, water, cloud). This process is not a part of the classification algorithm, as the program only looks for the best pattern within the underlying data, but is unaware of the meaning applied to each of the classes of data. This is a process that can likely be automated in future work with the incorporation of machine learning or hierarchical agglomerative clustering (but there is a tradeoff with significant computational requirements). Users can accomplish this task, by looking at an image used for development of the binary decision tree prior to classification. The data clustering should be congruent with visual interpretation of

the image (previous ice conditions, shape of feature, relative motion of feature) and after initial application will remain consistent through the entire time-series data cube.

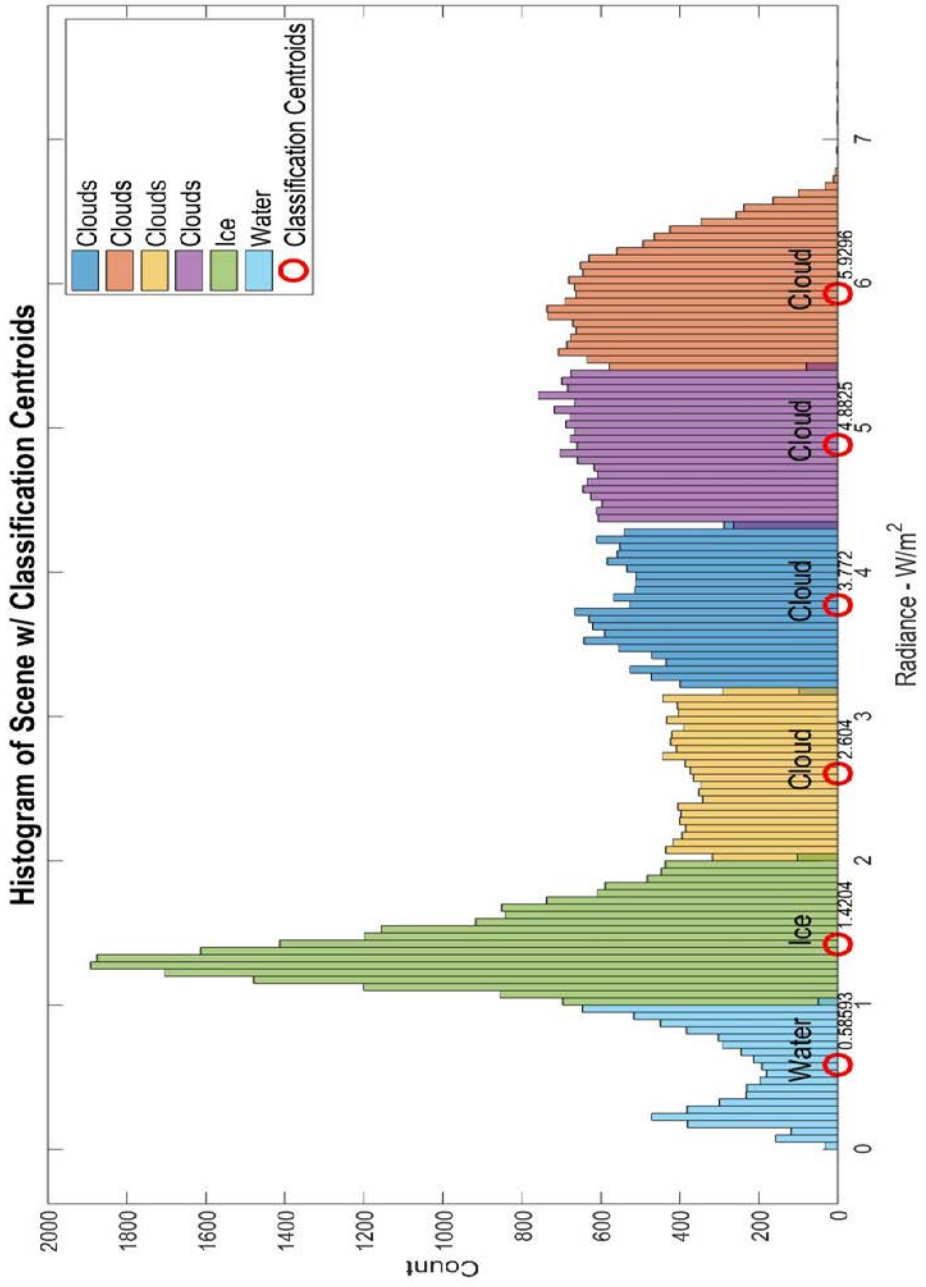

Figure 19: Histogram of Day 116 (noon) w/ breakdown of classification and centroids that determined classification scheme.

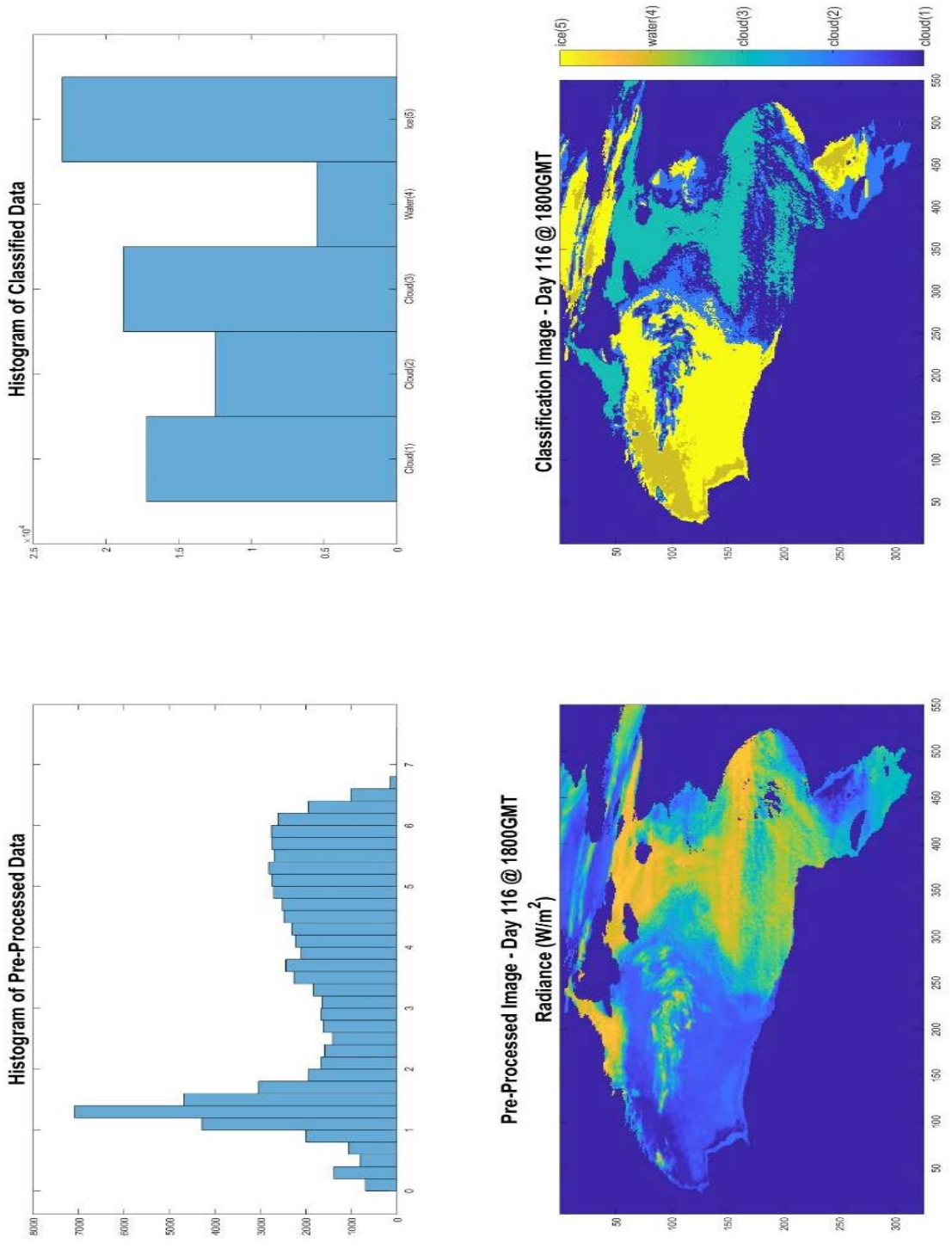

Figure 20: Histograms and corresponding image scenes for pre-processed data (left) and classified data (right).

Validation Method:

While many products that assess sea ice conditions exist, the temporal scale of this product exceeds any currently available. In order to validate the results of the classification schemas, classified images were initially compared to MASIE NH data for Hudson Bay (Region 10). When the MASIE data showed no significant structure in the ice (i.e. the scene is completely ice covered), visible MODIS imagery is used as a visual check to ensure that the classification schema is performing adequately. Statistical metrics were not used to assess accuracy of classification models because direct comparisons to other derived products are difficult given the difference in temporal resolution, spatial resolution, and atmospheric conditions at the collection time.

Metrics of ice covered / open water percentages were not used because of the cloudy nature of the GOES-16 imagery. While the MASIE product shows only a binary product (ice or water) in the Hudson Bay, the nature of the GOES/MODIS imagery is such that there are a large percentage of pixels that are not able to be classified because of their obscuration by clouds. This ultimately eliminated MASIE as a reasonable resource for validating results of the GOES-16 product. Instead MODIS imagery is used to provide a cursory check that the classification appears to be similar to what visible imagery from the day shows. This method was deemed sufficient given the exploratory nature of this product and the level of detail evident in the ice structure in the MODIS data.

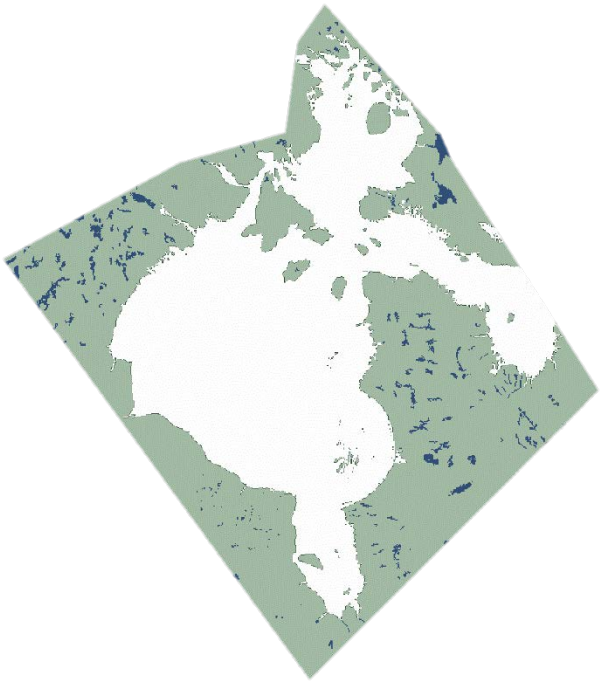

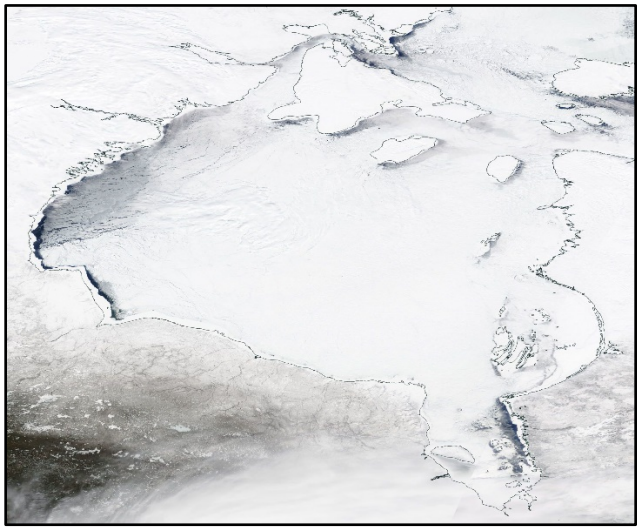

(National Ice Center and NSIDC, 2010) *(*EOSDIS - NASA Worldview, *2018)*

Figure 21: MASIE-NH Region 10 (left) and MODIS visible imagery (right) for April 26, 2017. Because MASIE shows complete ice cover for the time period, the MODIS imagery is used as a visible check to ensure quality of the binary decision tree schema.

Results:

Most of the results are generated from the March and April data sets as these were of the highest quality and offered the most consistency in a time series acquired from NOAA. The quality of the data is determined by its consistency in time (a collection is available for every 15 minute period) and is most representative in its mix of surface types (clouds, water, ice). Much earlier in the season there is very little open water and much later in the season there is very little ice which complicates training a classification algorithm. Additionally, the May data set is limited because not all collections were available from NOAA for unknown reasons (significant gaps of 2-4 hours in the 15 (minute time series). Other monthly data sets have high concentrations of clouds which limits the usefulness of a classification product.

Technique Comparison:

To assess the utility of a 3-image time series for classification schema development, this technique was compared to a single-image classification schema development model. Each technique had strengths and weaknesses when compared to the other, but both methods informed similar conclusions with regard to follow-on processing. Because of the difficulty in developing an unbiased metric for validation, visual interpretation of the classified images and the enhanced data was conducted to determine the best technique. Both methods require similar timelines (less than one minute of processing time), and the only substantive difference was the complexity of the binary decision tree used in the model which is a function of the increased data input for the 3-image time series approach.

To test the two techniques, classification schemas were developed for each method on each of four days (April 26 (116), April 27 (117), March 13 (072), March 14, 2017 (073)). These classification schemas were then applied to images captured by GOES-16 at +1 hour, +3 hours, and +5 hours. Each of the classified images was subjected to the same pre-processing previously outlined in order to yield a test dataset for the classification algorithm. The images were then compared with emphasis on ice-edge detection, cloud discernment, and performance over time.

At +1 hour, both classification schemas perform similarly with regard to ice edge determination. The single image schema is more sensitive to clouds in the scene, while the 3-image series is less sensitive. This is principally a function of the movement of clouds in a 45 minute time series. With high cirrus clouds moving upwards of 100mph and lower cumulus clouds moving between 30-40mph, the clouds will move significant distances during the 45minute capture window for the time-series images. This results in a decreased sensitivity to moving clouds, as the radiance values of pixels in the path of clouds will change significantly if underlying surface is imaged during the time-series window. (See Day 072 +1hour classified images).

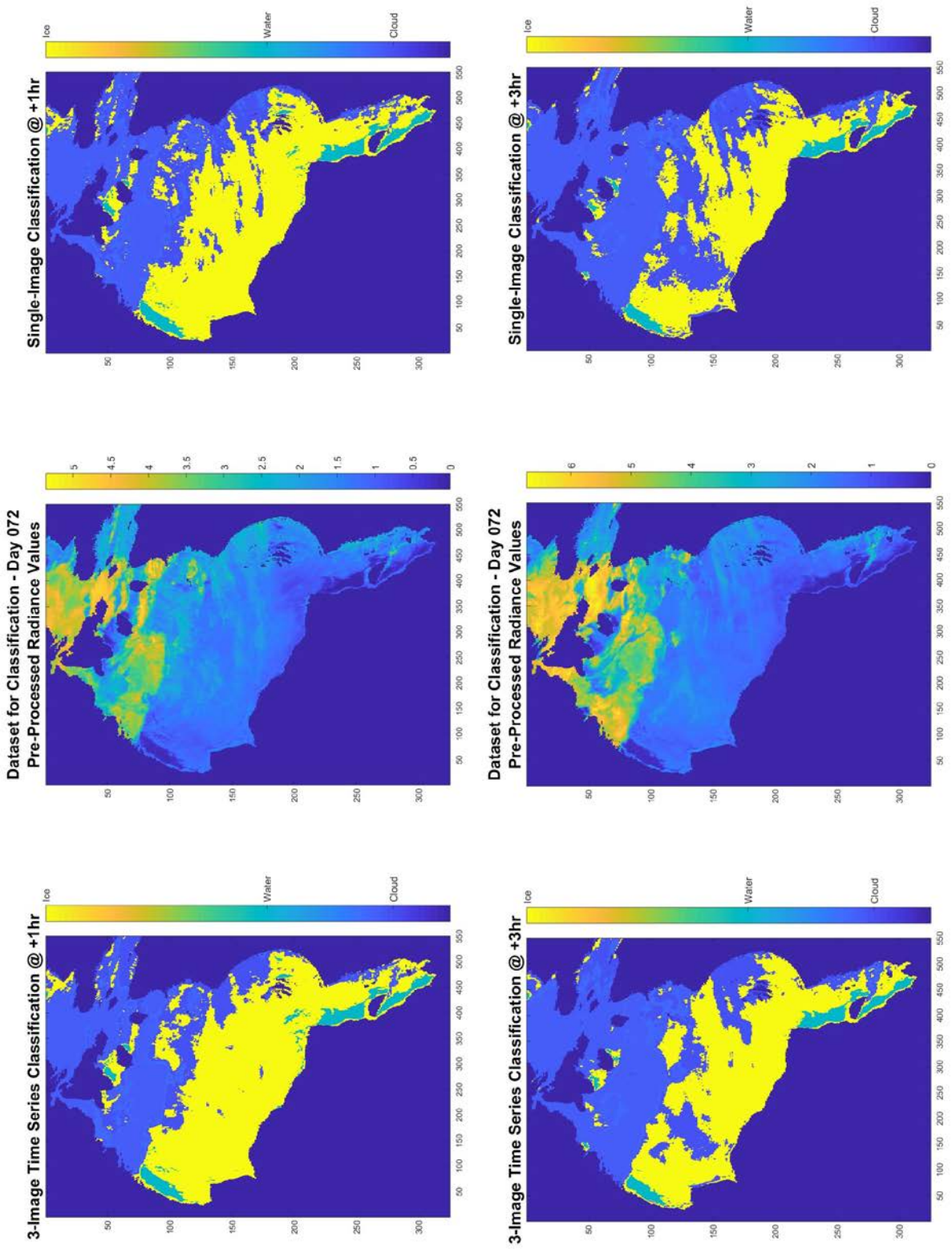

Figure 22: Day 072 classification examples. Left column is the 3-image time series, while the right column is the 1-image classification method. The center column shows the baseline images for classification.

The classification comparisons from April (days 116 and 117) show that both schemas deteriorate in their performance with an increase in time. Each of these tests show that at +1hour, the schemas perform well at discerning ice edge and clouds. These images show much more open water than is likely present as the time from classification schema development increases. While the structure of the ice likely changes throughout the course of the day, it is unlikely that it changes as much as is indicated in these classification results. The MODIS imagery from the day shows that there is likely thin ice in the Northwestern portion of Hudson Bay, and some leads/fractures are evident, but the imagery does not show the magnitude of change indicated by the classification results. This over-assessment of open water is likely the result of a significant change (≈ ±0.15 W/m^2)[5] in radiance value as more thin ice is exposed as a result of snow blowing from the ice, or a thinning of the ice over the course of the day. Both of these events would likely cause a change in the radiance value of the surface significant enough to change the classification category. The residual sun angle difference (that persists after sun angle correction attempts) is a significant factor in the difficulty in extended timeline classifications.

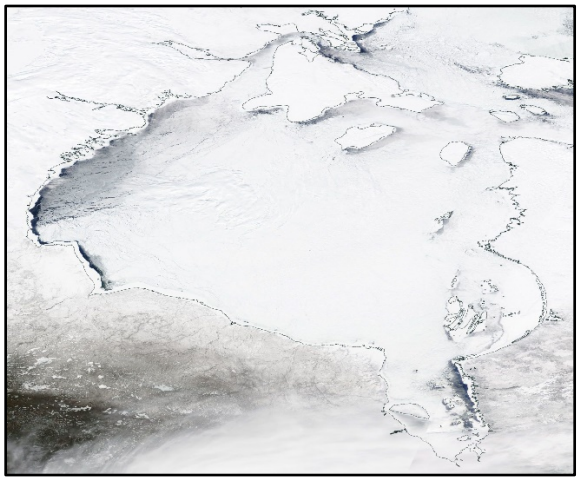

Figure 23: MODIS visible imagery from Day 116. Shown for comparison to the assessed ice-edge in the classified images.

[5] For example – in the dataset shown on the following page, pixel (118,102) has a value of 1.154 W/m^2 at D+1hr, but that value changes to 1.022W/m^2 at the D+3hr mark. This change of 0.13W/m^2 is sufficient to change classes in the classified image. This threshold is common between water/ice classification.

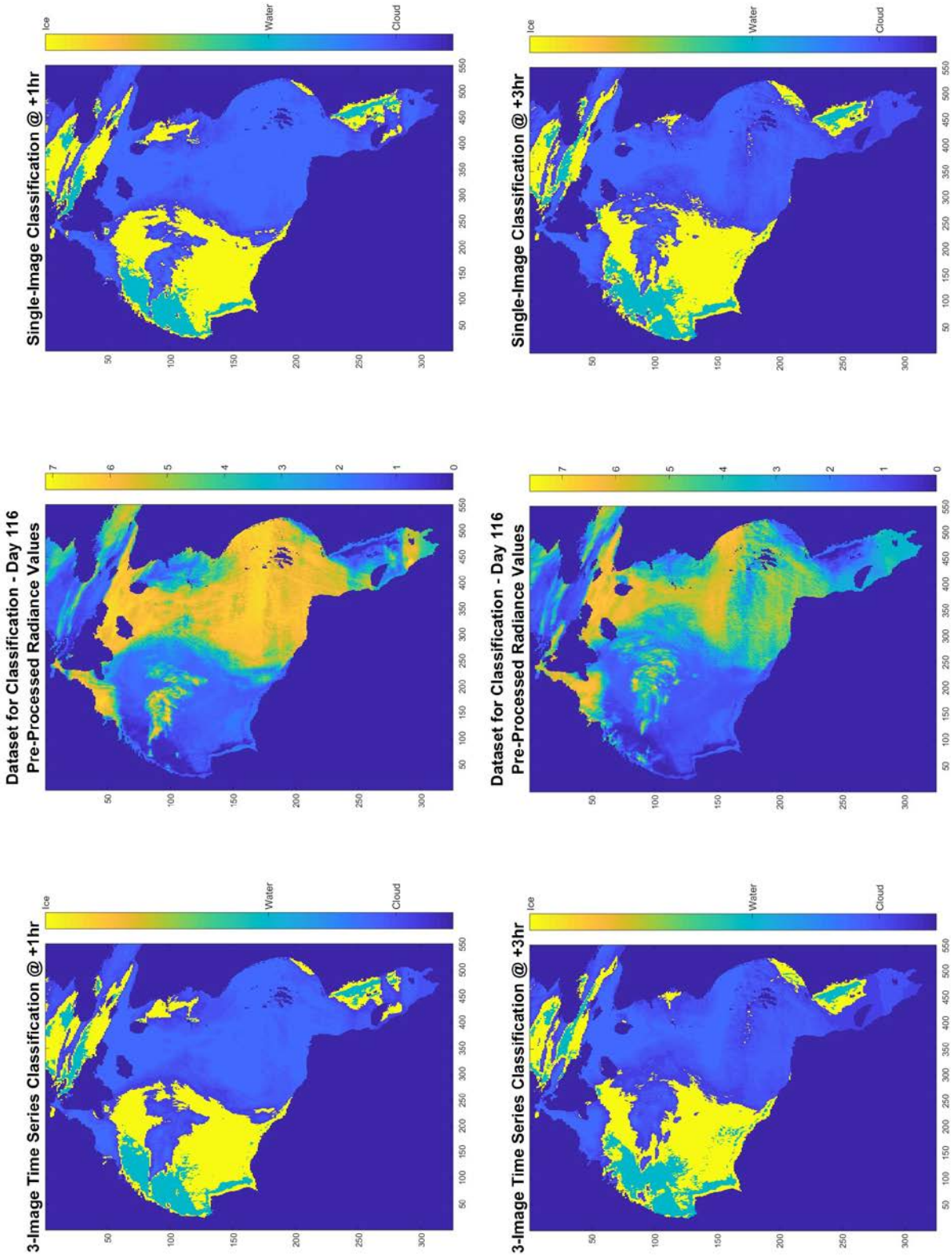

Figure 24: Day 116 classification schemas depicted. Sensitivity of the ice edge is evidenced by the rapid change over the time series in the classified images.

The most significant differences between the two classification techniques is in the sensitivity to clouds. Because there is no significant advantage in processing time between the two techniques, the 3-image time series technique is preferred because of this decreased cloud sensitivity within the scene. With the goal of the algorithm to ultimately classify the surface as water or ice, the minimizing of cloud-covering pixels is ideal as it results in more pixels classified as either ice or water. Both methods show signs of deterioration in their classifications as time increases. This is likely the result of the limitations of sun-angle correction, and as such, classification training should occur on an interval of 3 hours or less during daylight conditions.

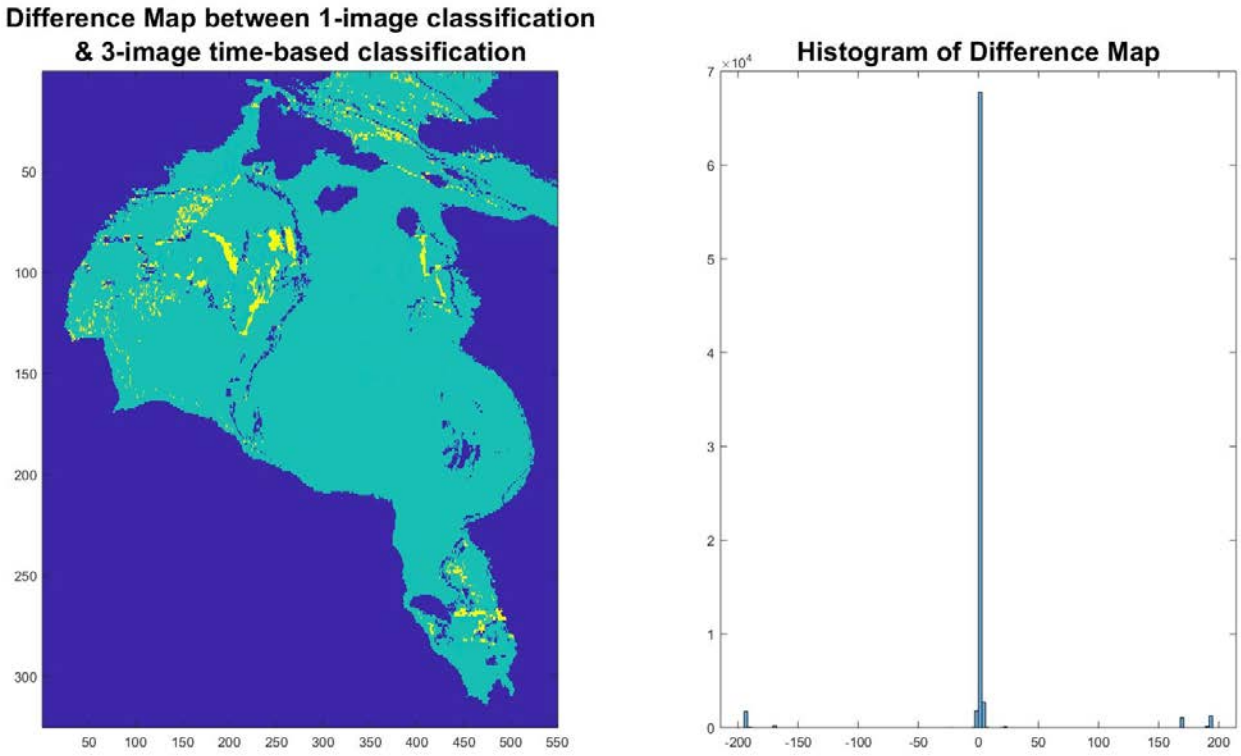

Figure 25: Difference map highlighting discrepancies between 3-image and 1-image classification schemas at +1hour (Day 116).

The above difference map shows the results of subtracting the 3-image time series classification image from the single-image classification image. This highlights the difference between the two models. The above histogram helps to explain this map. The values that hover around zero represent no-change, or

a very minor change in the classification level of the cloud cover in the image. The values between 150-200 are depicted in yellow on the map, and are areas where the 1-image schema classified the surface as either water or ice, but the 3-image schema classified the surface differently. The value of 170 is a pixel classified as ice in the 1-image schema and as water in the 3-image schema. Values around 185 are those classified as ice in the 1-image schema and as cloud in the 3-image schema. The negative values represent the 3-image schema classifying water or ice differently than the 1-image schema. The value of -185 is similarly a cloud in the 3-image schema, but ice in the 1-image schema, while the values of -170 represent ice in the 3-image schema, but cloud in the 1-image schema.

This depiction helps to identify the regions where the classification techniques disagree. Referring to the graphic above, the majority of disagreements occur at cloud edges. This highlights the difficulty in classifying cloud edges and cloud shadows which look much different than clouds or the underlying ice/water. It also highlights the sensitivity of the 1-image schema to clouds, and the more robust nature of the 3-image series. There are many more ice/cloud disagreements between 1-image and 3-image (histogram @ 170 vs. histogram @ -170) further demonstrating that the single image schema is much more sensitive to cloud presence in an image.

Multi-Day Schema Assessment:

While sun angle correction efforts may not account well enough for the sun's influence in order to classify an entire day's worth of images a classification from the same time period may be effective on D+1 or beyond. To test this theory, a 3-image time series classification schema was developed for Day 072 around noon local (1800GMT). This schema is then applied to D+1 (Day 073), D+2 (Day 074), and D+3 (Day 075) to assess if a "time of day" classification schema can be applied across a multi-day span with satisfactory results.

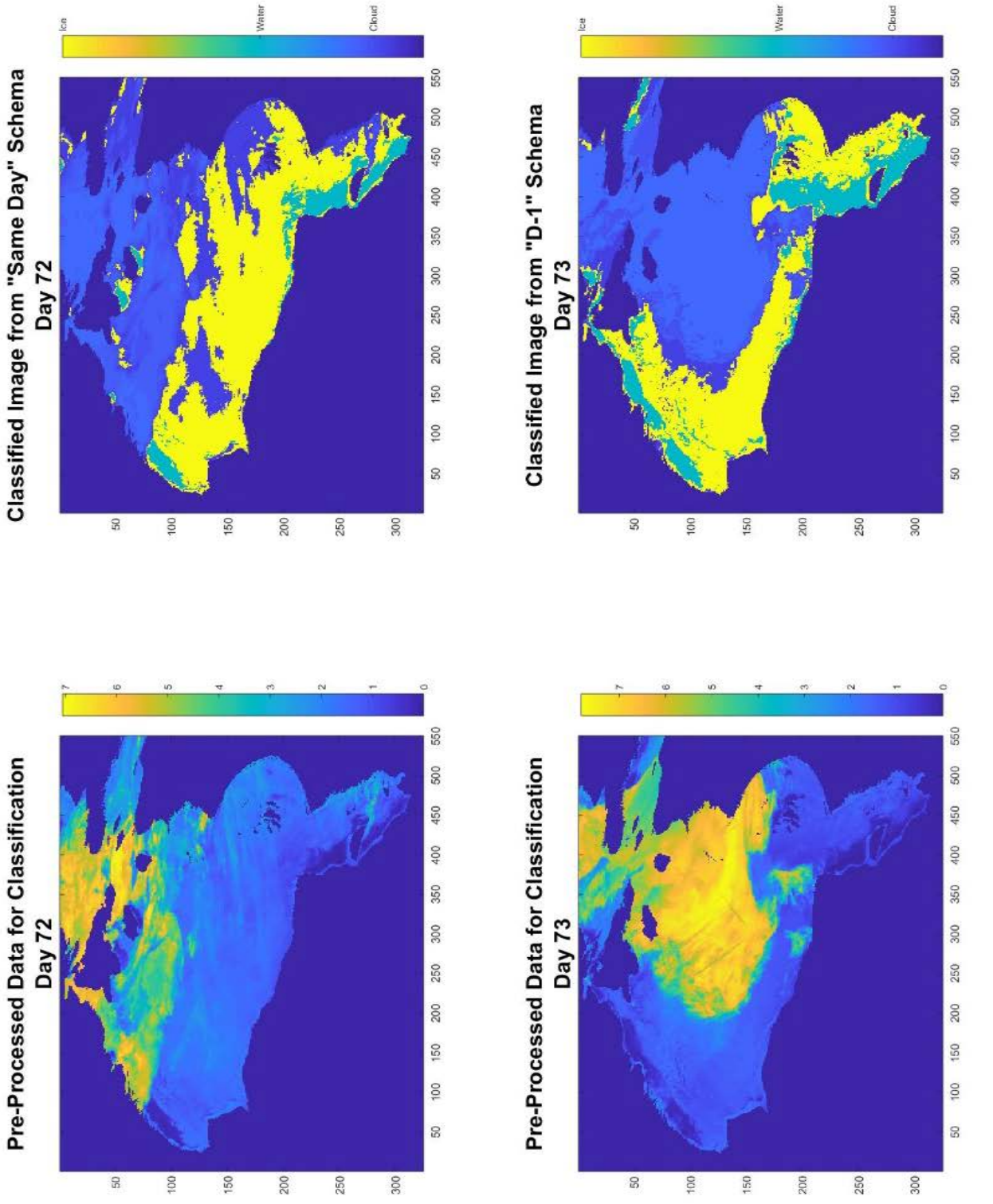

Figure 26: Classification results when schema from approximately noon on Day 072 is applied to Day 073 at noon. Deterioration in the ability to classify is evident as the time period is extended.

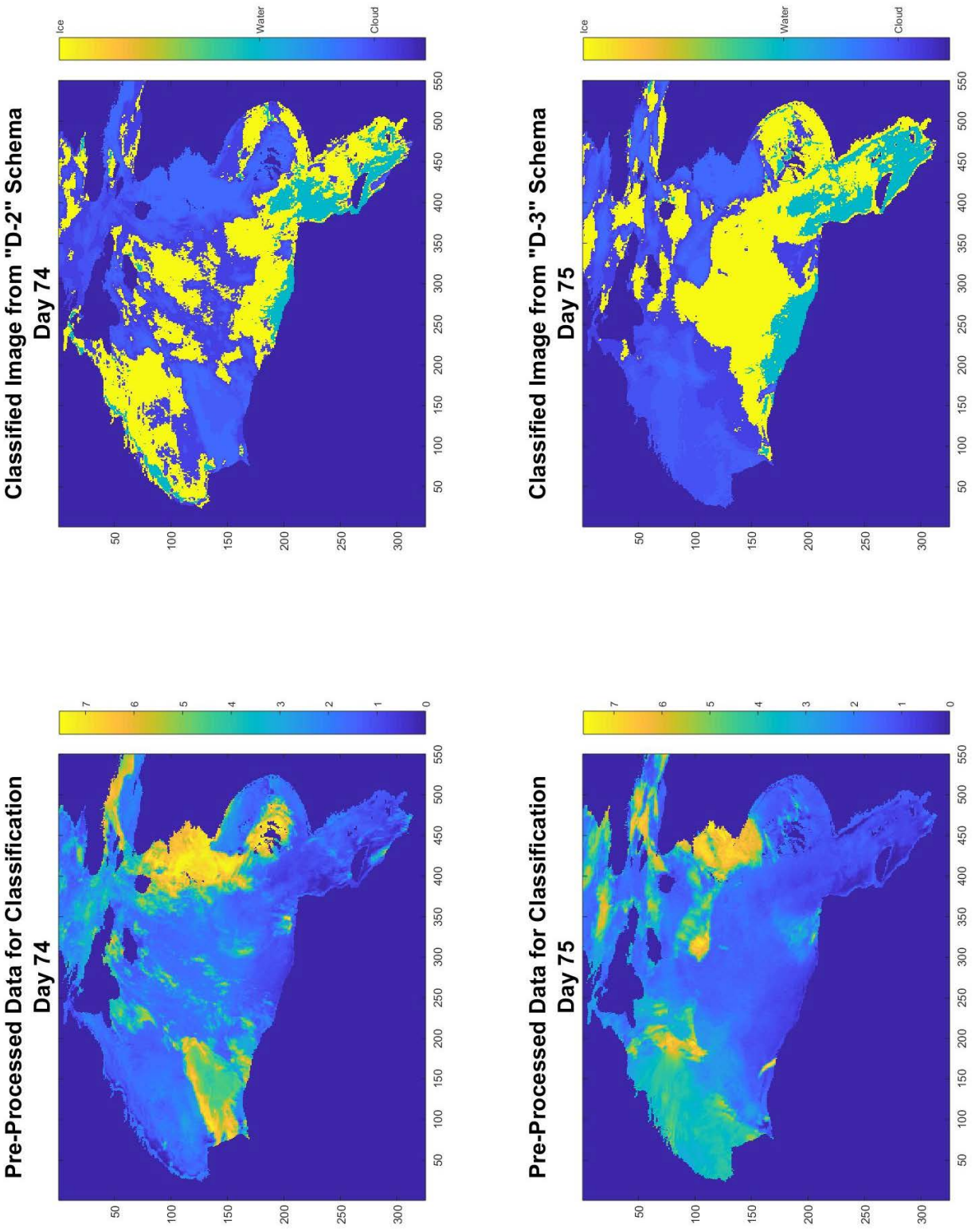

Figure 27: Classification results when schema from approximately noon on Day 072 is applied to Days 074 & Day 075 at noon. Deterioration in the ability to classify is evident as the time period is extended.

The schema developed on Day 072 (D-day) is shown above. It used a 3-image series (local times: 1130, 1145, 1200 [1730, 1745, 1800 GMT]) during the middle of the daylight period. Despite efforts to normalize the data through time using dark object subtraction and sun angle correction, the same point (and with similar surface type) can range in radiance value by more than .09W/m^2 and over a three day period the sun angle at the same location can change by more than .73°. While these are contributing factors to the difficulty using the same schema to classify images spanning multiple days, the biggest factor is the precision used for the 3-image series classification. The algorithm uses a decision tree with approximately 50 different decision points in order to develop six distinct classes. The sensitivity at which these classes are distinguished is likely greater than the sensitivity between subsequent days resulting from the change in sun angle and reported radiance.

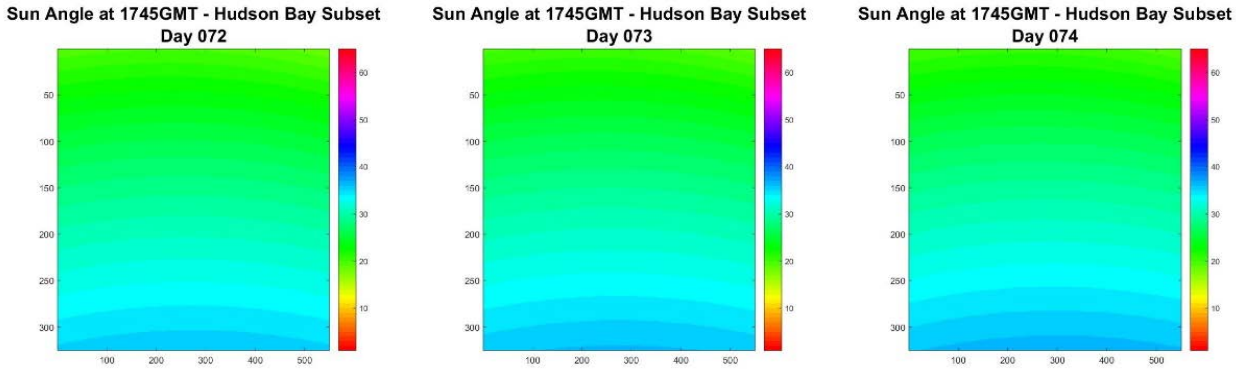

Figure 28: Sun Angle changes over a 3-day period (Day 72-Day 74). Scenes show sun angle at 1145 local time (1745GMT).

A single image classification decision tree can also be applied across multiple days. The results show that this method performs similarly in its ability to classify across multiple days. While the changes in sun angle remain a constant for this type of classification, the single image decision tree only has 5 decision points. While this eliminates the precision and decision points factor that may confound the multi-day classification for a 3-image time series, the results for the single-image schema classification appear quite similar. The inability of a classification scheme derived from either a single image or a 3-image time series

on subsequent days within a short time period indicates it is unlikely to be effective on an extended time scale like weeks or months.

While a single classification schema is effective for a time series data cube, these schema are sensitive to changes in the data. Specifically they are not interchangeable between days in which atmospheric conditions (cloud cover percentage, ice cover percentage, water percentage) are dramatically different, or when sun conditions have substantially changed (as they would over the course of weeks/months). The corrective pre-processing measures described above, do not create similar enough reflectance values that a classification schema from mid-March would be effective in mid-June (or even mid-April).

Contrast Enhancements:

Another technique to better classify the data is to apply an artificial enhancement. This method seeks to separate the distinct clusters on the histogram of a scene in order to aid in the classification process. It does so by increasing the difference between the values that represent water and those that represent ice and clouds. In the process of "spreading" the histogram, measurement units are lost however, and the histogram becomes a chart of digital numbers rather than W/m^2.

The process of enhancing the data set in this way begins with performing a histogram equalization across the daily data set. Histogram equalization is a technique that analyzes the histogram of a set scene, calculates the probability that a pixel value will fall into a specific bin, and then multiplies the pixel value by that probability (Jensen, 2015). The resulting histogram is one where the data is spread across the histogram of possible pixels values according to its likelihood of occurrence. This process is accomplished using a transformation curve like the one shown below.

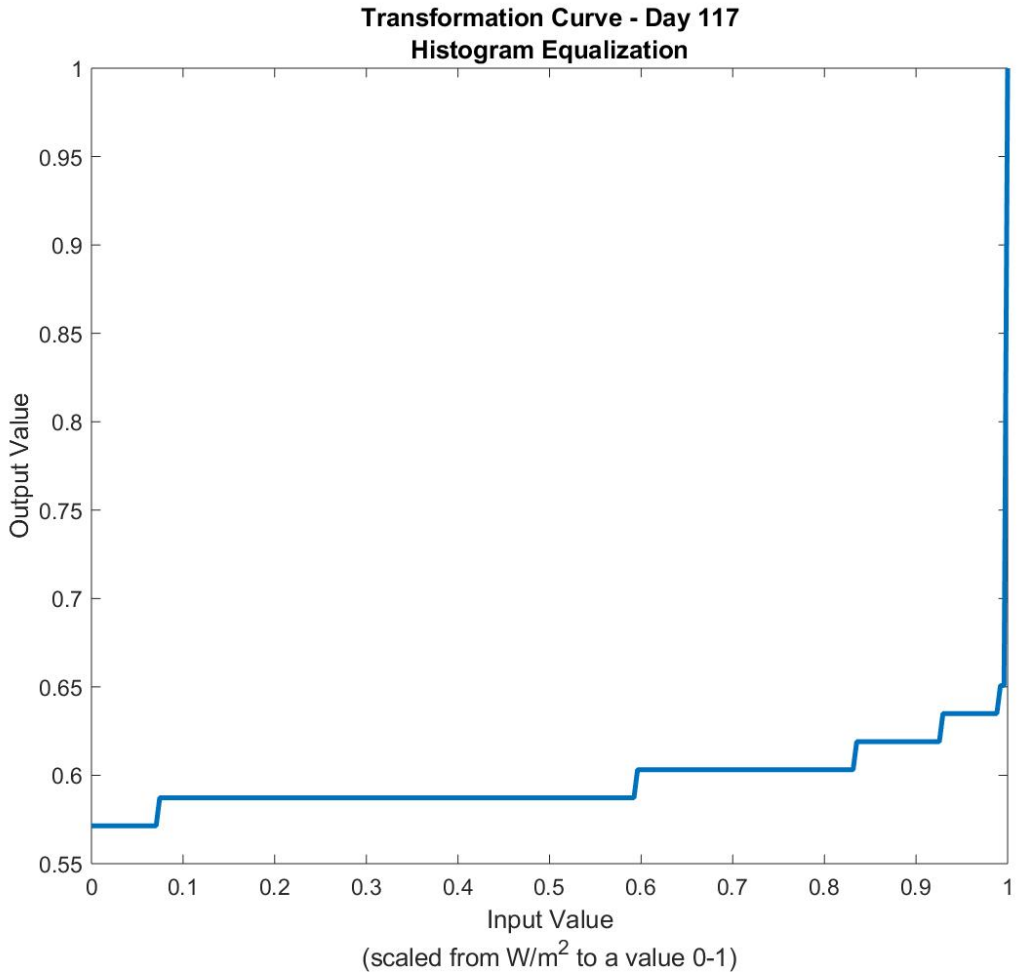

Figure 29: Transformation curve for histogram equalization on Day 117. Values on the Y-axis replace values on the X-axis once the histogram equalization is complete.

In this dataset, the result of a histogram equalization is that pixels are consolidated toward the low end of values (representing water) or the high end of values (clouds). While this step is limiting in the amount of information that can be drawn from the data, it can serve as an intermediate step to further enhance the data produced following the pre-processing steps. When the histogram equalization is multiplied by the pre-processed dataset, the cloud and ice values remain fairly consistent (because they are multiplied by values very close to 1) but values that represent water are driven to be lower, further separating them on the histogram (because they are multiplied by values between .5 and .7). This step enhances the difference in values that represent ice and water by providing a more clear break between the representative values.

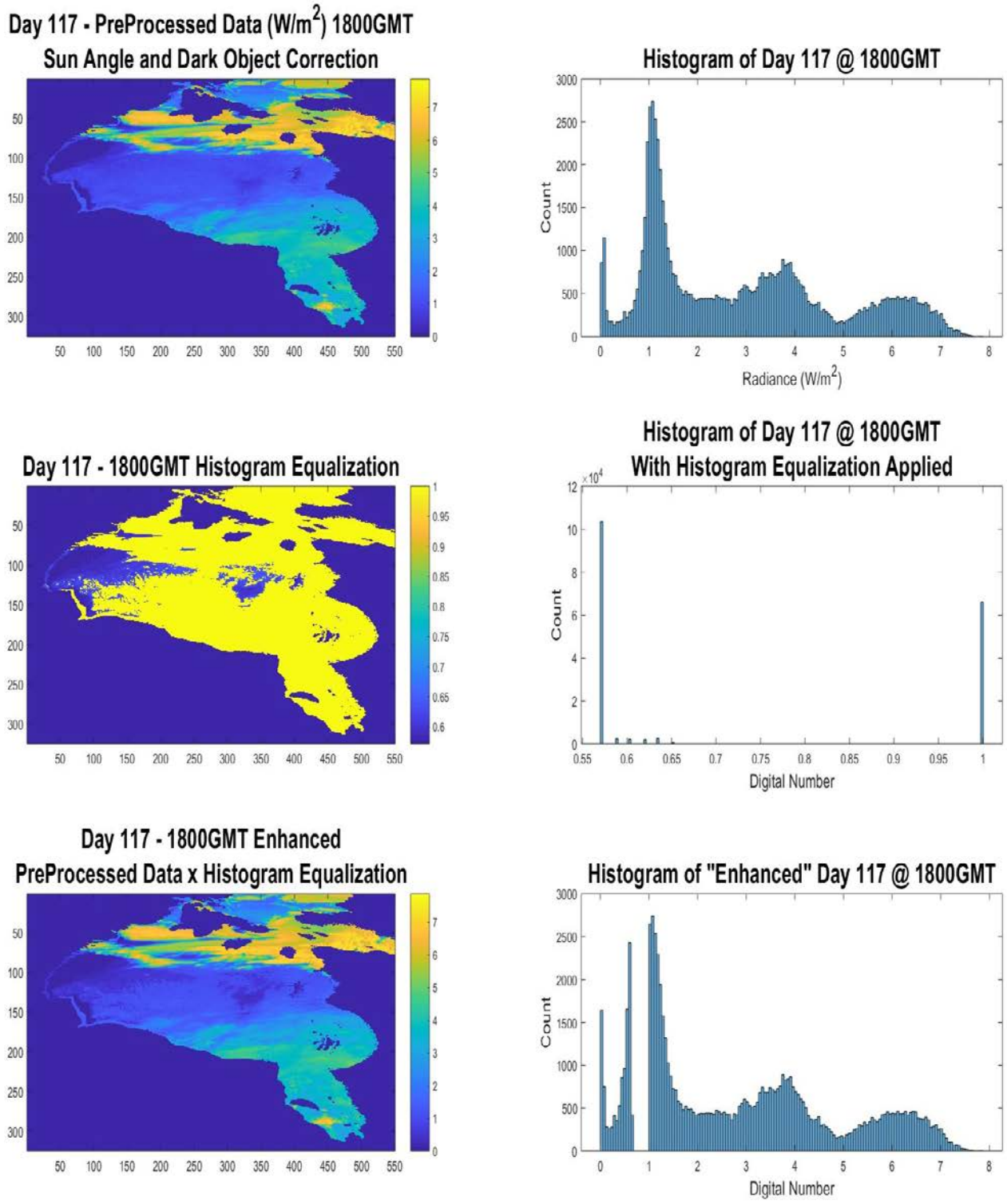

Figure 30: Process for enhancing the preprocessed data to increase contrast between water, ice and clouds using histogram equalization. (Print versions of this graphic may not show a significant distinction between the top-left image and bottom-left image – ice in the bottom left image is much less uniform following the data enhancement showing that there is a distinction in ice-cover)

This step to enhance the data creates a new set of conditions to test through the classification algorithm for both the single image technique as well as the 3-image time series technique. The results of these tests is shown below.

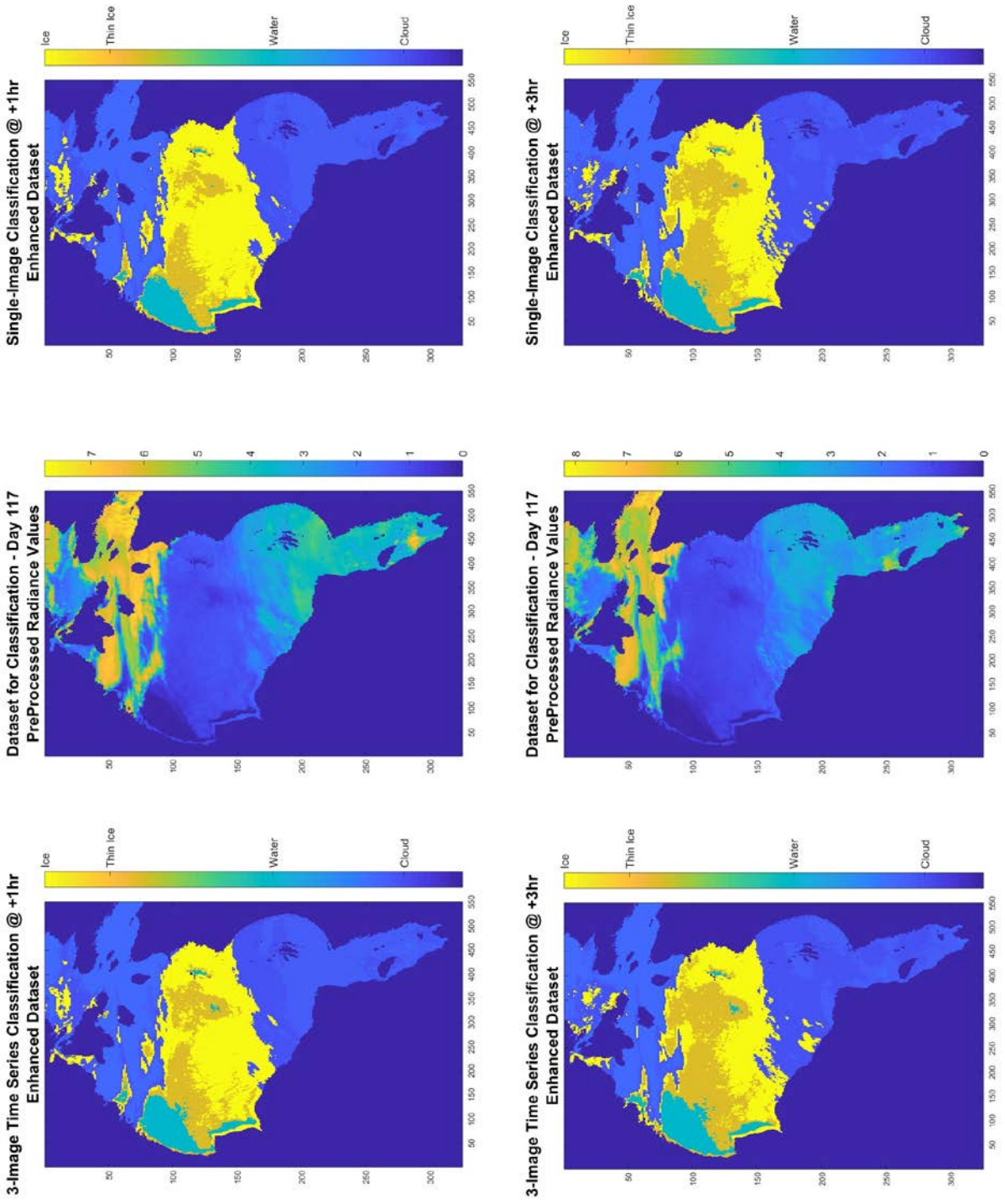

Figure 31: Day 117 Enhanced Data used in 3-image and single image classification algorithms.

When this data is compared to MODIS data from Day 117 it is apparent that there is different structure within the ice. This feature is more easily discernable in the enhanced data classifications than in the pre-processed data classifications as a result of the amplification of water and ice features through histogram equalization. The MODIS data is shown below.

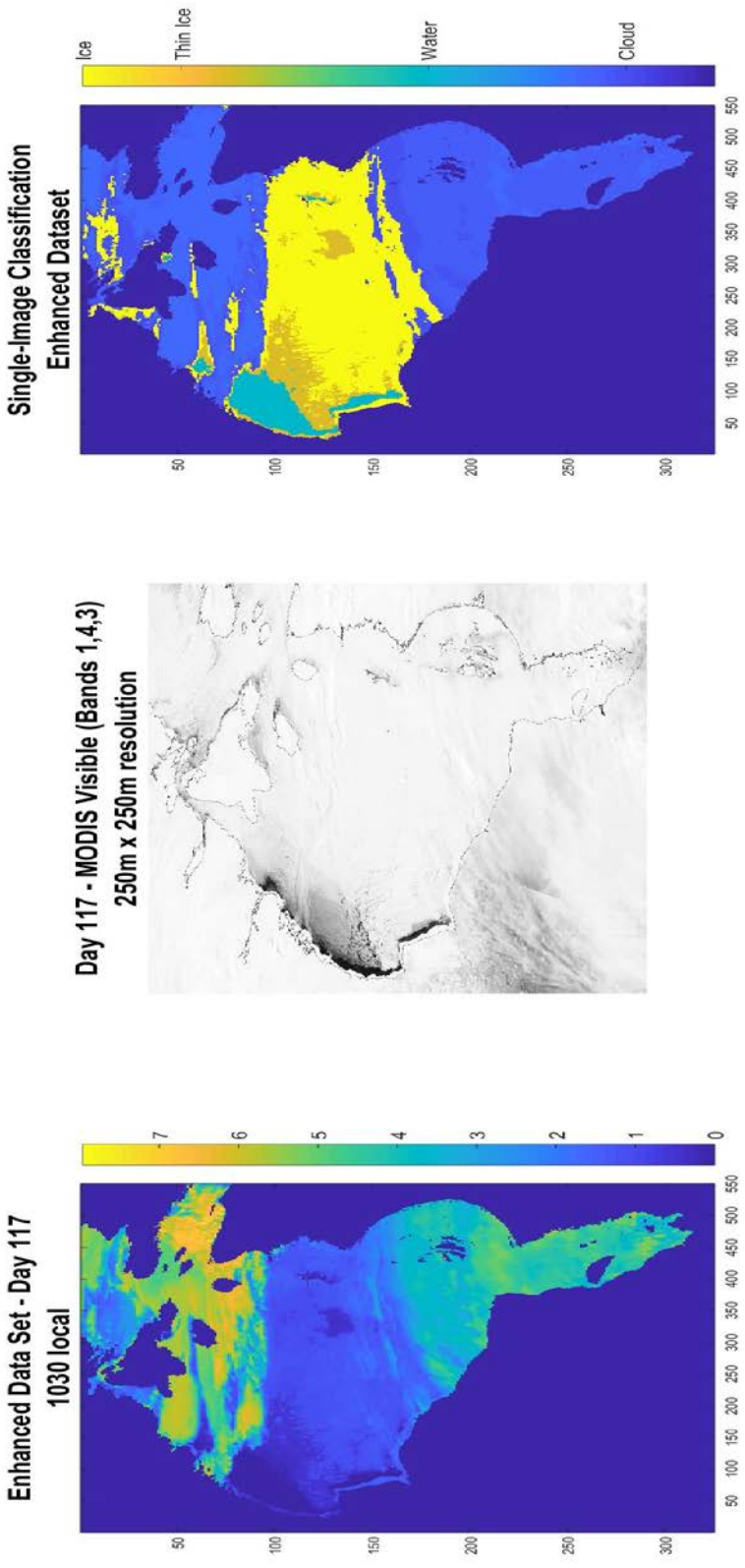

Figure 32: Comparison of the preprocessed SWIR Product, a 250m resolution MODIS product, and the outcome of the classification algorithm using enhanced data.

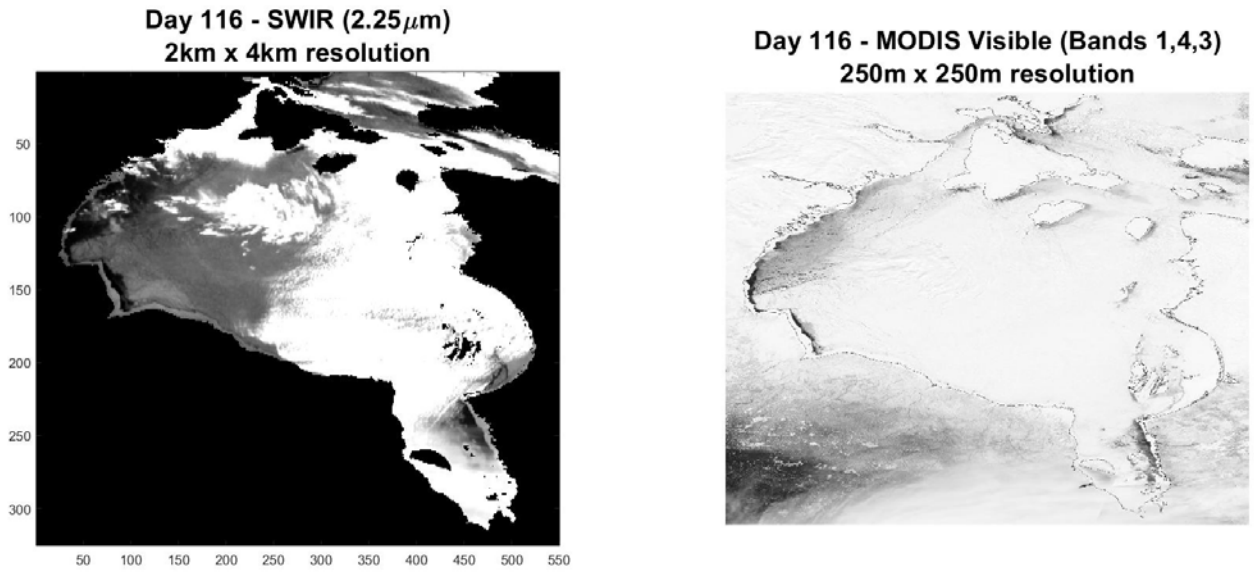

Figure 33: A comparison of Day116 from SWIR vs. Day116 from MODIS visible imagery (Bands 1,4,3).

Other Techniques:

While k-means clustering for data classification is a simple and efficient method for data segregation, there are likely better techniques for classifying the data once pre-processed. In brief experimentation, Gaussian mixture models seem like there is some promise in providing a reliable classification schema that may be able to persist throughout or potentially beyond a 3-hour timeline. Gaussian mixture models assume that an underlying dataset is a combination of multiple Gaussian distributions together, rather than assuming that the overall distribution of a dataset is normal. This technique is also able to assess the underlying data identify how many classes (or separate Gaussian distributions) the data ought to be separated into based on minimizing the Akaike information criterion (AIC). By minimizing this value, the quality of the model is assessed and the model (regardless of the number of "k" classes) with the lowest AIC is selected as that which best models the data.

The below examples show Day 116 data prior to Gaussian mixture modeling (blue histogram) and the Gaussian distributions determined to be a composite of the overall dataset. As is evident from the lack

of discreteness amongst classes, the classification product is unclear, as the Gaussian classification causes many of the classes to blur together.

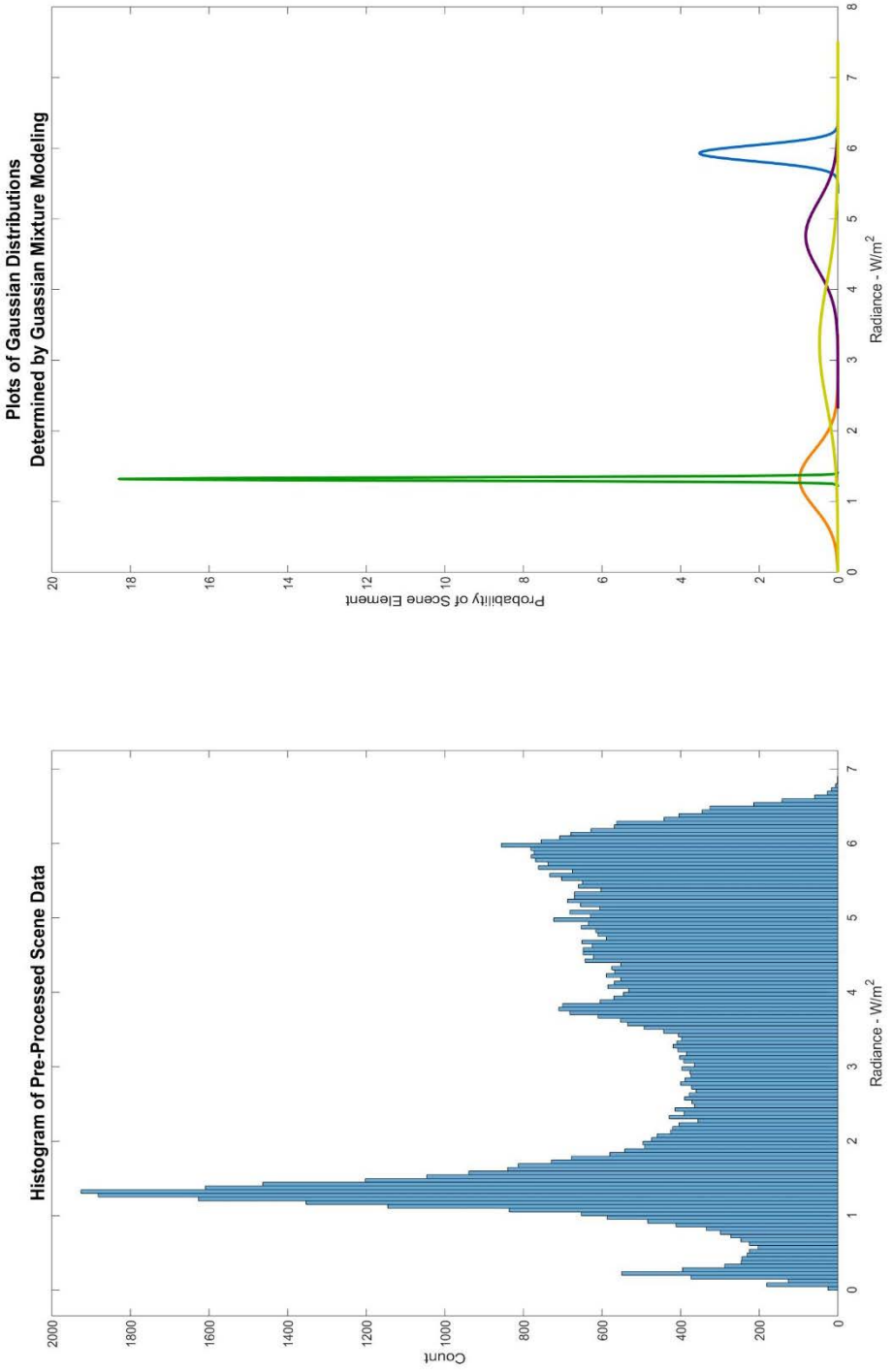

Figure 34: Histogram of Day 116 (0945Local time) and the Gaussian mixture model classification curves associated with the dataset.

While the data visually appears to be a combination of Gaussian distributions, none of the classes presents as normal a distribution as would be desired for a quality model. This is particularly true in the discernment between ice and water when clouds are present in the scene. While this technique is imperfect, if it is used as an intermediary to filter clouds, it can yield a better product.

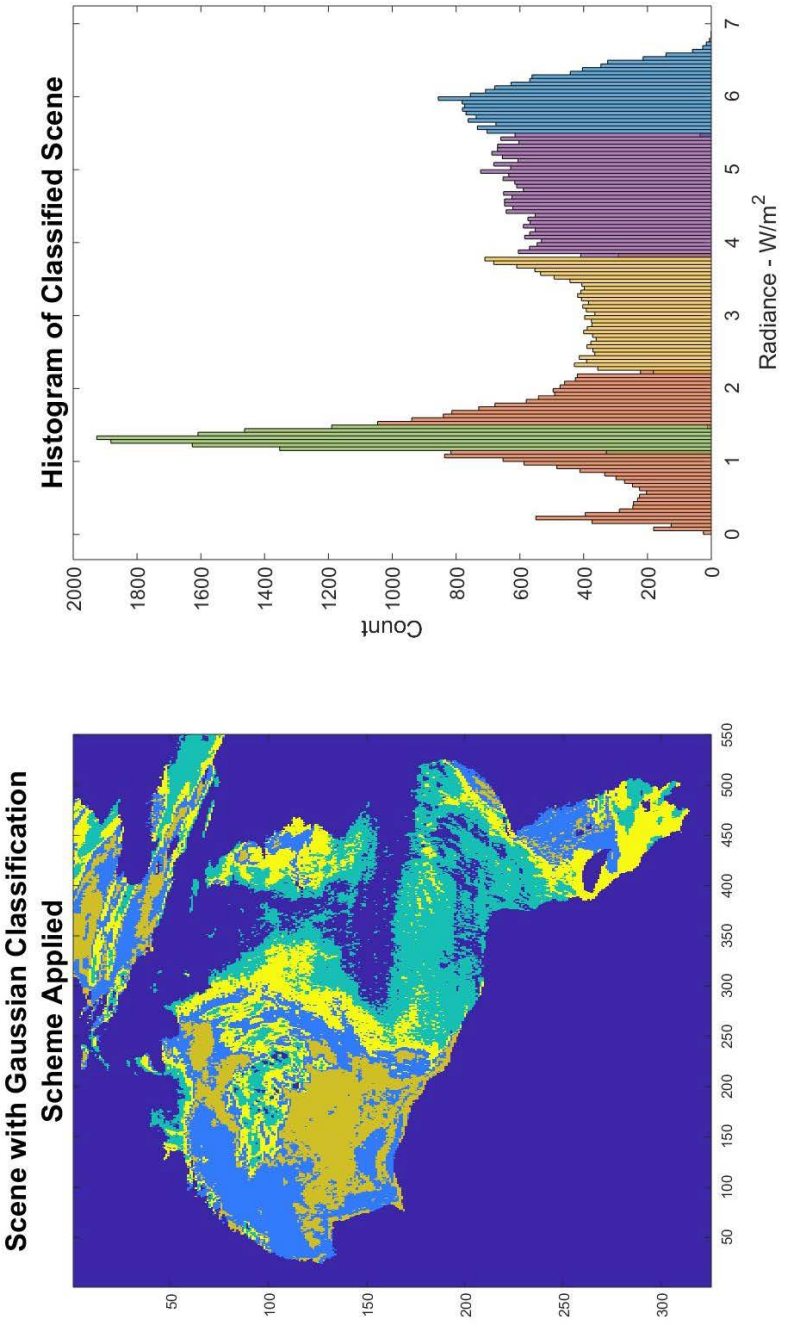

Figure 35: Classification from the Gaussian mixture model, and the histogram as divided by classes. Ice and water are not discrete as evidenced in the image as well as the histogram (orange/ green in the histogram and blue/mustard in the image).

If the yellow, purple and blue classes (from the figure 35 - histogram) are removed from the dataset, another Gaussian mixture model can then be developed. This one would then be built from data that is only representative of ice and water (or some combination of those two elements with thin clouds). This process will still require a man-in-the-loop to remove specific classes that correspond to clouds, and will need enhancements to upscale for application on time-series datasets but the initial tests were promising.

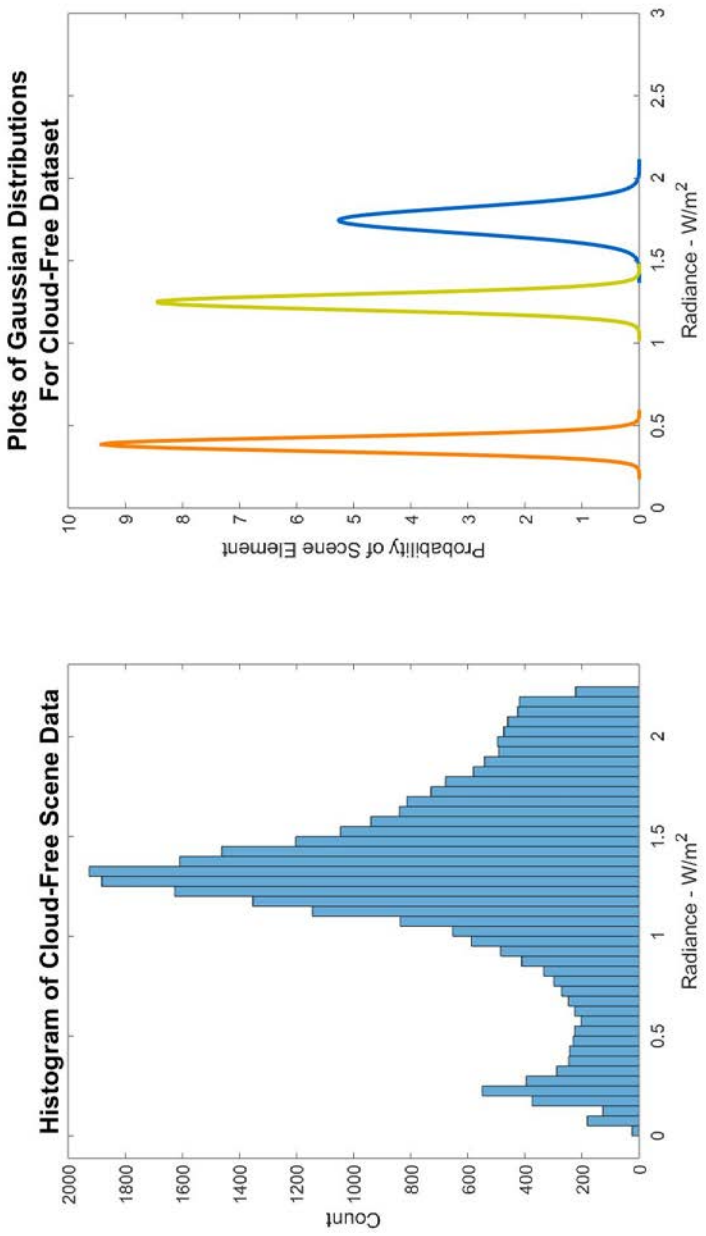

Figure 36: Histogram and Gaussian distribution curves of a cloud-free dataset developed from a previous Gaussian mixture model.

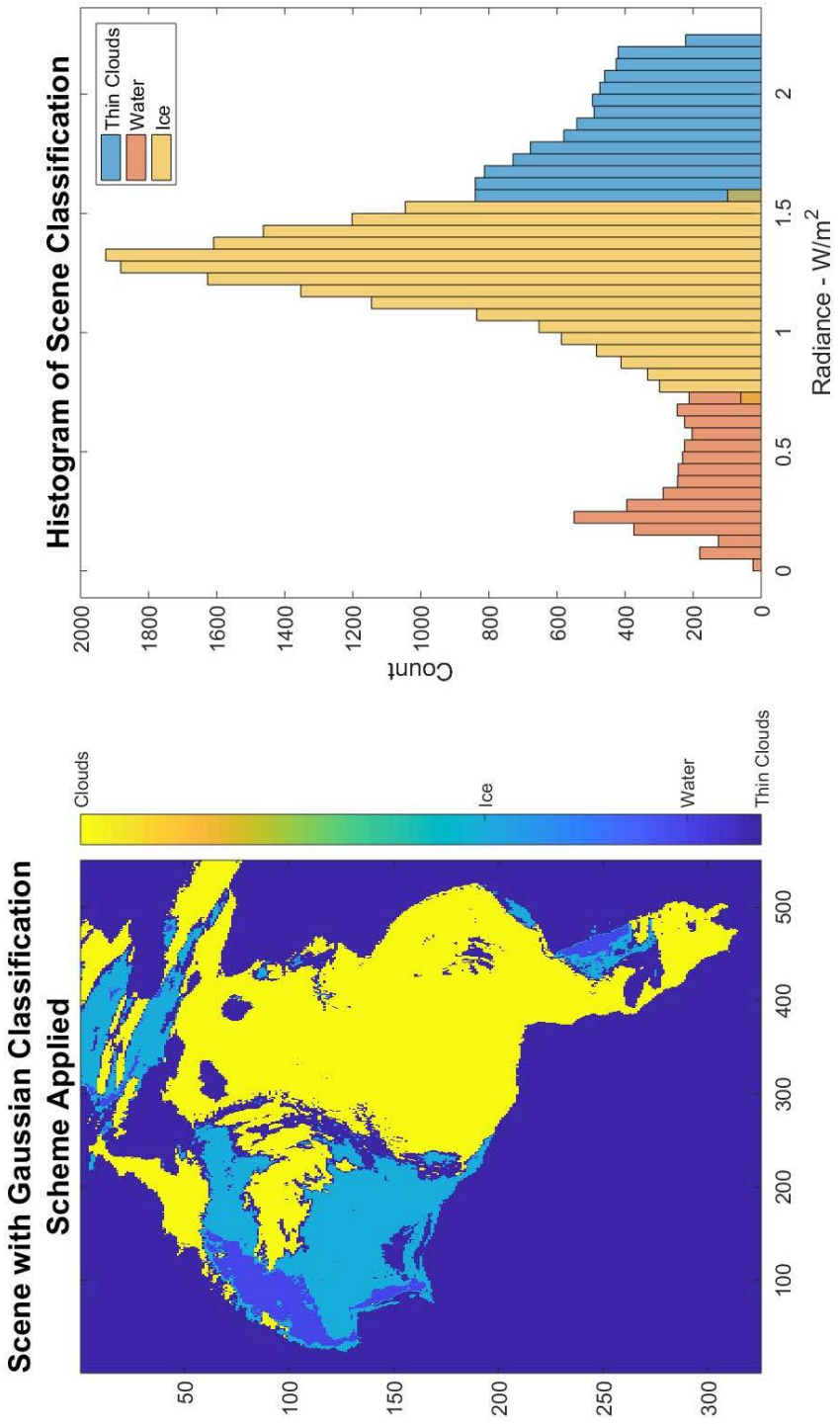

Figure 37: Classified image and histogram distribution from cloud free dataset. The results are promising, but will require enhancements to streamline the transition between initial Gaussian mixture model and the cloud-free Gaussian mixture model.

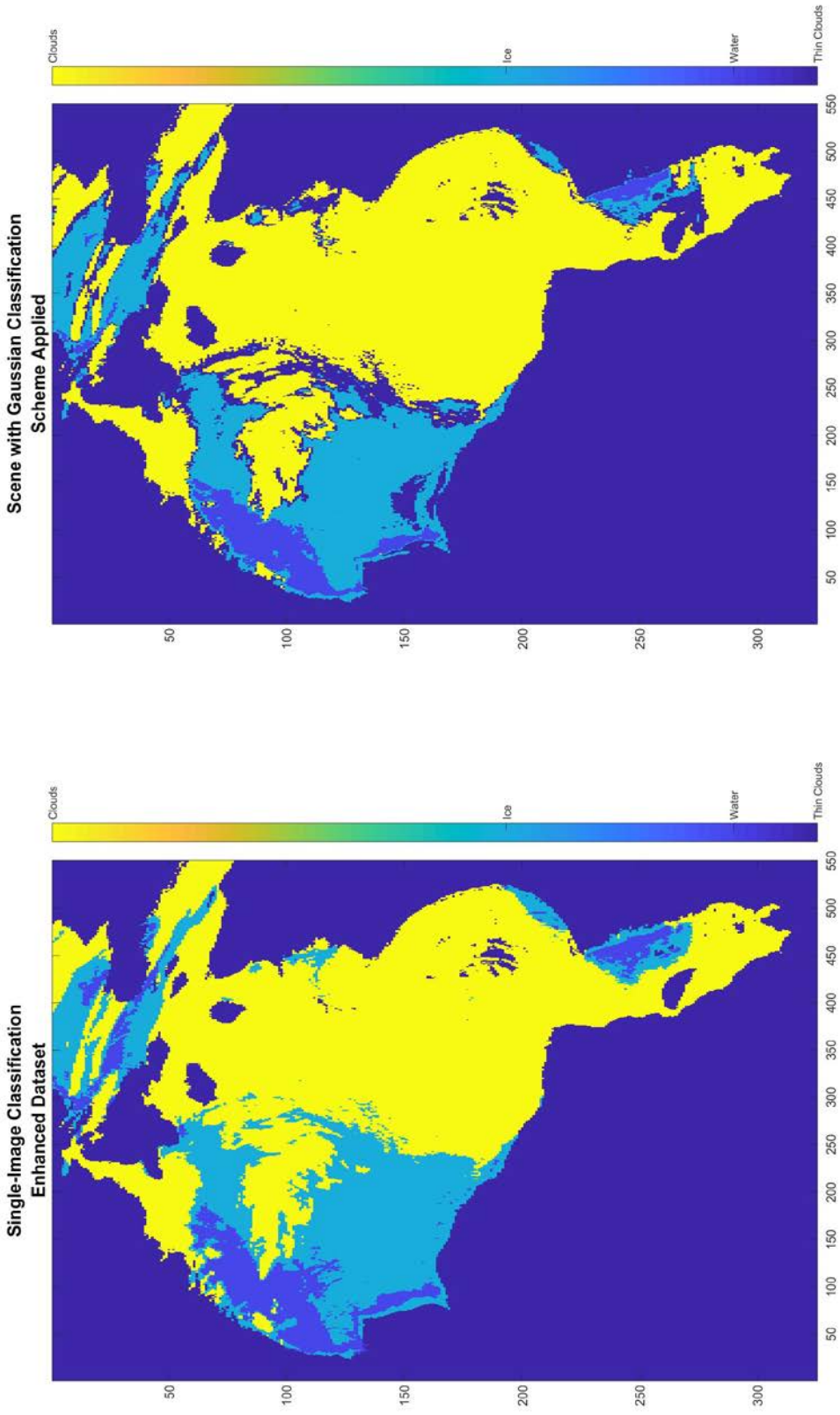

Figure 38: Comparison of Day 116 enhanced data set single-image classification scheme result, and cloud-filtered Gaussian Mixture Model classification. (of note, the enhanced data set classification is based on a 3hr old schema, whereas the Gaussian mixture model schema is applied within the hour.

Discussion:

As the results demonstrate, there is a clear ability to use single-channel short-wave infrared to detect and distinguish sea ice in remotely sensed imagery. This demonstration is significant in that it is unlike any other sea ice product currently available because of the spectral characteristics of the underlying data. While the products generated may not replace current products, the amount of information that is derived from a single file is noteworthy, and the temporal resolution of the underlying dataset makes these techniques and capabilities much more interesting.

Short wave infrared channels on remote sensing platforms are typically used to identify cloud properties, assess vegetative health, and assess snow cover (Harris Corporation, 2017a). While there is utility in assessing snow cover using short-wave infrared, it stems from the fact that snow is such a poor reflector of SWIR. This thinking is counter to the techniques and methods applied above, in which the ability of snow (on sea ice) to reflect SWIR energy is the entire basis of the research. While both water and snow are poor SWIR reflectors, the strength of snow albedo in the short-wave portion of the EM spectrum when compared to sea water albedo in the same EM region makes this classification possible.

An initial assessment of the full disk image for Band 6 (Short-Wave infrared at approximately 2.25µm) should deter use for sea ice research given that the only identifiable features in these images are cloud, and land. Further, the histogram of the full disk scene compared to the subset area of interest shows that at a cursory level, information regarding sea ice is likely lost in the noise. Upon closer scrutiny however, and with intensive efforts, a signal is derived from the noise.

While the SWIR images are produced at 10 bit (meaning there are 1024 shades of gray available for interpretation), the full disk image only uses 400 of 1024 shades (approximately 39%). In the Hudson Bay subset, only 267 shades of gray are used, meaning that the data of interest is contained in approximately

26% of the available spectrum of data possibilities. This severely limited condition makes deriving information regarding sea ice cover a difficult problem, but one that is not insurmountable.

Other techniques to characterize or detect sea ice use multiple channels of data in concert to inform product development. In the case of passive microwave remote sensing of sea ice, in addition to different channels being used, different polarities of the same channel are also used. This technique effectively doubles the data available for the classification algorithm. Conversely in this product, a single-channel is used which requires that the data be massaged and manipulated in a way that it provides enough information to develop a product while still remaining recognizable and meaningful when it stands on its own.

Most remarkable throughout this process is the ability to discern structure within the ice cover in the SWIR dataset. This structure is evident in the MODIS 250m visible imagery, but is also present in the GOES-16 SWIR at a resolution of approximately 2km x 4.6km. Preserving and highlighting this structure in the ice supports the viability of a single channel ice characterization and detection product from SWIR imagery. This detail is precisely the information that is important in understanding sea ice cover and using a product for transportation applications.

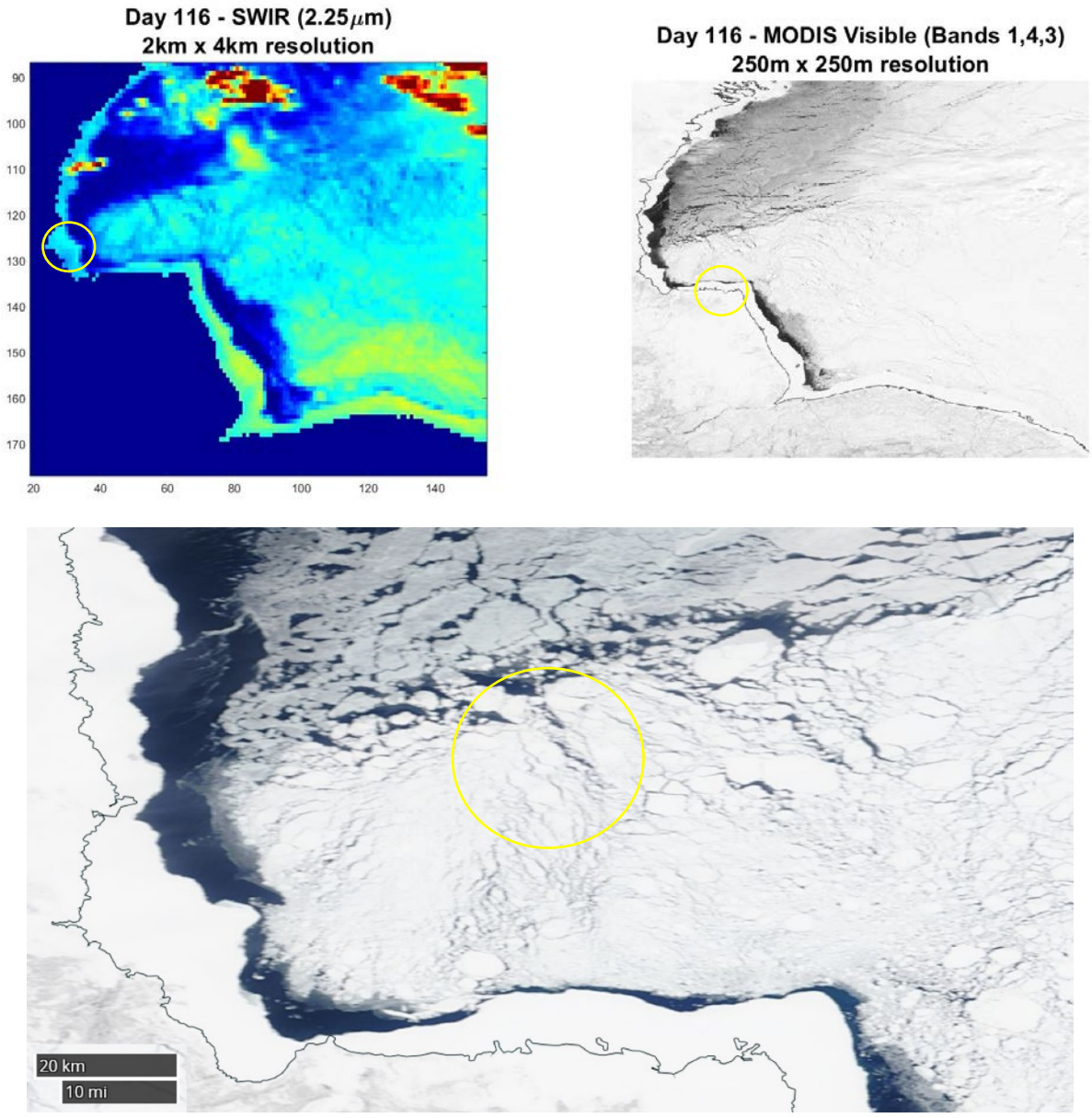

(*EOSDIS - NASA Worldview*, 2018)

Figure 39: Zoomed view shows structure of the ice that is evident in MODIS (250m resolution) and is also present in GOES-16 Band 6 @ 2x4.5km resolution).

The yellow circles in the images above highlights one such structure in the ice. Despite the surface feature being at a sub-pixel resolution in the GOES-16 dataset, its appearance demonstrates that there is an ability to discern these features in SWIR imagery. The structure and breaks in ice cover occur at scales less than 2km but the difference in surface albedo is significant enough in the preprocessed and enhanced

data sets to be the dominant feature in a pixel. That means that the pixels display this feature despite it occurring at that sub-pixel resolution scale.

There is merit to both of the techniques discussed above (using pre-processed data and using enhanced data), but they perhaps serve different purposes and utilities. The enhanced data set seems to provide the best characterization of sea ice cover, particularly when applied using a single image as the basis for the classification algorithm. This process moves the underlying data away from a recognizable measurement (W/m^2) however, thus requiring additional steps to map the data back to radiance values. If the end state of this process is the classification map itself, then this product seems to yield the most reliable and accurate results, specifically when the classification algorithm is derived from data that is not older than one hour. This means that a classification algorithm can be produced every hour and applied for the next four images to be received with reliable results. The processing requirements for this type of data production is minimal and can likely be accomplished in less than one minute from receipt of the raw full-disk image of SWIR data.

This type of data production does little to minimize the effect of clouds on the classified scene, but creates a usable product for cloud-free regions that is reliable, quick, and constructed using simple remote sensing principles. These methods rely upon the quality of the data available, while applying a simple yet effective process for detecting sea ice within a scene. The simple methodology is critical to ensuring a quick processing timetable to capitalize on the temporal resolution of the sensor.

The 3-image time series approach for classification retains the units of measure for radiance while being less susceptible to cloud interference. The time series method reduces the influence of fast-moving clouds in scenes by sampling from a longer time series. This limits the cloud albedo influence on a single pixel later used for classification training. This method, more robust in its approach, is more appropriate for studies less reliant on the high-temporal aspect of the produced data. The time series can be increased

or decreased as necessary (scaled by using more subsequent images in a time-series), and while the complexity of the underlying decision tree will increase, processing time will not change significantly.

Utility:

This research into understanding the capabilities and limitations of short wave infrared remote sensing applications is some of the foundational research for an ongoing research collaboration between the National Snow and Ice Data Center and the US Air Force Space and Missile Systems Center. NSIDC responded to a broad agency announcement published by the US Air Force which sought investments into innovative concepts, capability developments, and applied research, using data from the SBIRS payloads. Because of the persistent nature of these satellites, and the polar geometry of the HEO satellites, NSIDC submitted a proposal to assess the applicability of this data to near-real-time monitoring of sea ice conditions of Arctic sea ice. This type of temporal scale product has applications for civil, military, and commercial ventures as well as scientific applications for both military and civil agencies.

The Air Force ultimately funded the project under the name ICARTA – Ice Characterization of the Arctic for Transportation Applications and tasked to accomplish the following:

1. Develop and deliver prototype ICARTA algorithms to demonstrate that OPIR can monitor sea ice conditions.
2. Test these algorithms within the OPIR framework.
3. Identify and document requirements to move prototype to operational product.
4. Incorporate prototype algorithms into lab environment to demonstrate production capabilities.

NSIDC assumed a partnership with Net-centric Design Professionals (NDP) to complete the work with the understanding that algorithm development was the responsibility of NSIDC while implementation and upscaling the purview of NDP.

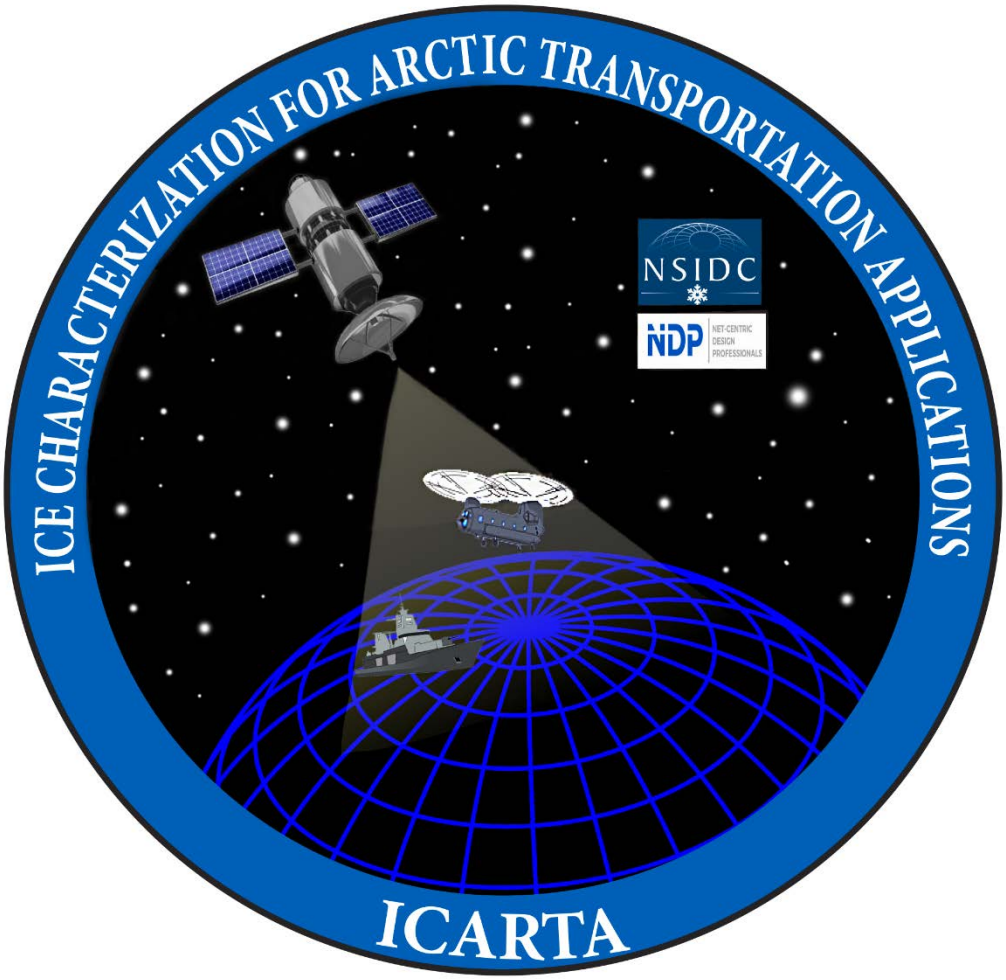

Figure 40: Logo for ICARTA project.

The research conducted using GOES-16 SWIR bands ice characterization and detection served two functions with regard to the ICARTA project. It first assessed whether single-channel shortwave infrared remote sensing was a feasible platform for sea ice detection at a degraded spatial scale but impressive temporal scale. Secondly, it served to provide unclassified data for research and collaboration to develop and refine algorithms to eventually apply toward SBIRS payload data. The foundational research using GOES-16 applied to contract requirement one (stated above). It used Hudson Bay sea ice rather than Arctic sea ice because of the limitations of the satellite, but this distinction in location is insignificant for research implications.

Use of GOES-16 established a proven ability to distinguish sea ice, clouds, and water in the GOES-16 SWIR spectrum and allowed for the development of processes to make detection and discernment more reliable. These processes include the preprocessing requirements to allow short-scale time series images to cooperate with one another in classification algorithms. These steps included atmospheric corrections and sun angle corrections. While sun angle corrections are applied for most satellite platforms, these are often done to correct for time of year, not time of day. Because polar orbiting satellites image the same portions of the earth at similar times each day, the corrections applied are to adjust for large-scale sun angle changes that may occur over the course of 16 days or fewer. This project required correction of sun angle due to the persistent coverage of the GOES-16 platform, and required this be done at a time scale that was not prohibitive to rapid product development. The sun angle correction algorithm was applied because it was necessary to correlate similar surface features throughout the significant sun angle changes within a single day.

The classification algorithm was developed to be robust in its ability to accommodate the significant differences anticipated between SBIRS payload data and GOES-16 SWIR data. This thinking led to the use of data cubes built on a fixed array with z values representing the underlying data, and the depth of the cube representing the temporal aspect of the data. By reducing data to four characteristics (X, Y, Z, & time) following the preprocessing steps, the data was made to be more flexible to different user interface applications, and available for manipulation and feasibility testing. Building algorithms that assume this data structure makes them more adaptable to different data sources and data formats for initial input data.

Since this research determined SWIR does possess the sensitivity to discriminate between cloud, ice, and water, the next steps for the ICARTA project are to test it in the lab environment on a dataset that likely has different spatial, spectral, temporal, and radiometric resolutions. Additionally, the classification algorithm will likely need to be improved in order to produce more consistent results through a time series

without requiring the same post-processing as described in the methods. There will need to be significant modifications to the algorithm, but the structure and underlying processes will remain in an effort to generate products as both a test, and eventually as an operational product to support emergency preparedness and civil, commercial, and military operations in the Arctic.

Conclusions:

This research has many implications for follow-on work as well as having significant merit of its own. The purpose of this research was to answer the following questions:

a. Is there enough sensitivity within the SWIR bands of the EM spectrum to develop an accurate sea ice product from a given data set?

b. Can a temporal based approach overcome the data limited nature of a single-channel algorithm, as well as a poor spectral resolution for sea ice studies?

While those questions are answered within this paper, there are significant implications for further research and potential capabilities.

The preprocessing procedures, as well as data enhancement techniques, demonstrated that short wave infrared bands do have enough sensitivity in reflected radiance to develop an accurate sea ice product. The quality of these products is dependent upon the effectiveness of preprocessing steps, as well as the length of time between the development of the classification algorithm and the application of this algorithm. The work demonstrated that as the time between algorithm development and subsequent images increases, the accuracy with which the classification performs significantly degrades. In order to be effective, the data for classification likely needs to be within three hours of the development of the classification model. This ensures that the sun angle corrections as well as atmospheric correction techniques are still relevant and effective. Even within these constraints, the shorter the time between classification algorithm development and application the better. In order to ensure applicability and consistency, a single classification scheme (for GOES-16) should be applied for at least one hour, or four

subsequent images in the time series. Production of classification schemas on a shorter timeline will increase the amount of post-processing time required to ensure consistency with regard to surface type classification between subsequent algorithms.

The second research question is more complicated in its answer. While using a time-series based approach does indeed increase the number of data points available for the development of a classification algorithm, the product of such an algorithm performs similarly to a single-image algorithm with few exceptions. Increasing the training data through a time-series makes an algorithm more robust in its approach to classification of cloud covered pixels. Because this approach looks at a pixel changing in reflected radiance over a period of 45 minutes, it is able to minimize the cloud coverage of atmospheric features moving through the scene during the time period. This is more effective in that it often allows the algorithm to classify more pixels as either water or ice, but it might also create classes that represent reflected radiance values that are too broad to accurately classify the surface medium effectively. Meaning that if a cloud moves through a pixel during the 45 minute time series, the classification will be made based on the three values recorded (in this case two cloud free and one clouded). This classification determination will then be based upon three values, one of which may be a 50% or more increase in reflected radiance than the other two. This adds complexity to the decision tree as well as possibly blurring the edges of each class boundary. In the case of clouds this results in a minimized impact, but at the water/ice interface, this could result in a much more disputable boundary. To minimize this impact, a single image classification should likely be applied simultaneously to identify any significant discrepancy with boundaries between classes.

This research yielded many additional observations besides answering the above questions. While the project confirmed SWIRs utility in sea ice remote sensing, it demonstrated the difficulty in undertaking SWIR sea ice characterization on such a coarse spatial scale. A scale finer than 2km is ideal for such studies if the work is to be truly applicable for the purposes of emergency response and Arctic transportation. This

resolution is required at a minimum in order to convey current ice conditions throughout the Arctic. A scale greater than 2km lacks the ability to chart features that occur at a smaller scale, but are significant factors for navigation – principally leads and thin ice.

While there is clearly an emergency preparedness and transportation application to this research given the time scale available, the scientific implications of similar datasets are noteworthy. Datasets occurring at a fifteen minute (or finer) time scale can assist significantly in our understanding of surface feature timelines. This avenue of research could capture the timescale on which leads can form and refreeze or could be applied over ice sheets to identify the time scale at which melt ponds grow and drain under specific conditions. While neither of these undertakings is likely appropriate for a single-channel approach, the SWIR dataset could be invaluable in filling-in timeline gaps between polar orbiting satellite overpasses. While other satellites likely have much finer spatial resolution and the ability to image in multiple channels across the EM spectrum, this SWIR dataset can provide continuity of surface conditions between satellite overflights. This technique could be used to complete the record in a time series study on any number of surface phenomena on the earth, whether in the cryosphere or elsewhere.

Lastly, this project demonstrated the amount of information that is present in even a single-channel of remotely sensed data. Unlike other ice detecting algorithms which use between two and six channels to identify and characterize ice, this research accomplished similar results using only a single channel with relatively poor spectral resolution. This indication of the inherent value of small datasets should encourage approaching remote sensing problem sets with the intention of minimizing the complexity of the algorithms as well as limiting the data requirements to achieve a purpose. By keeping data sets limited and focusing more on each individual data source, results of remote sensing applications are more likely to resemble the underlying dataset. This effort preserves confidence in the results and likely creates algorithms that are less complicated; more easily comprehended, and therefore have a more defensible epistemology.

Bibliography

Bommarito, J. J. (1993). DMSP special sensor microwave imager sounder (SSMIS). In J. C. Shiue (Ed.) (pp. 230–238). https://doi.org/10.1117/12.152601

Brucker, L., Cavalieri, D. J., Markus, T., & Ivanoff, A. (2014). NASA Team 2 Sea Ice Concentration Algorithm Retrieval Uncertainty. *IEEE Transactions on Geoscience and Remote Sensing*, *52*(11), 7336–7352. https://doi.org/10.1109/TGRS.2014.2311376

Bush, G. W. (2009, January 9). National Security Presidential Directive-66 and Homeland Security Presidential Directive-25: Arctic Region Policy. The White House. Retrieved from https://georgewbush-whitehouse.archives.gov/news/releases/2009/01/20090112-3.html

Cavalieri, D. J., Markus, T., & Comiso, J. C. (2014). AMSR-E/Aqua Daily L3 25 km Brightness Temperature & Sea Ice Concentration Polar Grids. Version 3. 4 August 2007. NASA National Snow and Ice Data Center Distributed Active Archive Center. Retrieved from doi:10.5067/AMSR-E/AE_SI25.003

Comiso, J. C., & Parkinson, C. L. (2008). Arctic sea ice parameters from AMSR-E data using two techniques and comparisons with sea ice from SSM/I. *Journal of Geophysical Research*, *113*(C2). https://doi.org/10.1029/2007JC004255

Dorofy, P., Nazari, R., and, P., & Key, J. (2016). Development of a Mid-Infrared Sea and Lake Ice Index (MISI) Using the GOES Imager. *Remote Sensing*, *8*(12), 1015. https://doi.org/10.3390/rs8121015

Dozier, J. (1989). Spectral signature of alpine snow cover from the Landsat Thematic Mapper. *Remote Sensing of Environment*, *28*, 9–22.

F. Fetterer, J. S. Stewart, & W. N. Meier. (2015). MASAM2: Daily 4-Km Arctic Sea Ice Concentration. Retrieved September 25, 2017, from https://nsidc.org/data/docs/noaa/g10005-masam2/

Frei, A., Tedesco, M., Lee, S., Foster, J., Hall, D. K., Kelly, R., & Robinson, D. A. (2012). A review of global satellite-derived snow products. *Advances in Space Research*, *50*(8), 1007–1029. https://doi.org/10.1016/j.asr.2011.12.021

Gallet, J.-C., Merkouriadi, I., Liston, G. E., Polashenski, C., Hudson, S., Rösel, A., & Gerland, S. (2017). Spring snow conditions on Arctic sea ice north of Svalbard, during the Norwegian Young Sea ICE (N-ICE2015) expedition: Spring Snow Conditions on Arctic Sea Ice. *Journal of Geophysical Research: Atmospheres*, *122*(20), 10,820-10,836. https://doi.org/10.1002/2016JD026035

Hall, D. K., Riggs, G. A., & Salomonson, V. V. (1995). Development of methods for mapping global snow cover using moderate resolution imaging spectroradiometer data. *Remote Sensing of Environment*, *54*(2), 127–140.

Harris Corporation. (2017a). GOES-R ABI Instrument Page. Retrieved September 5, 2017, from http://www.goes-r.gov/spacesegment/abi.html

Harris Corporation. (2017b). GOES-R Advanced Baseline Imager | Harris. Retrieved September 5, 2017, from https://www.harris.com/content/goes-r-advanced-baseline-imager

Harris Corporation, Department of Commerce, National Oceanic and Atmospheric Administration, NOAA Satellite And Information Service (NESDIS), & National Aeronautics and Space Administration. (2016, June 15). Geostationary Operational Environmental Satellite-R Series Product Definition and User's Guide (PUG). Harris Corporation.

Hook, S. (2017). ASTER Spectral Library. Retrieved October 2, 2017, from https://speclib.jpl.nasa.gov/search-1/water

Jacoby, Jr., H. (2014, February 26). *Statement of General Charles H. Jacoby, Jr., United States Army, Commander, United States Northern Command, and North American Aerospace Defense Command, Before the House Armed Services Committee*. Washington, D.C. Retrieved from http://www.northcom.mil/Portals/28/Documents/2014%20NC%20Posture%20Statement_Final_HASC.pdf

Jensen, J. R. (2015). *Introductory Digital Image Processing: A Remote Sensing Perspective* (4th ed.). Pearson.

Leslie, J. (2016). GOES-16 Mission | NOAA NESDIS. Retrieved from https://www.nesdis.noaa.gov/GOES-R-Mission

Kwok, R. (2010). Satellite remote sensing of sea-ice thickness and kinematics: a review. *Journal of Glaciology*, *56*(200), 1129–1140.

Markus, T., & Cavalieri, D. J. (2008). AMSR-E algorithm theoretical basis document: Sea ice products. *NASA: Greenbelt, MD, USA*, *3*. Retrieved from http://citeseerx.ist.psu.edu/viewdoc/download?doi=10.1.1.550.6152&rep=rep1&type=pdf

Markus, T., Cavalieri, D. J., & Comiso, J. C. (2008). AMSR-E algorithm theoretical basis document: Sea ice products. *NASA: Greenbelt, MD, USA*, *3*. Retrieved from http://citeseerx.ist.psu.edu/viewdoc/download?doi=10.1.1.550.6152&rep=rep1&type=pdf

Massom, R., Eicken, H., Haas, C., Jeffries, M., Drinkwater, M. R., Sturm, M., et al. (2001). Snow on Antarctic Sea Ice. *Reviews of Geophysics*, *39*(3), 413–445.

Meier, W., Duerr, R., Fetterer, F., & Stroeve, J. C. (2016, November). NOAA/NSIDC Climate Data Record of Passive Microwave Sea Ice Concentration. Retrieved November 30, 2016, from https://nsidc.org/data/docs/noaa/g02202_ice_conc_cdr/

Melia, N., Haines, K., & Hawkins, E. (2016). Sea ice decline and 21st century trans-Arctic shipping routes: Trans-Arctic shipping in the 21st Century. *Geophysical Research Letters*, *43*(18), 9720–9728. https://doi.org/10.1002/2016GL069315

NASA Worldview. (2018). NASA.

National Ice Center. (2017). National Ice Center Interactive Multisensor Snow and Ice Mapping System. Retrieved September 25, 2017, from http://www.natice.noaa.gov/ims/ims_1.html

National Ice Center and NSIDC. (2010). Multisensor Analyzed Sea Ice Extent - Northern Hemisphere (MASIE-NH). NSIDC. https://doi.org/10.7265/N5GT5K3K

NOAA - NESDIS. (2015a, May). GOES-R Band 5 “Snow/Ice” Fact Sheet. Retrieved from http://www.goes-r.gov/education/ABI-bands-quick-info.html

NOAA - NESDIS. (2015b, June). GOES-R Band 6 “Cloud Particle Size” Fact Sheet. Retrieved from http://www.goes-r.gov/education/ABI-bands-quick-info.html

NOAA - NESDIS. (n.d.). GOES-R Band7 “Shortwave Window” Fact Sheet. Retrieved from http://www.goes-r.gov/education/ABI-bands-quick-info.html

NSIDC Curators. (2010, April). Special Sensor Microwave Imager (SSM/I) Instrument Document. Retrieved November 25, 2016, from https://nsidc.org/data/docs/daac/ssmi_instrument.gd.html

NSIDC Writers. (2009, February). Defense Meteorological Satellite Program (DMSP) Satellite F17. Retrieved November 25, 2016, from https://nsidc.org/data/docs/daac/f17_platform.gd.html

Obama, B. (2013). *National Strategy for the Arctic Region*. The White House. Retrieved from https://www.whitehouse.gov/sites/default/files/docs/nat_arctic_strategy.pdf

Perovich, D. K. (2002a). Seasonal evolution of the albedo of multiyear Arctic sea ice. *Journal of Geophysical Research*, *107*(C10). https://doi.org/10.1029/2000JC000438

Perovich, D. K. (2002b). Seasonal evolution of the albedo of multiyear Arctic sea ice. *Journal of Geophysical Research*, *107*(C10). https://doi.org/10.1029/2000JC000438

Perovich, Donald K. (1996). *The optical properties of sea ice.* COLD REGIONS RESEARCH AND ENGINEERING LAB HANOVER NH. Retrieved from http://www.dtic.mil/docs/citations/ADA310586

Posey, P. G., Metzger, E. J., Wallcraft, A. J., Hebert, D. A., Allard, R. A., Smedstad, O. M., et al. (2015). Improving Arctic sea ice edge forecasts by assimilating high horizontal resolution sea ice concentration data into the US Navy’s ice forecast systems. *The Cryosphere*, *9*(4), 1735–1745. https://doi.org/10.5194/tc-9-1735-2015

Serreze, M. C., & Barry, R. G. (2011). Processes and impacts of Arctic amplification: A research synthesis. *Global and Planetary Change*, *77*(1–2), 85–96. https://doi.org/10.1016/j.gloplacha.2011.03.004

Serreze, M. C., & Barry, R. G. (2014). *The Arctic climate system* (Second edition). New York, NY, USA: Cambridge University Press.

Serreze, M. C., Holland, M. M., & Stroeve, J. (2007). Perspectives on the Arctic’s shrinking sea-ice cover. *Science*, *315*(5818), 1533–1536.

Shokr, M., & Sinha, N. K. (2015). *Sea Ice: Physics and Remote Sensing*. Hoboken, NJ: American Geophysical Union and John Wiley & Sons.

Siljamo, N., & Hyvärinen, O. (2011). New Geostationary Satellite–Based Snow-Cover Algorithm. *Journal of Applied Meteorology and Climatology*, *50*(6), 1275–1290. https://doi.org/10.1175/2010JAMC2568.1

Singh, P. (2011). Network of Stakes. In *Encyclopedia of Snow, Ice and Glaciers* (pp. 775–775). Springer. Retrieved from http://link.springer.com/10.1007%2F978-90-481-2642-2_371

Sturm, M. (2002). Thermal conductivity and heat transfer through the snow on the ice of the Beaufort Sea. *Journal of Geophysical Research*, *107*(C10). https://doi.org/10.1029/2000JC000409

Temimi, M., Romanov, P., Ghedira, H., Khanbilvardi, R., & Smith, K. (2011). Sea-ice monitoring over the Caspian Sea using geostationary satellite data. *International Journal of Remote Sensing*, *32*(6), 1575–1593. https://doi.org/10.1080/01431160903578820

Warren, S. G. (1982). Optical Properties of Snow. *Reviews of Geophysics and Space Physics*, *20*(1), 67–89.

Appendix A

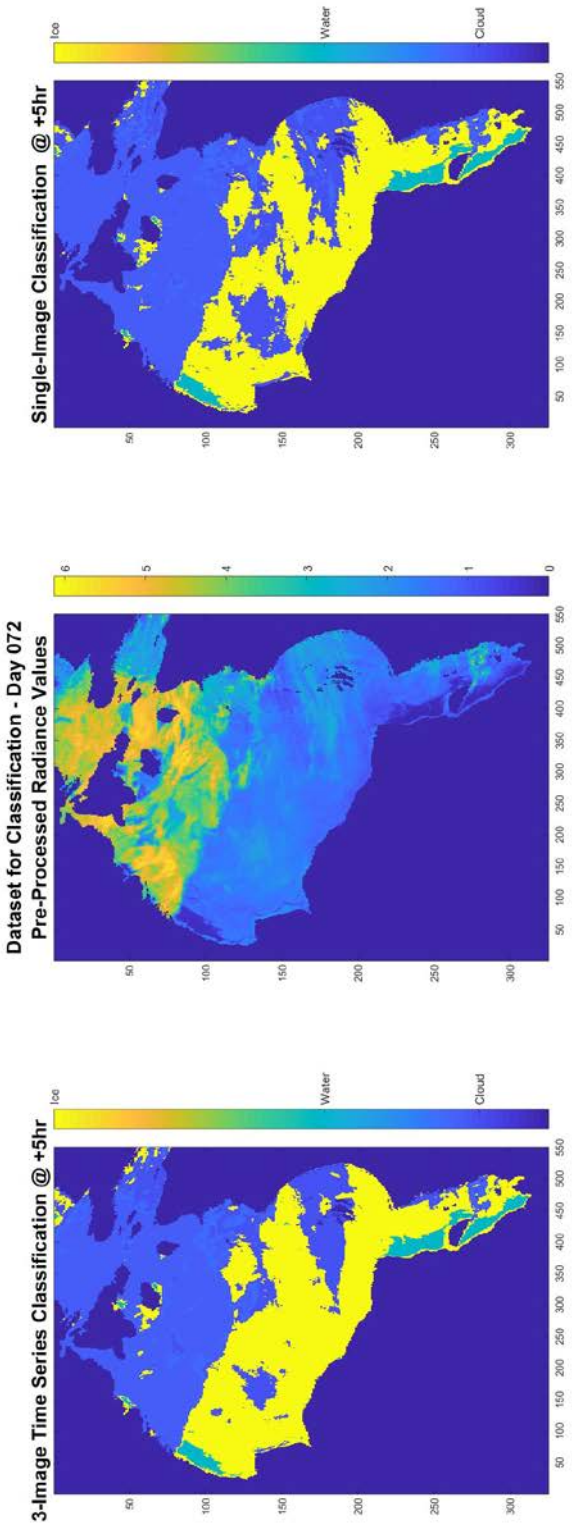

Figure 41: Day 072 classification examples at +5hrs from classification schema development.

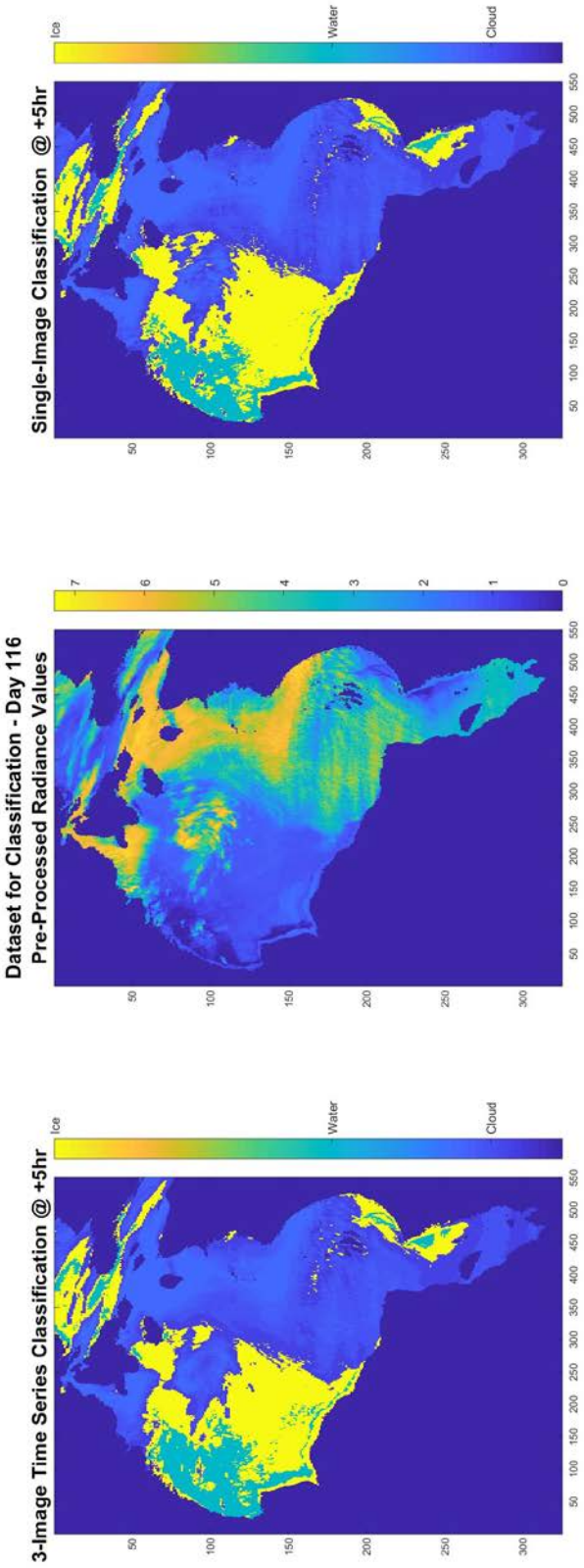

Figure 42: Day 116 classification examples at +5hrs from classification schema development.

Appendix B

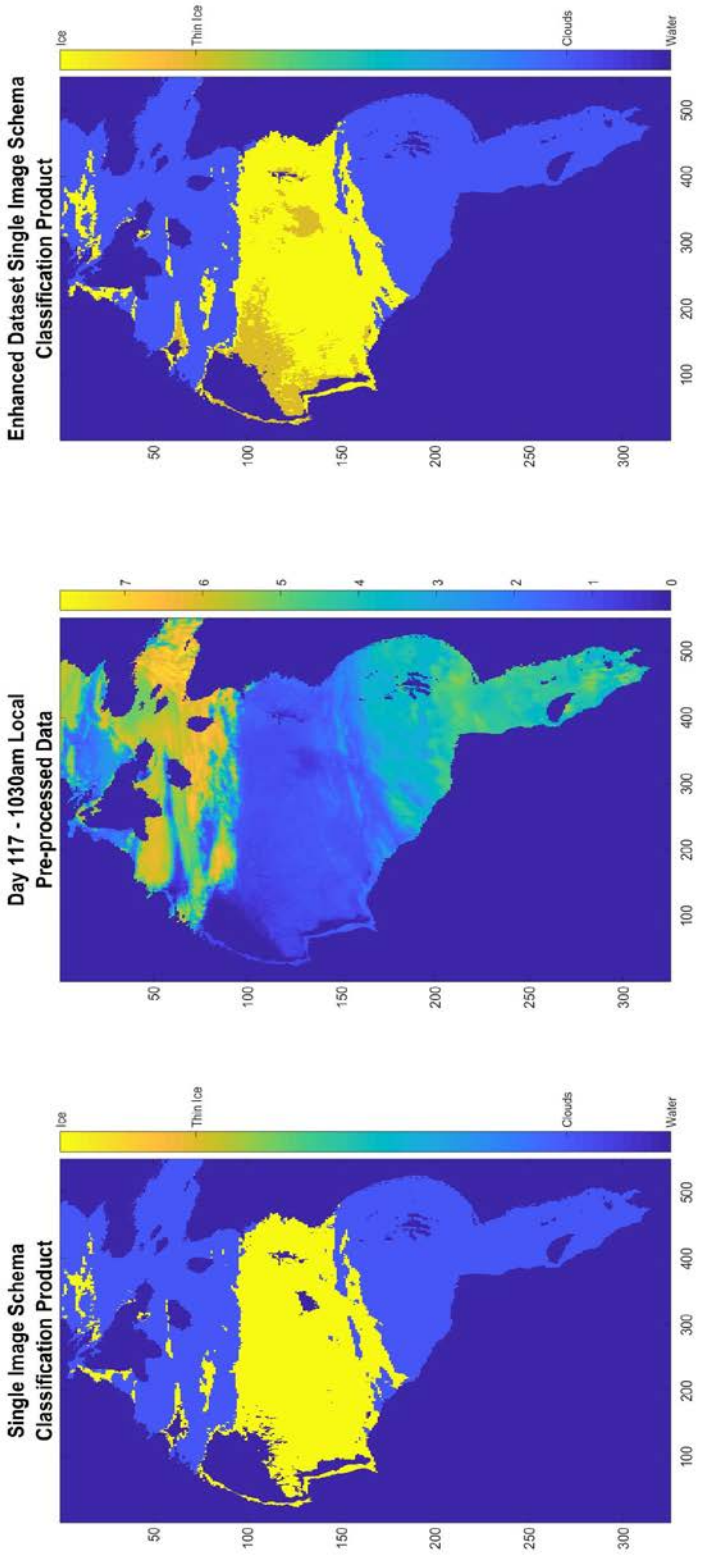

Figure 43: Comparison of the enhanced dataset when classified and the preprocessed dataset when classified. Center shows preprocessed data for comparison.

Appendix C

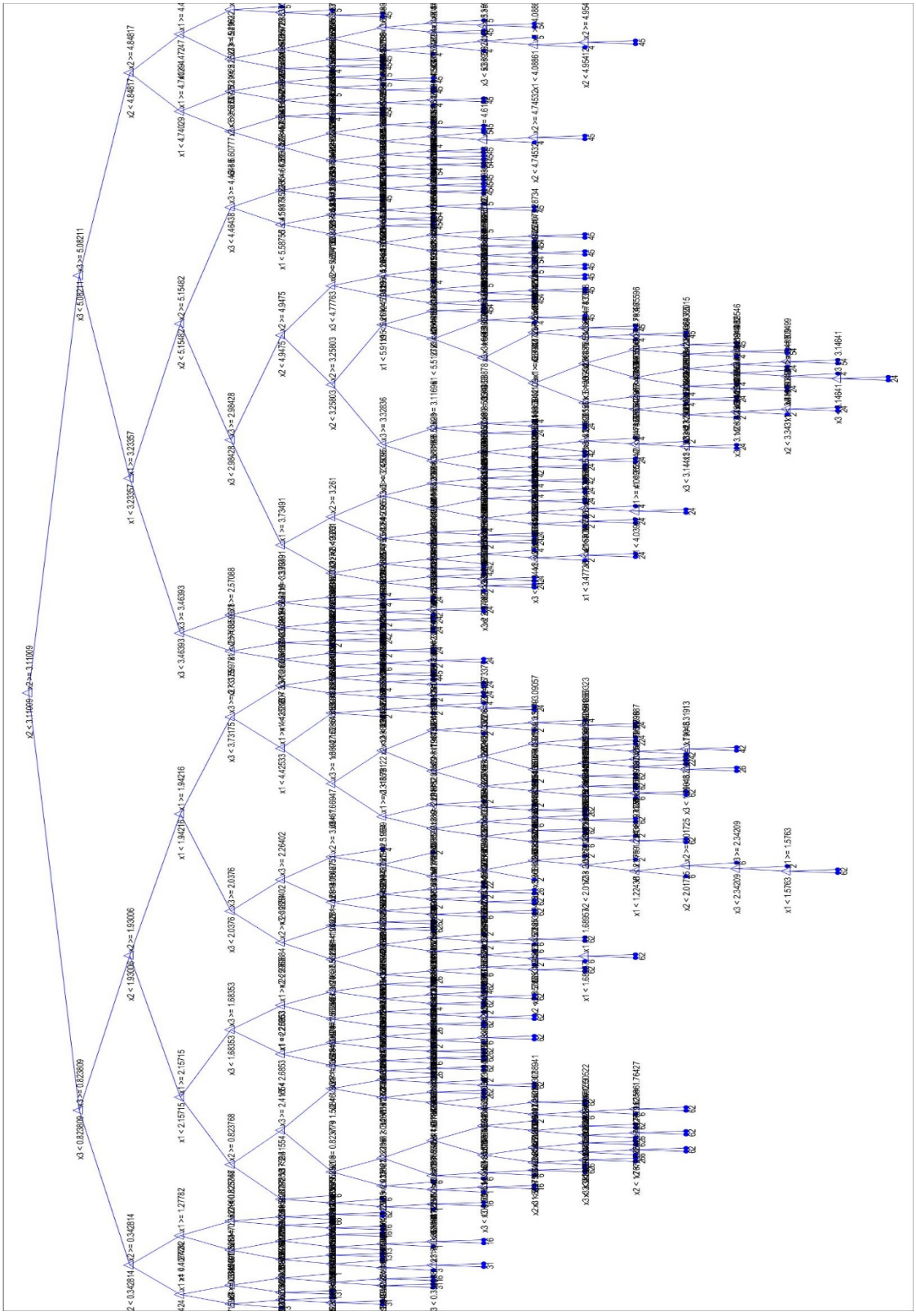

Figure 44: Decision tree for 3-image time series. This example has 74 decision points for classification.

Appendix D – Publication Authorization

DEPARTMENT OF THE AIR FORCE
HEADQUARTERS SPACE AND MISSILE SYSTEMS CENTER (AFSPC)
LOS ANGELES AIR FORCE BASE, CALIFORNIA

FROM: SMC/PA
TO: Nicholas Lewis
SUBJ: Security and Policy Review

29 March 2018

The document titled **"Emerging use of single-channel short wave infrared imaging for sea ice detection"**, our S&PR ID # 18-107, has been reviewed and is determined to be unclassified, technically accurate, non-propriety and suitable for public release.

If you have any questions, please call me at 310-653-2478.

Sincerely,

//s//
Tamry L.McCauely
Security and Policy Review
Space and Missile Systems Center

SMC Case No. 18-107